PROJECT NO. 16-10457

EXPERIMENTALLY VALIDATED COMPUTATIONAL MODELING OF CREEP AND CREEP-CRACKING FOR NUCLEAR CONCRETE STRUCTURES

PROJECT PERIOD: OCTOBER 1, 2016 THROUGH SEPTEMBER 30, 2020

REPORT DATE: OCTOBER 10, 2020

FEDERAL GRANT/ COOPERATIVE AGREEMENT NUMBER (CID): DE-NE0008551

RECIPIENT: TEXAS ENGINEERING EXPERIMENT STATION

PI: ZACHARY GRASLEY, (979) 845-9965, ZGRASLEY@TAMU.EDU

TABLE OF CONTENTS

EXECUTIVE SUMMARY

In a Nuclear Power Plant, one of the most important components is the concrete nuclear reactor cavity, which serves both a structural and protective function as the biological radiation shield. Given that creep has been identified as a major knowledge gap in the assessment of nuclear structures (NUREG/CR-7153), this work helps to further the understanding of creep behavior of massive concrete containment structures for decades to enable safe and long-term operation of these facilities. This project has developed a robust, experimentally validated model to predict creep in nuclear concrete structures for up 60 years using short-term creep data thereby enabling a longer service life of critical facilities and early detection of structural failure.

The work presented in this report is a pairing of computational and experimental methods. For the first time, the time temperature superposition (TTS) principle was successfully used to generate a uniaxial creep compliance master curve to predict mortar creep response for up to 22,500 days (nearly 60 years) at a reference temperature of 20°C. These data were used as input into finite element analysis (FEA) codes that use highly realistic random, 3D concrete microstructures from reconstructed coarse limestone aggregates. Finite element analysis performed provides the ability to quickly upscale mortar viscoelastic behavior to long-term concrete creep/relaxation data. A master creep compliance curve, constructed from the TTS principle, spanning 27 years, was used to validate two and a half decades of simulated concrete creep.

Concurrently, three different simulated wall specimens were designed to mimic the behavior of post-tensioned concrete nuclear containment facility vessel walls over time as a result of concrete creep. The specimens were designed with different thicknesses, transverse and longitudinal reinforcement ratios, and level of post-tensioning stress. Each specimen contained various instrumentation to measure internal concrete temperature, concrete strain, and post-tensioning strain hourly for over 3 years.

The concrete creep model developed in this project, based on the FEA concrete simulations, was applied to simulate the structural-scale experiments of prestressed concrete walls conducted in this project using the Grizzly code. These models can represent the effects of reinforcing and prestressing. Although there are some discrepancies with the experimental data, the model can predict the overall trends of the creep response in these experiments. One of these experimental models was also applied to an extended time to demonstrate how the findings from this study can be used to predict the behavior of actual structures of interest that have been in service for extended periods of time.

1 INTRODUCTION

1.1 Problem Statement

In a Nuclear Power Plant (NPP), one of the most important components is the concrete nuclear reactor cavity, which serves both a structural and protective function as the biological radiation shield. Additionally, radioactive waste and disposal facilities are also commonly made of concrete. As NPPs across the United States continue to operate past their initial design lifetimes of 40 years, some plants even approaching a second license renewal, it is important to understand the long-term durability of the concrete components in NPPs (Graves, Le Pape et al. 2014). In recent years, the US Nuclear Regulatory Commission (NRC) evaluated the aging-related degradation mechanisms of core components and materials present in NPPs and identified concrete creep in NUREG/CR-7153 as one of the primary safety-related areas where further study is necessary (Graves, Le Pape et al. 2014). In February 2013, Duke Energy decided to decommission the Crystal River 3 nuclear power plant in Florida due to cracks formed in the containment structure during a maintenance operation where concrete creep was speculated to be one of the contributing causes for the failure (Georgia Institute of Technology, 2015). Creep is a viscoelastic phenomenon that causes concrete to deform for decades under a constant stress. Since the nuclear plants are post-tensioned containment facilities, creep causes post-tensioning losses, which reduces the tensile force in the tendons to fall below the original design. Understanding the changes to the loss of prestress and post-tensioning is crucial to assess the concrete structure's ongoing viability and service life.

Modeling of concrete creep has been researched for decades, both analytically (Tulin 1965, Jordaan 1974, Bazant and Panula 1978, Scheiner, Hellmich et al. 2009) and through numerical simulations (Huang, Yan et al. 2016, Bernachy-Barbe and Bary 2019). In this study, concrete creep was evaluated in four tasks: a) Material level creep and strength experiments; b) Cement mortar to concrete creep upscaling using a computational approach; c) Large-scale structural concrete creep experiments; and d) Updating Grizzly with new material models.

1.2 Project Objectives

The main goal of this research is to understand the decades-long creep behavior of massive containment structures to enable safe and long-term operation of these facilities. Due to the complexity of concrete creep, important challenges are presented, and the scope of the research is focused on several key factors.

Primary Challenges and planned mitigations

Some of the challenges associated with the creep study are:

1. Creep is temperature dependent and proceeds for decades

Concrete creep is known to continue for decades and is speculated to continue indefinitely (Brooks, 2005). A direct, long-term measurement of creep is unattainable given the short time period for the project. Furthermore, concrete creep is temperature dependent. Nuclear concrete undergoes harsh service conditions involving steep temperature and pressure gradients during their lifetime. Hence, determining the dependence of creep on temperature is important for accurately predicting nuclear concrete creep. To address these two challenges, a novel step was taken in the study. Firstly, experiments on concrete creep was substituted by cement mortar creep. It is believed that – since concrete creep occurs almost entirely within the cement paste phase due to the typically linearly elastic behavior of aggregates – the concrete creep behavior can be captured from cement mortar specimens. The focus on cement mortar rather than concrete allows the use of smaller sized test samples compared to traditional concrete creep tests and enables more tests to be run simultaneously with enhanced resolution while minimizing experimental error. Secondly, unique miniature versions of conventional creep frames were built that were much more amenable to placing in climate chambers than larger concrete creep frames. To measure the effect of high temperatures on mortar creep, tests were performed at elevated temperatures (up to 80°C). It is known that concrete creep increases as a function of temperature (Nasser and Neville 1965; McDonald 1975; Ladaoui et al. 2011; Vidal et al. 2015). This introduces the possibility of predicting long-term creep at room temperature by measuring short-term creep at high temperatures using the Time-Temperature Superposition (TTS) principle. The TTS principle was first noted by Schwarzl (Schwarzl et al. 1952), who recognized that an increase in temperature generally increases the kinetics of most deformation processes in viscoelastic materials. In thermo-rheologically simple materials, this implies that during similar deformation processes at different temperatures, the same sequence of molecular events occurs with different speed and can be correlated using temperature dependent shift factors. The results from the creep tests at different temperatures were shifted to fit along the axis of logarithmic time scale to obtain a creep master curve.

2. Creep is age and moisture dependent

Concrete ages with time and creep is moisture dependent. As concrete ages with time, the properties of the material changes, thereby affecting the creep rate. Creep reduces when stress is applied on aged concrete. However, aging is most critical in the first 28 days after mixing and since post-tensioning for containment walls are not applied at early ages, these effects can be approximated as second order and can be ignored. Most U.S. nuclear plants have a liner on the interior of their containment facility which minimizes the effect of drying. Experimental measurements of a 30-year-old nuclear wall with liner suggested the internal Relative Humidity (RH) never drops below 80% (Åhs and Poyet, 2015; Oxfall et al., 2013). Throughout the study, creep experiments were carried out on cement mortar/concrete samples that were sealed to prevent drying. Bazant's B3 model and B4 model were also used to assess if significant drying creep occurred in the samples based on the measured free shrinkage strain.

3. Concrete is a nonlinear and creep is a 3D problem

Concrete behaves nonlinearly at higher stress levels. But, according to Neville and Dilger non-linearity of cement mortar arises only after the stress/strength is greater than 0.80 (Neville and Dilger, 1970). According to Mindess et al., concrete creep is linearly proportional to stresses up to 50% of its ultimate strength (Mindess et al., 2003). In this study, stress levels were maintained below the nonlinearity region. Concrete creep is generally modelled in terms of uniaxial creep compliance. However, nuclear structures are subjected to a 3D state of stress. Significant creep strains may be induced in directions transverse to each principle stress due to Poisson's effect. To address this issue, 3D creep response of cement mortar was evaluated using a novel, confined compression experiment that allows direct determination of the full stress and infinitesimal strain tensors in a single test.

In response to the problems identified above, a multi-faceted research program was conducted at Texas A&M University to understand the material and structural implications of concrete creep and creep-cracking in nuclear structures. The specific research objectives covered are:

1. Devise a new, 3D concrete material constitutive model based on 3D creep and cracking experiments ready for implementation in Grizzly[1].
    a. Use the Time-Temperature Superposition (TTS) principle to extend experimental mortar creep data to a longer time frame
    b. Use Finite Element Analysis (FEA) of virtual concrete microstructures to model creep of concrete to upscale the mortar experimental data
2. Establish an improved large-scale structural modeling approach that considers full 3D stress fields rather than plane stress that has been conventional in past analyses of nuclear concrete structures.
    a. Utilize results from Objective 1b to describe the behavior of concrete in a large-scale structure simulation in Grizzly
    b. Validate Grizzly results with data from large-scale wall section data

1.3 Logical path to accomplish goal

The project objectives were accomplished following a sequential path of tasks:

1. Literature review

    A thorough review of published literature was conducted to determine the appropriate mixture design for the experimental samples and wall sections, as well as the optimal computational methods and approaches

[1] Grizzly is a multi-physics object oriented simulation environment for simulating component aging and damage evolution for LWRS specific applications.

2. Creep experiments

   Creep compliance master curve of cement mortar was estimated for decades long using time-temperature superposition principle.

3. Computational upscaling

   Virtual concrete was generated and simulated under FEA to predict concrete creep behavior, using experimental mortar data as input to describe the viscoelastic properties of the mortar phase in the model.

4. Development of 3D concrete constitutive models

   The FEA simulations were used to generate a constitutive, homogenized response to describe the creep compliance behavior of concrete.

5. Large-scale structural concrete validation experiments

   Large-scale wall segments were fabricated early in the project to provide several years of stress and strain data while exposed to the environment.

6. Update Grizzly with concrete creep material model

   The constitutive model from Task #4 was used to describe the viscoelastic behavior of the concrete in simulations of the large-scale wall specimens.

7. Validate models

   The FEA models of concrete and the Grizzly models of the large-scale structures are validated against experimental concrete creep data and the experimental data collected from the large-scale experiments, respectively.

These tasks are inter-dependent, as represented below:

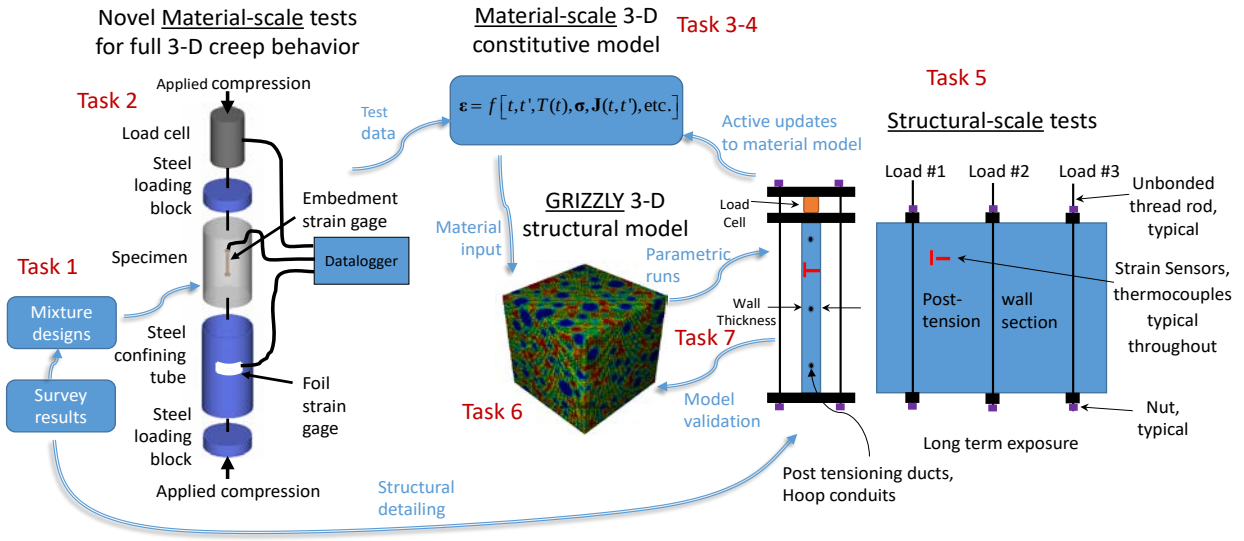

Figure 1. Flowchart of experimental and computational research plan to achieve the proposed objectives

References

1. Åhs, M. and Poyet, S. (2015). The prediction of moisture and temperature distribution in a concrete reactor containment. Tech. report. Lund University.
2. Bazant, Z. P. and L. Panula (1978). Practical prediction of time-dependent deformations of concrete. 12: 169--174.
3. Bernachy-Barbe, F. and B. Bary (2019). Effect of aggregate shapes on local fields in 3D mesoscale simulations of the concrete creep behavior. Finite Elements in Analysis and Design 156 (September 2018): 13--23.
4. Georgia Institute of Technology. (2015). PhD student Bradley Dolphyn studying the concrete cracks that shut down Crystal River nuclear power plant. https://ce.gatech.edu/category/crystal-river-3.
5. Graves, H., Y. Le Pape, D. Naus, J. Rashid, V. Saouma, A. Sheikh and J. Wall (2014). Expanded Materials Degradation Assessment (EMDA): Aging of Concrete and Civil Structures (NUREG/CR-7153), Nuclear Regulatory Commission. 4.
6. Huang, Y., D. Yan, Z. Yang and G. Liu (2016). "2D and 3D homogenization and fracture analysis of concrete based on in-situ X-ray Computed Tomography images and Monte Carlo simulations." Engineering Fracture Mechanics 163: 37--54.
7. Jordaan, I. J. (1974). "A note on concrete creep analysis under static temperature fields." Mat \' e riaux et Constructions 7(5): 329--333.
8. Ladaoui, W., Vidal, T., Sellier, A. and Bourbon, X. (2011). Effect of a temperature change from 20 to 50ºC on the basic creep of HPC and HPFRC. Mater. Struct. 44 (9), 1629-1639.

9. Mc Donald, J. E. (1975). Time dependent deformation of concrete under multiaxial stress conditions. In: Technical Report C-75-4 Concrete Laboratory, US Army Engineering Waterways Experiment Station, Vicksburg, MS.
10. Nasser, K. W. and Neville, A. M. (1965). Creep of Concrete at Elevated Temperature. ACI J. Proc. 62 (12), 1567-1579.
11. Oxfall, M., Johansson, P. and Hassanzadeh, M. (2013). Moisture profiles in concrete walls of a nuclear reactor containment after 30 years of operation. Lund university.
12. Scheiner, S., C. Hellmich and A. M. Asce (2009). "Continuum Microviscoelasticity Model for Aging Basic Creep of Early-Age Concrete." Journal of Engineering Mechanics.
13. Schwarzl, F. and Staverman, A. J. (1952). Time-Temperature Dependence of Linear Viscoelastic Behavior. J. Appl. Phys. 23.
14. Tulin, L. G. (1965). Creep of a Portland cement mortar as a function of stress-level and time. PhD, Iowa State University.
15. Vidal, T., Sellier, A., Ladaoui, W., and Bourbon, X. (2015). Effect of temperature on basic creep of High-Performance Concretes heated between 20ºC and 80ºC. J. Mater. Civil Eng. 27 (7).

2 MATERIAL LEVEL CREEP AND FRACTURE EXPERIMENTS

2.1 Introduction

The main goal of the material level creep experiments is to develop a constitutive model for long-term creep compliance of cement mortar from short-term experiments using the Time-Temperature Superposition (TTS) principle. For this purpose, a unique, miniature version of the standardized concrete creep frame was designed that is amenable to placing in climate chambers and temperature ovens. The 3D creep response of mature cement mortar was examined using the confined compressive creep test in the miniaturized frame that allows direct determination of the full stress and infinitesimal strain tensors in a single test. The constitutive properties of cement mortar were upscaled to predict concrete creep behavior as illustrated in the subsequent task. To validate the concrete creep model upscaled from the mortar, few concrete creep tests were conducted in the laboratory at room temperature and elevated temperatures up to 60 °C. The steps involved to accomplish the current task includes the following:

1. Design of ten miniaturized creep loading frames for cement mortar samples.
2. Instrumentation and data collection of uniaxial creep test on cement mortar.
3. Development of a constitutive model to predict several decades of creep compliance of cement mortar through short term tests using TTS principle.
4. Design of a novel confined creep test to capture the 3D constitutive properties of cement mortar.
5. Development of bulk and shear compliance functions as well as viscoelastic Poisson's ratio of cement mortar from the confined creep test.
6. Conducting creep test on concrete specimens to validate the upscaling scheme of cement mortar to concrete properties using advanced computational models.

These steps can be grouped into three major sub-tasks as shown in the flowchart below:

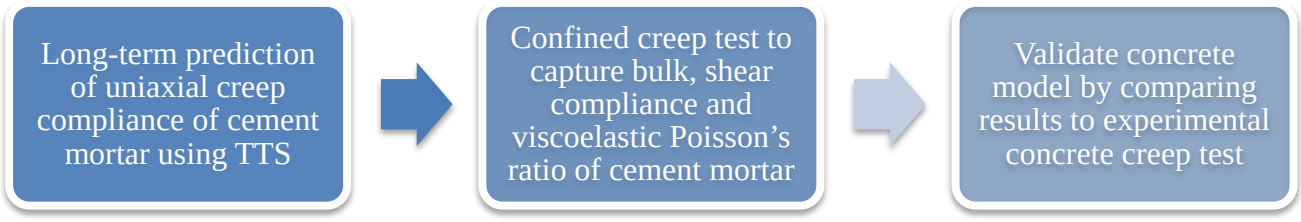

Figure 2. Flowchart showing the sub-tasks involved in the experimental study

2.2 Uniaxial Creep Test

The focus of this sub-task is to utilize the Time Temperature Superposition Principle to predict several decades of creep compliance of cement mortar from short term experiments at elevated temperatures.

2.2.1 Literature review

A viscoelastic material such as concrete has the characteristics of an elastic spring as well as viscous dashpot. When such a material is subjected to constant stress, there is an instantaneous elastic response followed by time-dependent creep strain. When the material is unloaded from stress, there is an instantaneous elastic recovery followed by creep recovery. In most cases, there is a considerable portion of total creep that is irreversible (Figure 3).

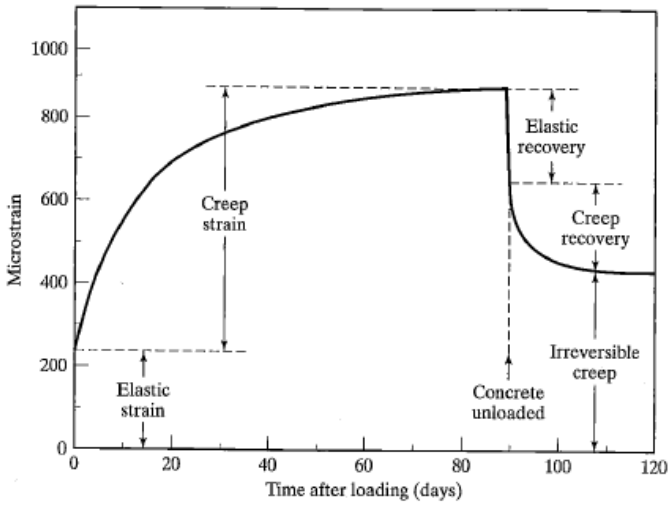

Figure 3. Typical creep behavior of plain concrete (Mindess, Young and Darwin book, 2003).

Different combinations of a spring and dashpot elements may be used to represent stress and corresponding strain component for a viscoelastic material. The two most common mechanical models used to represent the compliance function are the Maxwell model and Kelvin-Voigt model. Kelvin-Voigt (spring and dashpot in parallel) is suitable for predicting creep response of viscoelastic material. But, as concrete creep is known to continue indefinitely (Brooks, 2005) and the compliance function in a Kelvin-Voigt model asymptote at later ages, the creep compliance was represented using the logarithmic function such as:

$$J(t) = \sum_{i=1n}^{n} \frac{1}{E_i} Log\left(1 + \frac{E_i}{\mu_i} t\right) \quad (1)$$

where E_i refers to the spring constant and μ_i refers to the viscosity of the dashpots. The term μ_i / E_i can be denoted as τ_i called the retardation time.

Several studies have been conducted over the past few decades to predict concrete creep (Tulin 1965; Jordaan 1974; Bažant 1988; Brooks, 2005). In post-tensioned structures such as nuclear containment facilities and hydraulic dams, creep can cause redistribution of stresses, large deformations and prestress losses that ultimately compromise the safety of the structure. As creep occurs for decades, laboratory measurements of long-term creep are both challenging and time consuming; this serves as motivation for researchers to develop more effective methods to characterize or predict long-term creep of concrete. There are numerous studies in the literature that discuss the effects of temperature on creep of concrete. Nasser and Neville found that creep of concrete at room temperature (21ºC) can be 3 to 4 times the initial deformation within the first 1 to 2 years and that at elevated temperatures, such as 96ºC, creep effects are further amplified. Nasser and Neville found that for samples with a stress-strength ratio of 35% loaded at 14 days of age and 15 months under load, the creep at 72ºC was 1.75 times greater than that at 21ºC and the creep at 96ºC was 1.95 times higher than that at 21ºC (Nasser and Neville 1965). In comparison, McDonald showed that for samples at a stress-strength ratio of 31% loaded at 90 days of age and 12 months under load, the compressive creep of concrete at 66ºC was 1.79 times that observed at 23ºC (McDonald 1975). Bažant summarized the temperature effect on concrete creep from the literature and used the microprestress-solidification theory to fit the data considering the influence of temperature (Bažant et al. 2004). More recently, researchers (Ladaoui et al. 2011; Vidal et al. 2015) have analyzed the effect of temperature ranging between 20ºC and 80ºC on the basic creep of High-Performance Concrete (HPC). The companion studies concluded that the basic creep of HPC doubled at a stress-strength ratio of 30% and 10 months under load when the temperature was increased from 20ºC to 50ºC.

It is hence well-established that concrete creep increases as a function of temperature. The TTS principle was first noted by Schwarzl (Schwarzl et al. 1952), who recognized that an increase in temperature generally increases the kinetics of most deformation processes in viscoelastic materials. TTS is effectively used to model the temperature-dependent mechanical properties of thermorheologically simple polymers wherein temperature changes significantly impact creep. Thermorheologically simple materials are those materials whose temperature dependence for viscoelastic processes is fully captured by the temperature dependence of relaxation/retardation times (Drozdov 1998; Christensen 2003; Hernández 2017). For such materials, by experimentally measuring creep strain at different temperatures, a creep master curve can be generated by shifting the data along a logarithmic time axis.

2.2.2 Initial Assessment of the TTS Principle to Predict Creep

As an initial step to verify the applicability of developing a creep master curve for cement mortar using TTS, basic creep data obtained from a recent study (Vidal et.al 2015) was fitted using the

TTS principle to predict long-term creep. The basic axial creep data used was obtained on HPC using Type I cement with stress/strength ratio of 35% loaded at 300 days of age and 10 months under load at 20ºC, 50ºC and 80ºC. The creep compliance was computed from the basic creep strain and applied stress. The data obtained for creep compliance at high temperatures was then shifted to a reference room temperature (20ºC) using a temperature shift factor to obtain a creep compliance master curve (Figure 4). The resulting smooth curve with overlapping data from differing temperatures illustrated that TTS was successfully applied to predict creep compliance for nearly 30 years using basic creep data obtained during the initial 300 days.

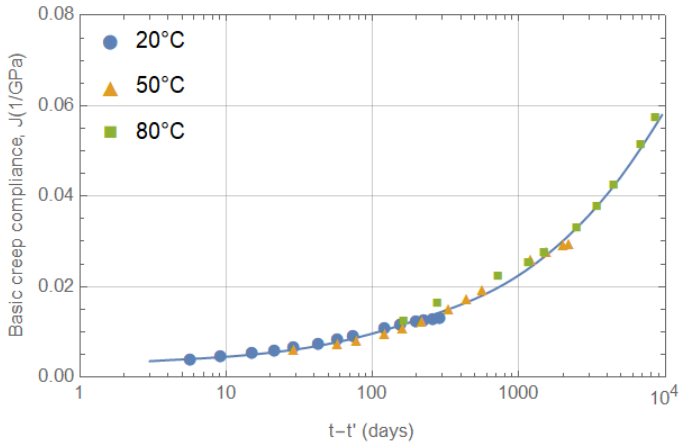

Figure 4. Basic creep compliance, J (t,t') master curve at 20ºC developed using TTS principle applied to data from Vidal et al. 2015

In addition, the B4 model (Bažant et al. 2014) was used to generate basic creep compliance curves for mature concrete (loaded at 56 days of age) at three different temperatures (20ºC, 50ºC and 80ºC); the results are plotted in Figure 5. It is clear from the figures that the B4 model – which is based on fitting a large database of concrete creep test results – predicts a temperature dependence of basic creep that indicates a thermorheologically simple behavior of the mature concrete. This should not be surprising given that the B4 model quantifies the temperature effects on concrete creep as a multiplier (determined by an Arrhenius function of temperature) on creep time (to create a reduced time) – this is essentially equivalent to using a multiplier on relaxation/retardation times.

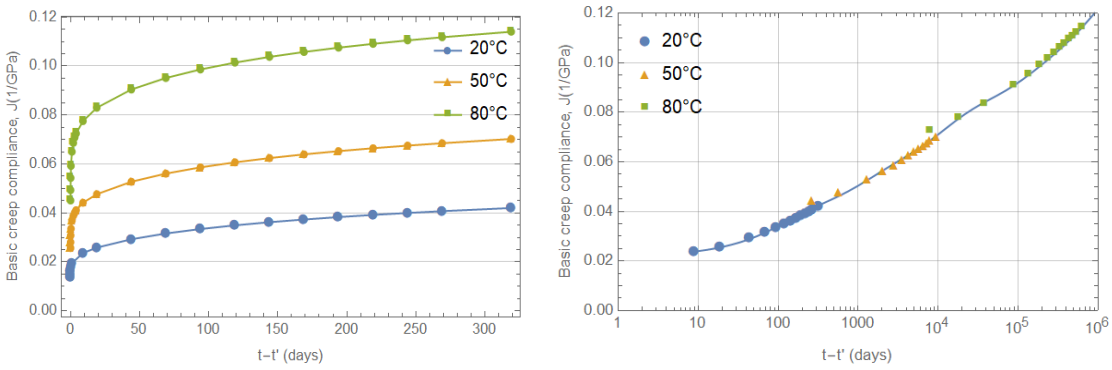

(a) (b)

Figure 5. a) Basic creep compliance of concrete using B4 model at different temperatures. (b) Basic creep compliance master curve at 20°C on log time scale using TTS principle.

These initial analyses of a recent dataset of concrete creep at multiple temperatures and the B4 model of concrete creep both indicate that mature concrete, exhibiting only basic creep, may be well approximated as behaving in a thermorheologically simple fashion. However, it should be noted that at early ages concrete likely does not behave in a thermorheologically simple fashion given the strong influence of hydration and other aging mechanisms (Grasley 2006 and Grasley and Leung 2011). Furthermore, at temperatures below the freezing and above the boiling points of water the TTS principle will not be applicable given that the temperature effects generate phase changes and initiate new mechanisms of time-dependent deformation (Rahman et al. 2016) rather than simply influence the kinetics of mechanisms active in the intermediate temperature range.

2.2.3 Experimental Design

The cement mortar mix design was selected to closely resemble the Vérification Réaliste du Confinement des Réacteurs (VeRCoRs) mortar mix used by Électricité de France (EDF). The mortar samples were prepared using Type I/II cement and river sand. The river sand used was sieved to pass the 2.38 mm sieve and dried for 24 hours before mixing. The water to cement ratio by mass (w/c) for the mix was kept at 0.52 (SSD condition) and the sand to cement ratio by mass was 2.12. About 422.5 mL of water reducing admixture ‘Pozzolith 80’ was added per 100kg of cement. The mixture proportions are shown in Table 1 and referenced in (EDF 2014).

Table 1. **Mixture proportions in SSD condition**

Materials	Unit	Mix Quantity
Cement (Type I/II)	kg/m^3	601
	lb/yd^3	1013
River Sand	kg/m^3	1263
	lb/yd^3	2129
Water	kg/m^3	323
	lb/yd^3	544.4
Pozzolith 80	l/m^3	2.54
	oz/yd^3	66

Sample Preparation

Creep Samples

Cement mortar was mixed in accordance with ASTM C305-99 and immediately cast into 50 mm x 100 mm (2 in. x 4 in.) cylindrical molds with embedded vibrating wire gages (50 mm or 2 in. gage length) from Geokon. Fishing line was used to suspend the gage axially at the center of each mold. The cylinders were filled in three equal increments and tapped after each increment to minimize air voids. Once filled, the cement mortar samples were retained in the mold to prevent moisture loss until just prior to the time of testing after 28 days. The demolded samples were immediately sealed with one layer of adhesive-backed aluminum foil to minimize drying. Sulfur capping compound was used to ensure the ends of the sample were smooth and concrete plugs were attached to both ends of the sample to ensure uniform compressive stress throughout the cross-section per the St. Venant's principle.

Free Strain Samples

In addition to the uniaxial creep test, companion cylindrical specimens having dimensions of 50 mm x 100 mm (2 in. x 4 in.) were fabricated to record the free strain due to shrinkage at each temperature for the entire duration of the creep test. The age and test conditions of these load-free specimens were the same as those used in the creep tests. An embedded vibrating wire gage was used to record the free strain with time.

Fabrication of Creep Frame

A unique, miniature version of the standard ASTM C512 concrete creep frame was designed and fabricated exclusively for the cement mortar samples as shown in Figure 5. The total height of the scaled down frame is 45 cm (18 in.) as supposed to the approximately 180 cm (6 ft.) tall standard concrete creep frame. The diameter of the frame is 10 cm (4 in.). The creep frame has a compression spring at the bottom of the frame which helps to maintain a constant load. Above the spring is a plate with a ball bearing at the center to ensure minimum eccentricity in loading. An inline load cell is placed just below the sample to record the load levels in the frame. Although stress levels are intended to be constant during a creep test, the actual stress level was recorded periodically to account for any load loss. A 5 ton mini hydraulic jack was used to apply the initial axial force. Threaded rods and nuts are provided in the frame to maintain a constant load after removal of the jack. Most importantly, the newly designed creep frame is amenable to placing in climate chambers and temperature ovens required to perform thermally accelerated creep tests. More details of the creep frame is presented in Baranikumar, (2020).

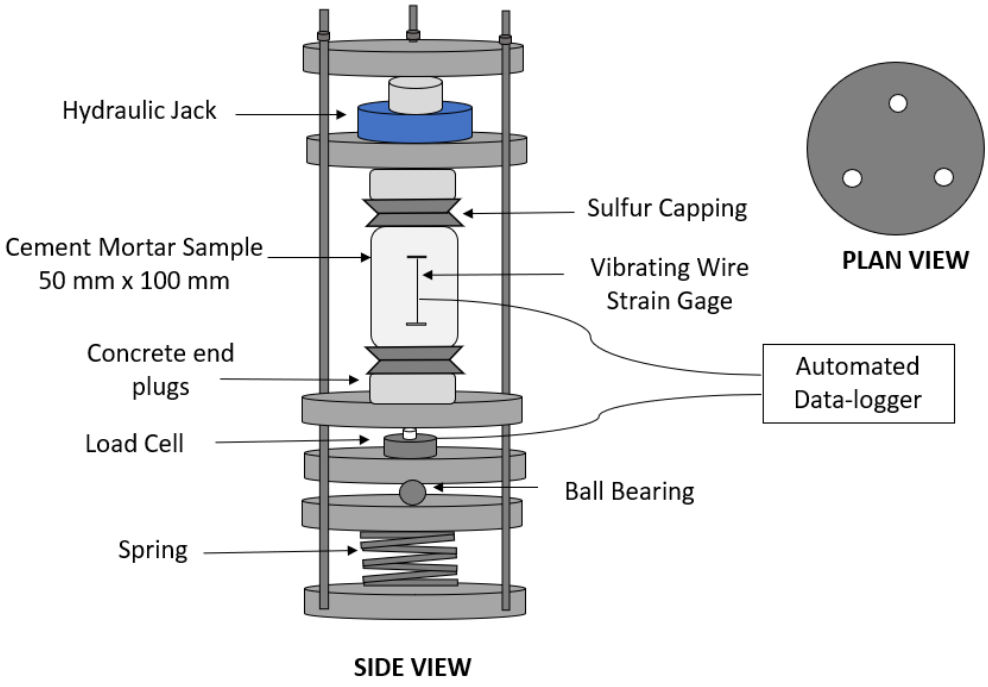

Figure 6. Miniaturized cement mortar creep test frame. This frame is 45 cm (18 in.) in total height and is a scaled down version of ASTM standard concrete creep frame, which is approximately 180 cm (6 ft.) in height.

Uniaxial Creep Test setup

The previously described miniaturized creep frame was used to run the uniaxial creep test. The cement mortar samples were loaded at 28 days of age using a hydraulic jack to a constant load of

775 kg (1700 lbs.) which corresponded to 10% of 28-day compressive strength of the mortar. At this loading age and stress magnitude, the mature cement mortar is approximated as a non-aging, linearly viscoelastic material.

The load was approximated as a stepwise load function given the very short time span of load application relative to the overall duration of the creep test. The axial strain from the vibrating wire gage as well as the load readings from the load cell were recorded every 30 minutes using a CR300 Data logger, AM16/32B Multiplexer and a 2-Channel Vibrating-Wire Analyzer (AVW200) purchased from Campbell Scientific. As alluded to earlier, creep tests were run at three different temperatures: 20°C (reference temperature), 60°C and 80°C. Three replicates of cement mortar samples were used at each temperature and were heated to the respective test temperature before starting the creep test (to avoid the accumulation of thermal strains during creep). The experiments were conducted in environmental chambers maintaining a constant temperature (Figure 5**Error! Reference source not found.**). The relative humidity was consistent at 50% in the 20°C chamber and below 10% in the 60°C and 80°C chambers.

Figure 7. Uniaxial creep test setup using the miniaturized creep frame inside an environmental chamber maintaining constant temperature and humidity.

2.2.4 Results and Discussion

The stress applied was calculated as a function of time using the load recorded from the load cell and the cross-sectional area of the samples. If load loss was observed, it was accounted for while modeling creep compliance, as described later in this section. Significant load loss was observed in the cement mortar samples at the higher temperatures (60°C and 80°C) due to

appreciable creep deformation. The samples at 80°C were reloaded if the load dropped to below 50% of the initial load applied. If a second load application was required, as was the case with few samples at 80°C, sigmoidal function was used to fit the entire stress history and the creep compliance was modelled using the Boltzmann's superposition principle for the two applications of load.

Figure 8 shows the different components of strain in the mortar sample from a creep test. The strain readings represent the average strains recorded for the three replicate specimens. The vibrating wire gage at the center of the sample records the total strain. The free strain reading was constantly monitored in an unloaded specimen at the same age and test conditions. The creep strain in Figure 8, which is the primary point of interest in this study, is the difference between the total strain and free strain.

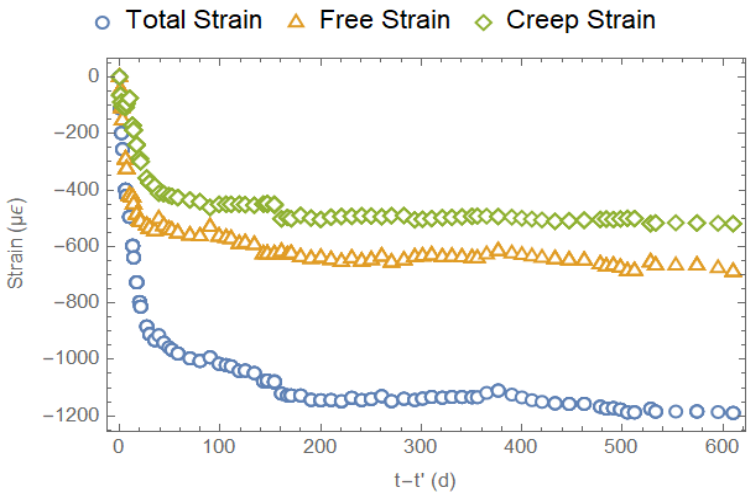

Figure 8. Graph showing total strain, free strain and creep strain for a sample under load as a function of time.

It was observed that after 600 days, the creep strain at 60ºC was 1.51 times higher than that at 20ºC and the creep strain at 80ºC was 2.40 times higher than that at 20ºC. These multipliers are similar to those recorded in existing literature (Nasser and Neville 1965; McDonald 1975). Using the B4 model, creep at 60ºC and 80ºC was 1.32 times and 1.88 times higher respectively than the corresponding value at 20ºC. The average creep strains obtained at the different test temperatures are plotted in Figure 9.

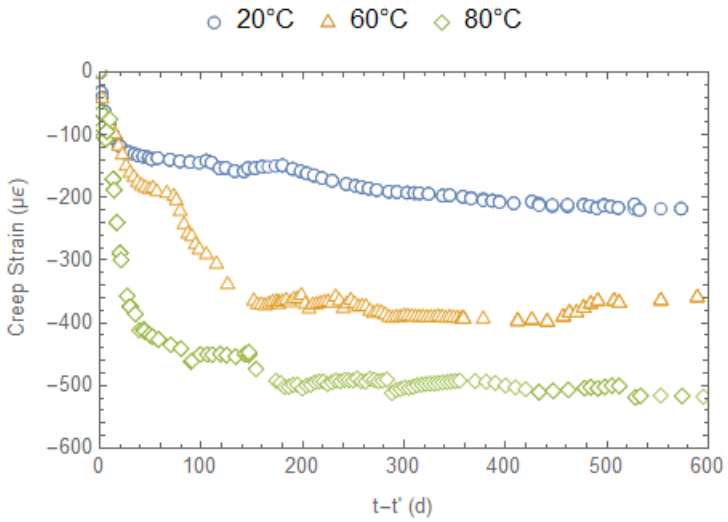

Figure 9. Average creep strain data at different temperatures. The creep strain at 60°C is 1.51 times higher and the creep strain at 80°C is 2.40 times higher than that at 20°C after 600 days of testing.

Since there is significant load loss encountered in creep tests conducted at elevated temperatures, a more informative way to compare the creep test results at varying temperatures (rather than plotting creep strain) is to assess the creep compliance, $J(t)$. The creep compliance at a constant load is given by dividing the measured creep strain by the applied stress, but the stress-strain relationship is of the integral or differential type for a non-constant stress history. For a non-aging, linearly viscoelastic material, the axial strain ($\varepsilon(t)$) is related to the axial stress $\sigma(t)$ according to

$$\varepsilon(t) = \int_0^t J(t-t') \frac{\partial \sigma(t')}{\partial t'} dt' \quad , \tag{2}$$

where t is the present time and t' is the dummy time variable. In order to determine $J(t)$ using the constitutive expression, it is necessary to fit the measured stress history to a time dependent function, take the derivative of that function (in terms of the dummy time variable), multiply the derivative by a presumed function for $J(t)$ - including phenomenological fit coefficients – and then integrate the product over time. The resulting time dependent function is fit to measured strain data to determine the phenomenological fit coefficients included in $J(t)$. Figure 10 shows the graph of the compliance function at different temperatures. The creep compliance clearly increases with increasing temperatures due to larger creep strains.

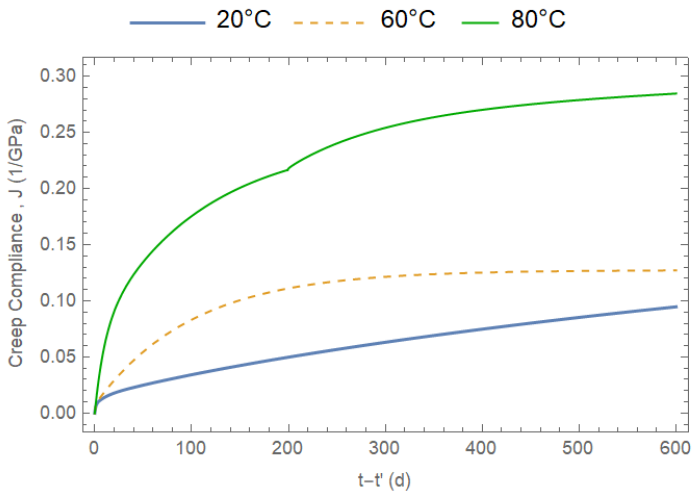

Figure 10. Creep compliance functions at 20°C, 60°C and 80°C calculated using constitutive equation.

Evaluation of Drying Creep in Mortar Experiments

As stated previously, the presence of free shrinkage strains in the adhesive-backed aluminum foil coated samples indicated that there was likely some external drying or self-desiccation (internal drying). Any external or internal drying would result in the presence of drying creep. Drying creep is the creep, in addition to basic creep (i.e., creep with no moisture change in the pore network), resulting under conditions of a change in moisture content of the loaded specimen. Drying creep is also referred to as the Pickett effect (Pickett 1942).

To assess significance of the drying creep component in our experiments, the B4 model was used. Using the model, the internal moisture history of the samples was back calculated using the constitutive equation relating the free strain to the average humidity history in the B4 model (Bažant et al. 2014). Then using the mix design composition and humidity profile, the basic and drying creep components of compliance were subsequently estimated using the B4 model in order to assess their relative magnitude. According to the B4 model, the creep compliance of a specimen exposed to the atmosphere and undergoing drying during a creep test can be expressed using

$$J(t,t') = q_1 + R_T C_0(t,t') + C_d(t,t',t_0), \quad (3)$$

where, q_1 is the instantaneous strain due to unit stress, $C_0(t,t')$ is the compliance due to basic creep, $C_d(t,t',t_0)$ is the additional compliance due to drying, and R_T is a multiplicative factor for basic creep at elevated temperatures. Bažant's B4 model illustrates a step-by-step procedure to calculate the basic and drying creep compliance functions (Bažant et al. 2014).

The total compliance function was obtained using eq. (3). Figure 11 depicts a comparative representation of the total creep compliance and the basic and drying creep compliance components at 20ºC, 60ºC and 80ºC, as predicted by the B4 model.

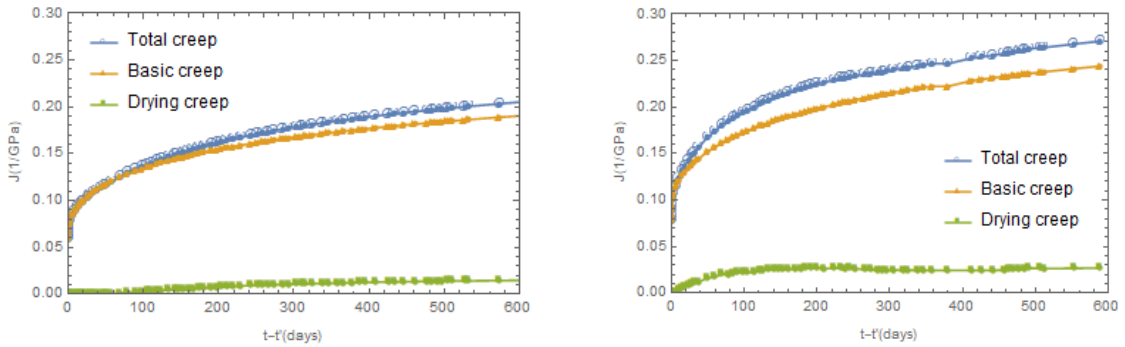

(a) 20ºC (b) 60ºC

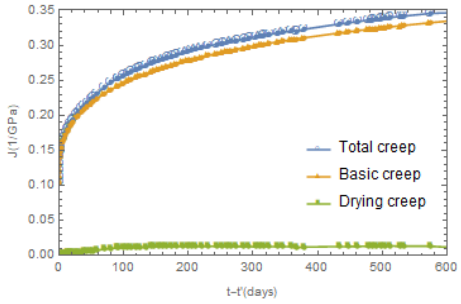

(c) 80ºC

Figure 11. B4 model used to depict the negligible impact of drying creep compliance in the calculation of total creep compliance.

From Figure 11, it is clear that the compliance due to drying is negligible compared to the total compliance function. The compliance function obtained from the creep experiments may thus be approximated as entirely due to basic creep compliance.

Creep Compliance Master Curve for Cement Mortar using TTS Principle

The basic creep compliance curves obtained at 20°C, 60°C and 80°C by fitting the experimental data using the constitutive equation method were plotted on a logarithmic time axis. All creep compliance curves were similar shapes, implying that the material was thermorheologically simple. Hence the creep compliance curves at 60°C and 80°C were shifted laterally to the right using the TTS principle to obtain a creep compliance master curve at room temperature (20°C) as shown in Figure 12.

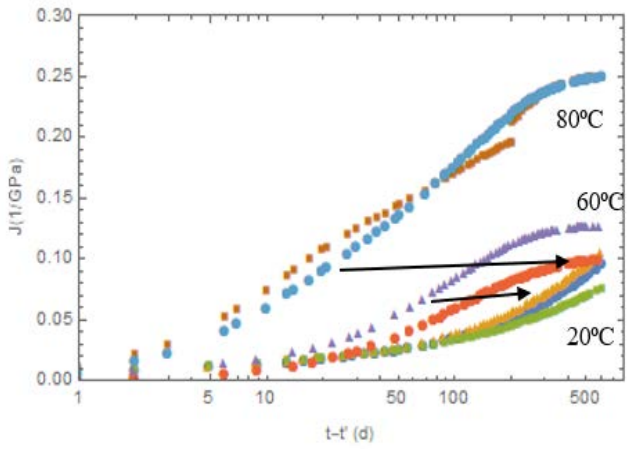

Figure 12. Creep compliance functions at 60°C and 80°C shifted along the logarithmic time axis to produce a creep compliance master curve at 20°C.

The temperature dependent shift factor, β_{Tc} that is needed to shift the curve laterally is calculated as

$$\beta_{Tc} = \frac{t}{t_r}, \tag{4}$$

where t is the present time and t_r is the reduced time. In this study, a β_{Tc} value of 4 was calculated for 60°C and 37 for 80°C to shift the creep compliance data from higher temperatures to 20°C reference temperature (β_{Tc}=1 at 20°C). A creep compliance master curve was obtained to predict creep of cement mortar for up to 22,500 days ~ 60 years using creep experiments performed for 600 days. The shifted data was fitted into a five-unit logarithmic chain shown in equation 9. The unit of creep compliance has units of 1/GPa.

$$J(t) = 0.03055 Log\left[1+\frac{t}{10000}\right] + 0.01273 Log\left[1+\frac{t}{1000}\right] + 0.03434 Log\left[1+\frac{t}{100}\right] - 3.9327 x10^{-10}$$
$$Log\left[1+\frac{t}{10}\right] + 0.00248 Log\left[1+t\right] \tag{5}$$

The creep compliance master curve is presented in Figure 13. The master curve allows for predicting creep in structures for several decades beyond the range of the original results obtained using laboratory creep experiments.

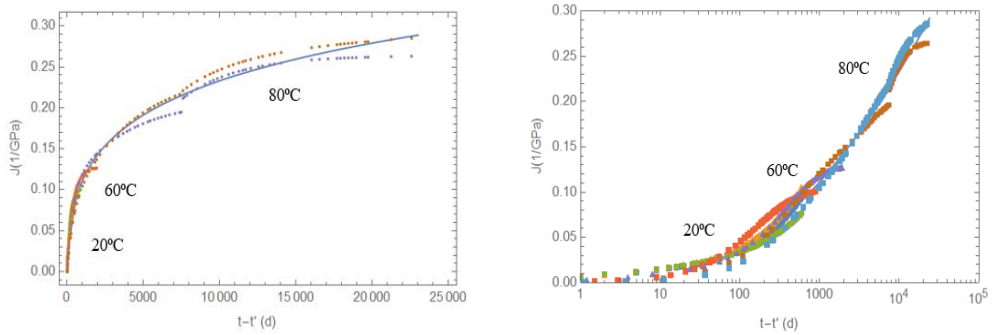

(a) (b)

Figure 13. Creep compliance master curve in (a) normal time scale and (b) logarithmic time scale.

2.3 Confined Creep Test

2.3.1 Literature review

Though creep of concrete has been a subject of interest for several decades, attention has mainly been devoted to creep under a uniaxial stress condition. However, in reinforced and prestressed structures, a three-dimensional state of stress generally exists, which can complicate the response of the structure. To understand the behavior of concrete under multiaxial compression, the Poisson's ratio of the viscoelastic material plays a crucial role to determine the long-term deformation response and durability performance of concrete (Bernard et al., 2003).

Some investigators have studied the viscoelastic/viscoplastic Poisson's ratio (VPR) of concrete, but the results reported from different studies are contradictory. For example, it has been suggested that VPR is an increasing, decreasing, and constant function of time in separate studies. Such uncertainty arises mainly from the fact that the VPR is measured or calculated differently by different researchers. Ross was the first to conduct creep tests on concrete under 2D loading and suggested that the creep Poisson's ratio (CPR)[2] is close to zero (Ross, 1954). His experiments showed that creep in the direction of major stress in 2D testing reaches a magnitude of the same order as that under simple 1D stress of same intensity. A few years later, Gopalakrishnan reported that under multiaxial stress conditions, the CPR was lower than the uniaxial Poisson's ratio and that there was no variation in CPR with time (Gopalakrishnan et al., 1969). The CPR was calculated separately for each direction using the knowledge of the uniaxial compliance. Gopalakrishnan also argued that the CPR was a function of the magnitude of stress.

[2] Note that CPR is determined by the negative ratio of transverse to axial strains in a constant stress (creep) test. As will be noted later in the paper, CPR is not generally equivalent to VPR.

Jordaan and Illston calculated CPR as the ratio of the total mechanical strains (i.e., the sum of elastic and creep strains) in the axial and lateral directions (Jordaan and Illston, 1969). They proposed four different expressions for calculating CPR under different loading conditions (uniaxial, biaxial, triaxial with uniaxial system, triaxial with octahedral shear stresses). The effective Poisson's ratio for all cases remained constant and equal to the Poisson's ratio in an elastic state (Jordaan and Illston, 1969). In 1974, Parrott measured the lateral strains from uniaxial tests on cement paste to determine the Poisson's ratio (Parrott, 1974). He used the creep strains (the total strain minus the elastic and shrinkage strains) to calculate the CPR. The CPR was found to be a constant value equal to 0.13 (Parrott, 1974). Kesler found that the CPR of concrete that was sealed during loading to be almost equal to the elastic Poisson's ratio, however it was considerably smaller if allowed to dry under load (Kesler, 1977). Lakes demonstrated that composite structures may exhibit increasing or decreasing Poisson's ratio with time (Lakes, 1992). He also proposed that time dependent VPR need not be monotonic in nature, where a composite can be constructed that can have a decreasing Poisson's ratio with time initially followed by an increasing function. Hilton cited five different expressions for time-dependent Poisson's ratio and identified VPR's strong dependence on stress histories (Hilton, 2001). Grasley and Lange computed the VPR of sealed cement paste using the correspondence principle. They found that under multiaxial loading, the VPR of cement paste is relatively constant with time and then gradually increases as dilatational compliance comes to a halt (Grasley and Lange, 2007).

More recently in 2015, Aili used various multiaxial creep test data from literature to show the difference between the CPR and relaxation Poisson's ratio (RPR – equivalent to the VPR). In spite of the two Poisson's ratio not being equal (Tschoegl et al. 2002; Lakes and Wineman, 2006) the initial and long-term asymptotic values and their corresponding time derivatives were found to be the same (Aili et al., 2015). In another study, Aili found the VPR for a mature concrete to be constant and ranging between 0.15 and 0.20 (Aili et al., 2016). Charpin conducted a 10-year concrete creep study under uniaxial and biaxial conditions in which the evolution of the CPR was discussed. Their experimental data showed that the assumption of a constant Poisson ratio for concrete is reasonable (Charpin et al., 2015). In 2017, Charpin and Sanahuja established through examples, both theoretical and practical, that any evolution of Poisson's ratio: increasing, decreasing or non-monotonic is possible for concrete (Charpin and Sanahuja, 2017). In summary, there is a large scatter in the reported VPR from different studies at room temperatures. A possible reason that could partly explain this large scatter in data is that the experiments were performed under varying test conditions. Also, the laboratory measurement of axial and lateral strains is challenging as they highly depend on the resolution of strain gages used. Overall, these conditions make multiaxial creep tests strenuous and time-consuming, thereby serving as a motivation for researchers to develop more effective methods to evaluate VPR.

Data on the Poisson's ratio of concrete at elevated temperatures are scarce and limited. At ambient temperature, the Poisson's ratio of concrete can vary between 0.15 and 0.20 (Atheel, 1981; Aili et al., 2016). A study by Ehm in 1985, suggests that the Poisson's ratio decreases with

increasing temperatures due to weakening of the microstructure by breakage of bonds at higher temperatures (Ehm, 1985). For a concrete under confining pressure, as it would be in many nuclear power plant concrete structures, it has been hypothesized that Poisson's ratio at elevated temperature would be about the same as at room temperature (NRC, 2010).

In the current study, the authors utilize a confined creep test that can fully capture the 3D constitutive properties of cement mortar in a single experiment. The confined creep test allows the simultaneous measurement of bulk and shear compliance, which is used to determine the uniaxial compliance and VPR through intermodulus conversion via the correspondence principle (Grasley and Lange, 2007).

2.3.2 Experimental Design

Mix Design

The cement mortar mix design used for the confined test is the same as that used in the uniaxial creep test. The mixture proportions are detailed in Table 1 of Section 2.2.3.

Confined Creep Test Setup

The confined creep test was conducted in the same miniaturized creep frame as discussed in section 2.2.3, with the exception that the cement mortar sample was confined in a 304L stainless steel confining tube of 2 mm (0.07 in.) thickness (54 mm outer diameter and 50 mm inner diameter) and 100 mm (4 in.) height. Both ends of the confining tube were sealed using tightly fitted caps. After 24 hours, the end caps were removed, and the sample was pushed slightly outside the tube on either end separately to smoothly cut the surface using a diamond blade wet saw. This procedure ensures that the bond between the sample and the confining tube is broken and the contact between them can be approximated as frictionless. Apart from the embedded vibrating wire gage at the center of the sample for measuring axial strain, four sets of foil strain gages (C2A-13-250LW-120) from Micro Measurements were mounted on the outer radial surface of the steel tube to measure hoop strain. The foil strain gages were placed diametrically opposite to each other and in the circumferential direction. A steel loading block with a diameter of 49 mm (1.9 in.) and height of 50 mm (1.9 in.) was placed on both ends of the sample. The loading block diameter was slightly less than the inner diameter of the confining steel tube so that it can easily slide through the tube while also ensuring uniform compressive stress throughout the sample cross-section. The axial strain from the vibrating wire gage as well as the load readings from the load cell were recorded every 30 minutes using a CR300 Data logger, AM16/32B Multiplexer and a 2-Channel Vibrating-Wire Analyzer (AVW200) from Campbell Scientific. The foil strain gages that read hoop strain were connected to a Student D4 data acquisition system from Micro Measurements using quarter bridge circuits. The cement mortar specimens were cured at room temperature for 28 days before starting the test. At 28 days, the samples were loaded using a hydraulic jack to a constant load of approximately 1905 kg (4200 lbs), which corresponded to 25% of 28-day compressive strength of mortar; f'_c = 37.23 MPa (5400 psi) at 28 days.

Figure 14. Confined creep test setup using the miniaturized creep frame placed inside an environmental chamber maintaining constant temperature and humidity.

Computation of Viscoelastic Material Properties

The confined creep apparatus was first utilized by Ma and Ravi-Chandar and subsequently by Park and Roy (Ma and Ravi-Chandar, 2000; Park and Roy, 2004) to obtain the bulk and shear linear viscoelastic compliance functions simultaneously on the same specimen, under constant environmental conditions. Grasley and Lange (Grasley and Lange, 2007) were the first to use such an experimental setup on cementitious materials when they studied cement paste creep at room temperature. In this study, the confining steel cylinder with an inner radius a of 25 mm (1 in.), an outer radius b of 27 mm (1.06 in.) and a height h of 100 mm (4 in.) was used. The material properties of the confining steel cylinder are known. The Young's modulus of stainless steel (E^c) is 193 GPa and Poisson's ratio (ν^c) is 0.29. The confined test set-up in the cylindrical polar coordinate system is shown in Figure 15.

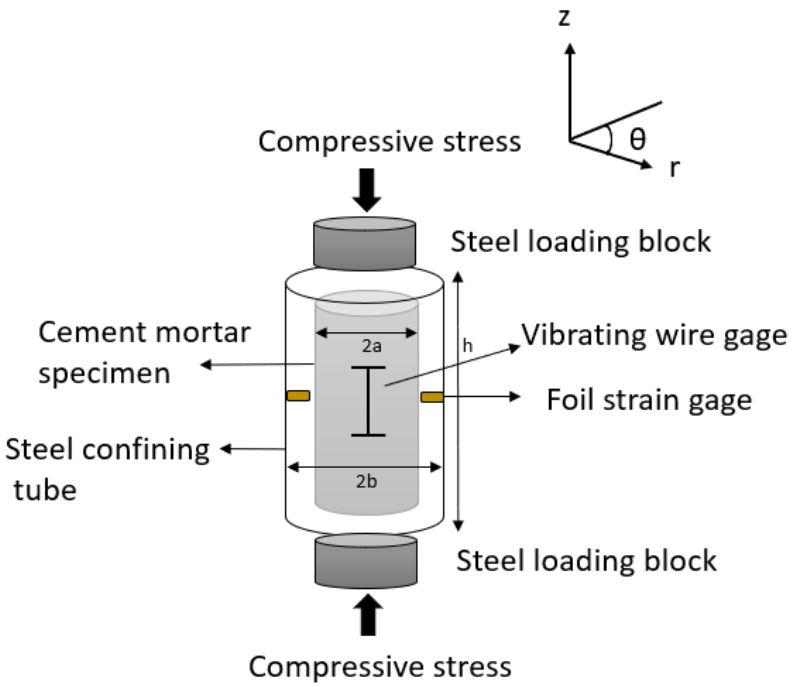

Figure 15. Confined compressive creep test set-up with inner radius a of 25 mm (1 in.), an outer radius b of 27 mm (1.06 in.) and a height h of 100 mm (4 in.).

The axial stress, σ_{zz}, experienced by the cement mortar sample under a constant load was calculated by dividing the load applied by the cross-sectional area of the sample such that

$$\sigma_{zz} = \frac{\text{Load applied}}{\pi a^2}. \tag{6}$$

The total axial strain as a function of time, $\varepsilon_a(t)$, was recorded using a vibrating wire gage. The mechanical axial strain, $\varepsilon_{zz}(t)$, was calculated as

$$\varepsilon_{zz}(t) = \varepsilon_a(t) - \varepsilon^{sh}(t), \tag{7}$$

where, $\varepsilon^{sh}(t)$ is the free shrinkage strain. A companion specimen of the same dimension and confinement was used to record the free strain using embedded vibrating wire gage.

When an axial stress is applied, the specimen tends to expand in the transverse direction due to Poisson's effect, resulting in a positive (or tensile) radial displacement (u_r). However, the (8) confining cylinder restrains this deformation with a negative (or compressive) radial stress (σ_{rr}).

From the continuity conditions at the interface

$$\sigma_{rr}(a) = \sigma_{rr}^{c}(a) \tag{9}$$

and

$$u_r(a) = u_{rr}^{c}(a), \tag{10}$$

where superscript *c* denotes confining cylinder.

By measuring the hoop strain, (ε_h), on the outer surface of the confining cylinder using the foil strain gages, the radial displacement and radial stress of the confining cylinder on the inner surface, u_r^c and σ_{rr}^c, respectively, were computed by the Lamé solution as

$$u_r^c = \frac{\varepsilon_h}{2}\left[\left(1-\nu^c\right)a + \left(1-\nu^c\right)\frac{b^2}{a}\right] \tag{11}$$

$$\sigma_{rr}^{c}(t) = -\frac{b^2-a^2}{2a^2}E^c\varepsilon_h(t). \tag{12}$$

The stress induced radial strain, $\varepsilon_{rr}(t)$, was calculated by dividing the radial displacement, u_r^c, by inner radius, a, and subtracting the free shrinkage strain such that

$$\varepsilon_{rr}(t) = \frac{\varepsilon_h(t)}{2}\left[\left(1-\nu^c\right) + \left(1-\nu^c\right)\frac{b^2}{a^2}\right] - \varepsilon^{sh}(t). \tag{13}$$

The axisymmetric strain-displacement relation gives $\varepsilon_{rr} = \varepsilon_{\theta\theta}$ and equilibrium equations require that radial and hoop components of stress are equal, i.e., $\sigma_{rr} = \sigma_{\theta\theta}$, where r and θ represent radial and tangential components, respectively. Since eqns. (6), (7), (12) and (13) representing the axial stress, axial strain, radial stress and radial strain, respectively, form the principal components of stress and strain, the full 3D constitutive response of the material was obtained from the confined experiment.

The deformation of the specimen was then separated into dilatational and deviatoric components. The volumetric stress, σ_m, in the specimen was determined as one-third the sum of the three normal stress components such that

$$\begin{aligned}\sigma_m(t) &= \frac{\sigma_{kk}(t)}{3} = \frac{1}{3}\left[\sigma_{zz}(t) + \sigma_{rr}(t) + \sigma_{\theta\theta}(t)\right] \\ &= \frac{1}{3}\left[\sigma_{zz}(t) + 2\sigma_{rr}(t)\right].\end{aligned} \tag{14}$$

Since the deformation gradients are small, the volumetric strain, ε_{kk}, was approximated as the sum of three normal strains such that

$$\varepsilon_{kk}(t)=\left[\varepsilon_{zz}(t)+\varepsilon_{rr}(t)+\varepsilon_{\theta\theta}(t)\right] \\ =\left[\varepsilon_{zz}(t)+2\varepsilon_{rr}(t)\right]. \tag{15}$$

The deviatoric stress, τ_e, and deviatoric strain, γ_e, from the confined compression test were computed using

$$\tau_e(t)=\frac{1}{\sqrt{3}}\left|\sigma_{zz}(t)-\sigma_{rr}(t)\right| \tag{16}$$

and

$$\gamma_e(t)=\frac{2}{\sqrt{3}}\left|\varepsilon_{zz}(t)-\varepsilon_{rr}(t)\right|. \tag{17}$$

The constitutive equations for a non-aging, linear viscoelastic material, expressed in terms of dilatational and deviatoric components, is given by

$$\varepsilon_{kk}(t)=\int_0^t B(t-t')\frac{\partial\sigma_m(t')}{\partial t'}dt' \tag{18}$$

and

$$\gamma_e(t)=\int_0^t L(t-t')\frac{\partial\tau_e(t')}{\partial t'}dt', \tag{19}$$

where $B(t)$ and $L(t)$ are the bulk and shear compliances of the material, respectively. Here t refers to the present time and t' is the dummy integration time variable. Once the bulk and shear compliances were found, the uniaxial creep compliance, $J(t)$, was computed using intermoduli conversion via the correspondence principle such that

$$\overline{E}(s)=\frac{9\overline{K}(s)\,\overline{G}(s)}{3\overline{K}(s)+\overline{G}(s)} \tag{20}$$

and

$$\overline{J}(s).\overline{E}(s)=\frac{1}{s^2}, \tag{21}$$

where $\overline{E}(s)$, $\overline{K}(s)$ and $\overline{G}(s)$ are Laplace transformed relaxation, bulk and shear modulus functions, respectively, and s is the complex variable in the Laplace domain. The Laplace transformed uniaxial creep compliance and the corresponding Laplace transformed relaxation moduli are each related as shown in eqn. (21).

2.3.3 Results and Discussion

Initial Loading

The stress/strength ratio applied was 0.25, which lies within the linearity range of the material according to the study by Neville and Dilger, who demonstrate that non-linearity of cement mortar arises only beyond a stress/strength ratio of 0.80 (Neville and Dilger, 1970). Figure 16 shows that when the compressive axial load was applied on the sample, the compressive axial strain was accompanied by an increase in tensile hoop strain.

As outlined earlier, using the measured hoop strain and material properties of the confining cylinder, the principal components of stress and strain were determined. Figure 17 shows the volumetric (or bulk) and shear stresses plotted against their corresponding volumetric (or bulk) and shear strains at 20ºC.

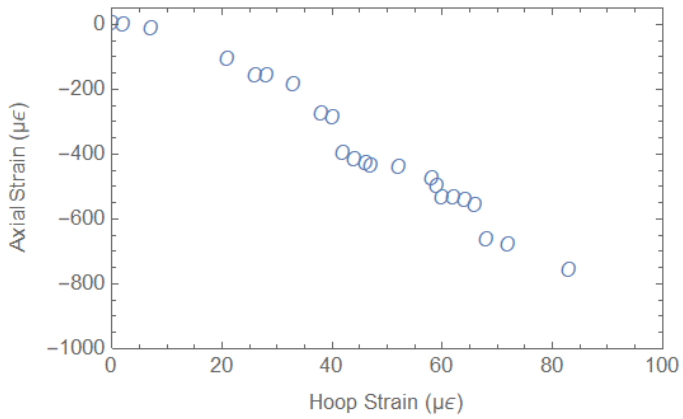

Figure 16. Variation of axial strain and hoop strain at initial loading.

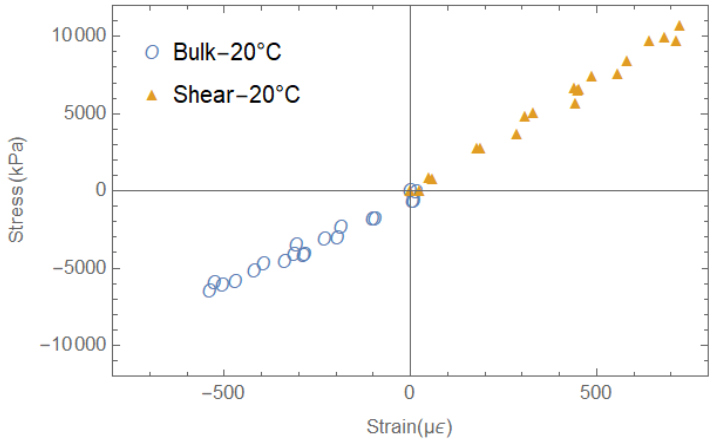

Figure 17. Volumetric (or bulk) and shear stress-strain data at initial loading at 20ºC.

It is clear from Figure 17 that the samples exhibited linear elastic behavior at the time of initial loading. The slope of these curves represents the elastic bulk and shear modulus of cement mortar at the respective temperatures. The elastic bulk modulus, *K*, was calculated to be 13.6 GPa and the elastic shear modulus, *G*, was calculated to be 11.6 GPa at 20ºC. Using the intermodulus conversion, the elastic Young's modulus, *E*, was calculated to be 27.0 GPa. To validate the calculations, the *E* of three mortar cylinders (100 mm x 200 mm) were measured in accordance with ASTM C469. The average measured Young's modulus of the samples at 28 days was 25.4 ± 1.1 GPa. The predicted and measured elastic modulus values were hence found to be in reasonable agreement.

Determining $B(t)$ and $L(t)$ from Confined Creep Test

The deformation from the confined experiment was separated into dilatational and deviatoric parts for the determination of dilatational and deviatoric compliance functions. Although the axial load was maintained relatively constant throughout the experiment, the volumetric and shear stress varied as a function of time. Since volumetric and shear strains are also evolving along with the corresponding stresses during the experiment, a more informative way to assess the confined creep test results is to determine the bulk and shear compliance functions, since these functions are ostensibly independent of either stress or strain history. In order to determine $B(t)$ and $L(t)$ using the constitutive expression given in eqns. (18) and (19), it is necessary to fit the measured stress history to a time dependent function, take the derivative of that function (in terms of the dummy time variable), multiply the derivative by a presumed function for $B(t)$ and $L(t)$ – including phenomenological fit coefficients – and then integrate the product over time. The resulting time dependent function was fit to the measured strain data to determine the phenomenological fit coefficients included in $B(t)$ and $L(t)$. This is the most fundamentally accurate method to determine the compliance functions. Figure 18 shows the graph of the compliance functions.

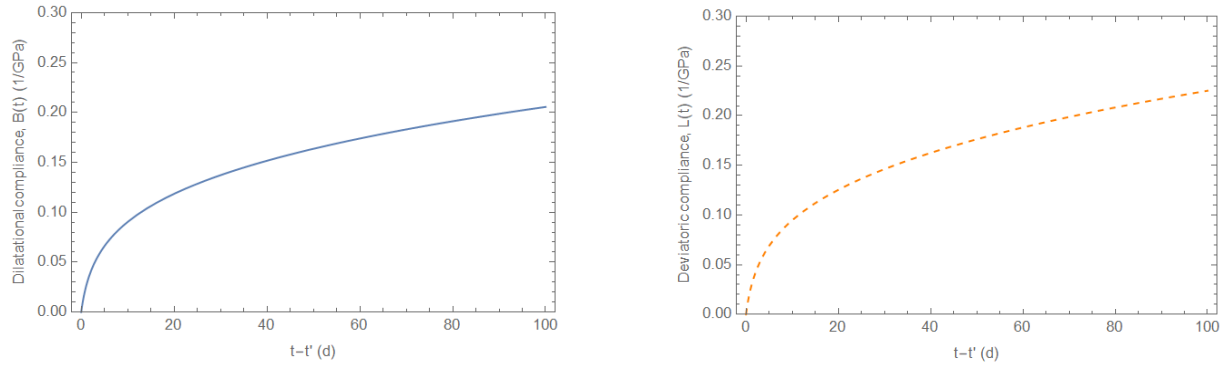

(a) Bulk compliance (b) Shear compliance

Figure 18. The bulk and shear compliance functions calculated using the constitutive equation.

$$B(t) = 0.06217 Log[1+t/100] + 1.48787 * 10^{(-10)} Log[1+t/10] + 0.03519 Log[1+t] \quad (22)$$

$$L(t) = 0.08391 Log[1+t/100] + 2.08211 * 10^{(-10)} Log[1+t/10] + 0.03616 Log[1+t] \quad (23)$$

Once the $B(t)$ and $L(t)$ were computed, they were transformed in to the Laplace domain to find the Laplace transformed bulk modulus, $\overline{K}(s)$ and shear modulus, $\overline{G}(s)$ from the relations

$$\overline{B}(s).\overline{K}(s) = \frac{1}{s^2} \quad \text{and} \quad \overline{L}(s).\overline{G}(s) = \frac{1}{s^2}.$$

The Laplace transformed relaxation modulus, $\overline{E}(s)$, and subsequently the Laplace transformed uniaxial creep compliance, $\overline{J(s)}$, were found using the intermodulus conversion expression shown in eqn (21). The inverse Laplace transform was then used to determine the compliance in the time domain. A graph depicting the predicted compliance through the intermodulus conversion compared to the measured compliance from uniaxial creep data is shown in Figure 19. It can be seen that the predicted compliance was reasonably close to the measured compliance data.

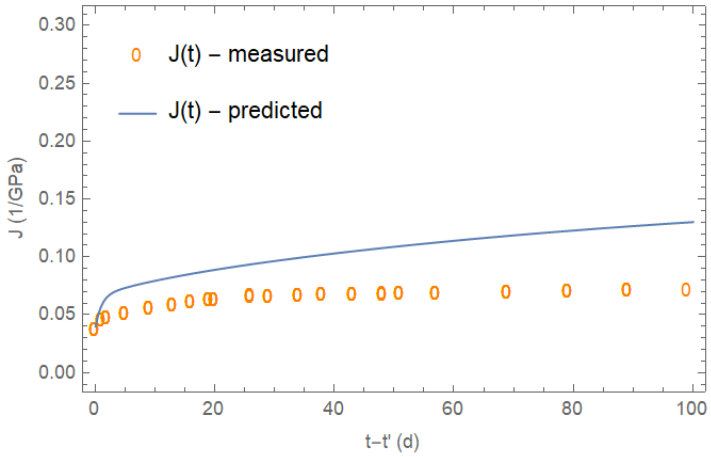

Figure 19. The predicted uniaxial creep compliance using intermodulus conversion.

Viscoelastic Poisson's ratio

As alluded to previously, there is contradiction in the literature regarding the measurement and prediction of VPR of concrete with time. This uncertainty arises mainly from the way researchers define the VPR function. As shown by Kassem et al. (2013), in a displacement controlled experiment such as a stress relaxation test where the input axial strain, ε_{11}, is a step function represented as $\varepsilon_{11}(t) = \varepsilon_0 H(t)$, where ε_0 is a constant and $H(t)$ is the Heaviside function, the output transverse strain $\varepsilon_{22}(t)$ is given by

$$\varepsilon_{22}(t) = -\nu(t)\varepsilon_0. \quad (24)$$

VPR can then be calculated as

$$\nu(t) = -\frac{\varepsilon_{22}(t)}{\varepsilon_0} \quad . \tag{25}$$

On the other hand, in a load controlled experiment, such as a creep test where the input axial stress σ_{11} is a step function represented as $\sigma_{11}(t) = \sigma_o H(t)$, where σ_0 is a constant, the output axial strain is given by

$$\varepsilon_{11}(t) = \int_0^t D(t-t') \frac{\partial \sigma_{11}(t')}{\partial t'} dt' \tag{26}$$

The corresponding output transverse strain is given by

$$\varepsilon_{22}(t) = -\int_0^t \nu(t-t') \frac{\partial \varepsilon_{11}(t')}{\partial t'} dt' \quad . \tag{27}$$

In order to determine $\nu(t)$ using eqn. (27), it is necessary to fit the measured axial strain history to a time dependent function, take the derivative of that function (in terms of the dummy time variable), multiply the derivative by a presumed function for $\nu(t)$ – including phenomenological fit coefficients – and then integrate the product over time. The resulting time dependent function is then fit to the measured transverse strain data to determine the phenomenological fit coefficients included in $\nu(t)$. Many researchers have determined a "creep Poisson's ratio" for concrete by neglecting the history dependence denoted by the convolution integral in eqn. (27); such a creep Poisson's ratio is a function of the stress or strain history of the material and is thus not a constitutive property like the VPR determined in eqn. (25) or (27).

In case of a specimen subjected to a 3D state of stress, such as a confined creep test, the VPR may be determined using the intermoduli conversion in the Laplace domain according to

$$s.\bar{\nu}(s) = \frac{3\bar{K}(s) - 2\bar{G}(s)}{6\bar{K}(s) + 2\bar{G}(s)} \quad . \tag{28}$$

In this study, using the Laplace transformed bulk and shear modulus, the Laplace transformed VPR was determined from eqn. (28). Then, the Laplace transformed VPR was inverted to the time domain to obtain the VPR of the viscoelastic material (see Figure 20). *Mathematica* was used to perform the analyses.

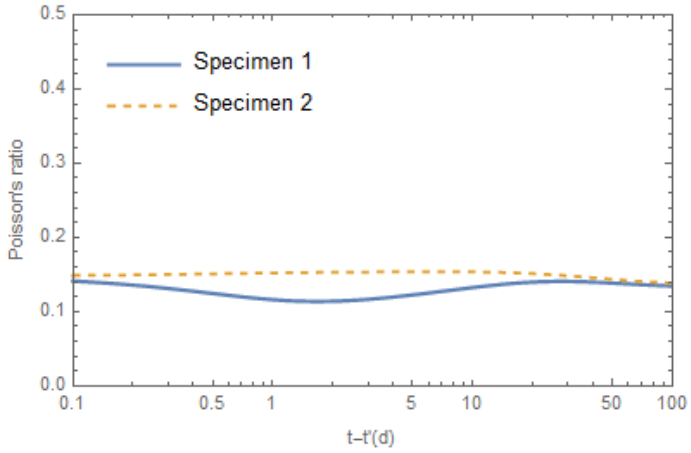

Figure 20. Variation of viscoelastic Poisson's ratio of cement mortar as a function of time.

The viscoelastic Poisson's ratio of cement mortar was found to be a relatively constant value of 0.14 at 20ºC over a period of 100 days after initial loading. If the rate of decay of dilatational and deviatoric compliance functions show a similar trend (i.e., same rate at all times), then VPR can be considered a constant function with time. The same phenomenon is discussed by Bernard et al. and Grasley and Lange, where the reduction in porosity in the sample was suggested to decrease the rate of change of dilatational compliance with time versus the rate of change of deviatoric compliance (Bernard, 2003; Grasley, 2007).

2.4 Concrete Creep Test

2.4.1 Literature review

Concrete creep has been a topic of interest for several decades especially due to the increasing use of prestressed concrete as the prime structural material in the construction of pressure vessels in nuclear reactors (Nasser and Neville, 1965). At room temperature, creep can be 3-4 times the initial deformation in the first 1-2 years and at elevated temperatures, the effects of creep cannot be ignored. In 1907, Hatt discovered that concrete under a constant load continued to slowly deform and named the phenomenon as creep (Hatt, 1907). Since then, several researchers have studied the behavior of concrete under uniaxial and multiaxial loading. The time-dependent deformation in concrete originates from the hardened Portland cement paste. The aggregates are typically assumed to be linearly elastic and do not contribute to creep.

Although numerous studies have looked into the creep response of concrete (Ross, 1954; Gopalakrishnan, 1968, McDonald, 1975; Kommendant et al., 1976; Kesler, 1977; Wittmann and Roelfstra, 1980; Bazant, 2001; Benjoudjema et al., 2005; Torrenti and Le Roy, 2015; Sellier et al., 2016) , there is limited literature that describes concrete's long-term basic creep behavior. Past work on long term creep includes that of Hanson (Hanson, 1953), Troxell (Troxell et al., 1958),

Browne (Browne and Blundell, 1969), Brooks (Brooks, 2005) and more recently Charpin (Charpin et al., 2018). Some challenges in conducting long-term creep experiments are reliability of creep frames without failing, stress decay over time and availability of personnel to monitor the test. As detailed in section 2.2, it is well known that concrete creep increases as a function of temperature. This introduces the possibility of predicting long-term creep at room temperature by measuring short-term creep at high temperatures using the TTS principle. Nasser and Neville made interesting observations in their study on concrete creep at elevated temperatures that the shape of creep curve with time is the same at elevated temperature as of normal temperature. Secondly, the linearity of stress-strength ratio is the same as room temperature for elevated temperature upto 96°C which indicates that increase in temperature not only enhances creep, but the mechanisms remain the same (Nasser and Neville, 1965). This validates that the TTS principle can be applied for concrete creep strains.

In this current sub-task, the experimental creep study on concrete samples at room and elevated temperature (i.e. 60°C) is detailed. Using B3 and B4 model, the drying component of creep was subtracted to obtain only basic creep of concrete. The modelled creep compliance will be compared to the simulated results in the next task to verify the applicability of upscaling technique from mortar creep compliance to concrete creep compliance. Finally, since creep strain has been speculated to contribute to structural failure (Bažant et al. 2012), split tensile tests were performed on virgin concrete as well as concrete that has undergone creep.

2.4.2 Experimental Design

Mix Design

The concrete mix design selected for the study is the same as the VeRCoRs mortar mix as detailed in section 2 with the addition of intermediate and coarse aggregates. River gravel used as intermediate aggregates was sieved to pass between 11 mm and 4 mm and Limestone used as coarse aggregate was sieved to pass between 16 mm and 8 mm. All the aggregates were dried for 24 hours before mixing. The same water to cement ratio (w/c) of 0.52 was maintained (SSD condition). The mixture proportions used are shown in Table 2 and referenced in EDF (EDF, 2014).

Table 2. Mixture proportions (SSD condition)

Materials	**Unit**	**Mix**
Cement (Type I/II)	kg/m^3 lb/yd^3	320 539
Fine aggregate 0/4 mm (River sand)	kg/m^3 lb/yd^3	837 1412

Intermediate aggregate 4/11 mm (River gravel)	kg/m^3 lb/yd^3	456 768
Coarse aggregate 8/16mm (Limestone)	kg/m^3 lb/yd^3	560 944
Water	kg/m^3 lb/yd3	167 282
Pozzolith 80	l/m^3 oz/yd^3	1.35 66

Sample Preparation

Creep Samples

Concrete was mixed in accordance with ASTM C192 and immediately cast into 100 mm x 200 mm (4 in. x 8 in.). DEMEC (Demountable Mechanical Strain gage) contact points for measuring strains on the outer edge of sample were drilled in the concrete mold before pouring the mix. The cylinders were filled in three equal increments and tapped after each increment to minimize air voids. Once filled, the concrete samples were retained in the mold to prevent moisture loss until just prior to the time of testing after 28 days. The demolded samples were immediately sealed with one layer of adhesive-backed aluminum foil to minimize drying. Two cylinders were connected end to end using sulfur capping compound and concrete plugs of 100 mm (4 in.) height were attached to both ends of the sample to ensure uniform compressive stress throughout the cross-section per the St. Venant's principle.

Compressive creep test was performed on concrete cylinders at 20ºC and 60ºC. The cylinders were loaded to 20% of their compressive strength, which was close to 12,000 lbs. Concrete can be assumed to behave linear viscoelastic upto 40% of its compressive strength (Neville et al., 1983). Strain readings were measured using DEMEC dial gage.

Free Strain Samples

In addition to the uniaxial concrete creep test, companion cylindrical specimens of same dimensions were fabricated to record the free strain due to shrinkage at each temperature for the entire duration of the creep test. The age and test conditions of these load-free specimens were the same as those used in the creep tests. DEMEC contact points were used to record the free strain with time.

Concrete Creep Test setup

Compressive creep test was performed on concrete cylinders at 20ºC and 60ºC. The concrete samples were loaded at 28 days of age using a hydraulic jack to a constant load of 540 kg (1200 lbs.) which corresponded to 20% of 28-day compressive strength of the concrete. At this loading age and stress magnitude, the mature concrete is approximated as a non-aging, linearly viscoelastic material.

The load was approximated as a stepwise load function given the very short time span of load application relative to the overall duration of the creep test. A load cell was used at the time of jacking the frame which was subsequently removed after the load application. The load was thus assumed to be constant throughout the entire duration of test. This is a reasonable assumption to make as the concrete frames unlike the miniaturized mortar creep frames have tougher springs that maintains the load constant. The creep strains from DEMEC points were recorded once a day for a week, then once a week for a month followed by once a month for a year. As alluded to earlier, creep tests were run at two different temperatures: 20°C (reference temperature) and 60°C. Two replicates of concrete samples were used at each temperature and were heated to the respective test temperature before starting the creep test (to avoid the accumulation of thermal strains during creep). The experiments were conducted in environmental chambers maintaining a constant temperature (Figure 21). The relative humidity was consistent at 50% in the 20°C chamber and below 10% in the 60°C chambers.

Figure 21. Uniaxial concrete creep test setup.

2.4.3 Results and Discussion

Concrete Mix Properties

The compressive strength ($f_c^{'}$) and elastic Young's modulus (E) of the concrete were measured at ages of 3, 7, 14, 28 and 90 days in accordance with the test procedures outlined in ASTM C39 and ASTM C469 respectively. Three replicates of the mortar samples were tested at each age. The evolution of mean values of $f_c^{'}$ and E of cement mortar with age is shown in Figure 22 along with the standard error for each measurement.

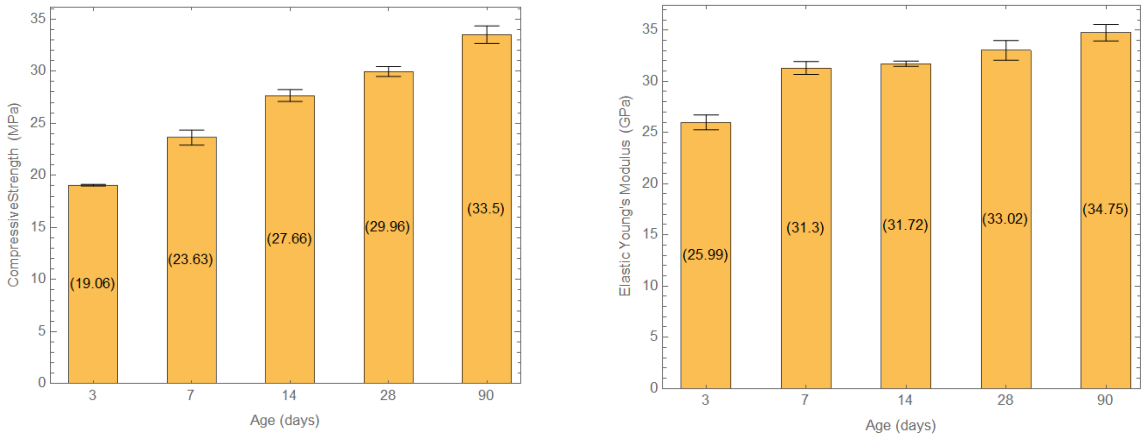

Figure 22. Average compressive strength and elastic Young's modulus of concrete at different ages along with the standard error for each measurement.

Concrete Creep Test

The stress on the concrete samples was calculated as a function of time using the constant load applied and the cross-sectional area of the samples. Figure 23 (a) shows a representative fitted stress function of a concrete sample at 20°C.

$$\sigma(t) = 8.722 + 0.0000112e^{-t} + 6.75*10^{-6}e^{\frac{-t}{10}} + 6.04*10^{-6}e^{\frac{-t}{100}} \quad (29)$$

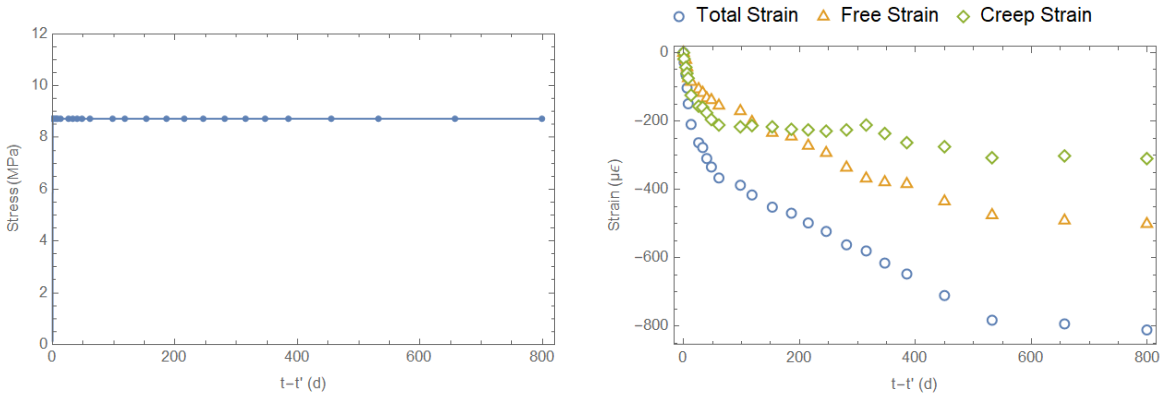

(a) (b)

Figure 23. (a) Fitted stress with respect to time under load for a sample at 20°C. (b) Graph showing total strain, free strain and creep strain for a sample under load as a function of time.

Figure 23 (b) shows the different components of strain in the concrete sample from a creep test. The strain readings represent the average strains recorded for the two replicate specimens. The DEMEC at the exterior of the sample records the total strain. The free strain reading was constantly monitored using DEMEC in an unloaded specimen at the same age and test conditions. Despite the fact that all samples were sealed with an aluminium foil to restrict drying, the free strain measured was mostly from drying shrinkage since autogenous shrinkage is unlikely in a mix design with 0.52 w/c ratio. If drying did occur in the samples during the test as anticipated, the measured creep strain is the sum of basic creep and drying creep in accordance to the Pickett effect. This issue will be addressed later in the study. The creep strain in Figure 23, which is the primary point of interest in this study, is the difference between the total strain and free strain.

It was observed that after 800 days, the creep strain at 60ºC was 1.6 times higher than that at 20ºC. These multipliers are similar to those recorded in existing literature. Nasser and Neville found that for samples with a stress-strength ratio of 35% loaded at 14 days of age and 15 months under load, the creep at 72ºC was 1.75 times greater than that at 21ºC. (Nasser and Neville 1965). In comparison, McDonald showed that for samples at a stress-strength ratio of 31% loaded at 90 days of age and 12 months under load, the compressive creep of concrete at 66ºC was 1.79 times that observed at 23ºC (McDonald 1975). Using the B4 model, creep at 60ºC was 1.69 times than the corresponding value at 20ºC. The average creep strains obtained at the different test temperatures are plotted in Figure 24.

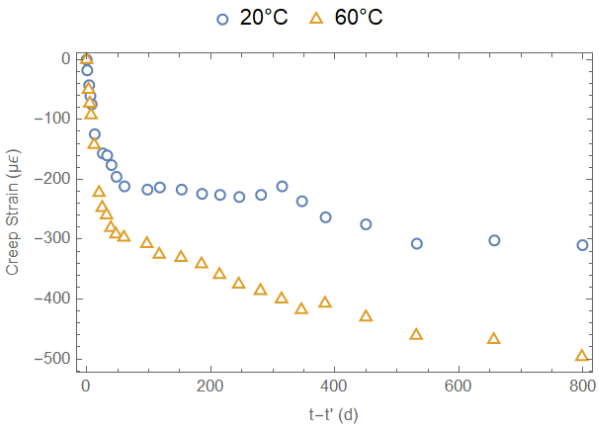

Figure 24. Creep strain of concrete at different temperatures.

A more informative way to compare the creep test results at varying temperatures (rather than plotting creep strain) is to assess the creep compliance, $J(t)$. Figure 25 shows the graph of the compliance function at different temperatures obtained using the eqn. (2) in section 2.2.4. The creep compliance clearly increases with increasing temperatures due to larger creep strains.

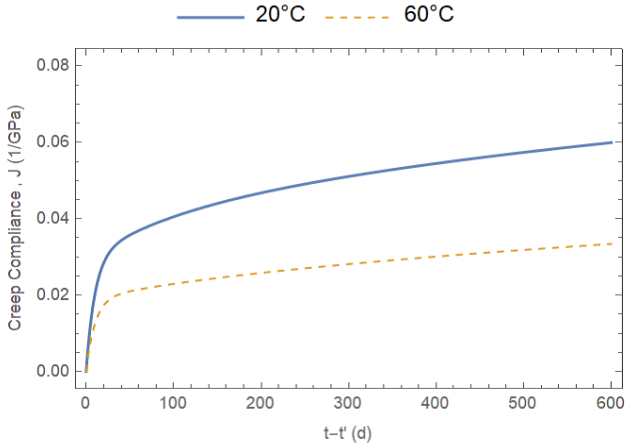

Figure 25. Creep compliance functions fitted using the constitutive equation at 20°C and 60°C.

Evaluation of the Significance of Drying Creep in Concrete Experiments

As explained in section 2.2.4, the total creep compliance was compared to the compliance obtained from B3 and B4 model.

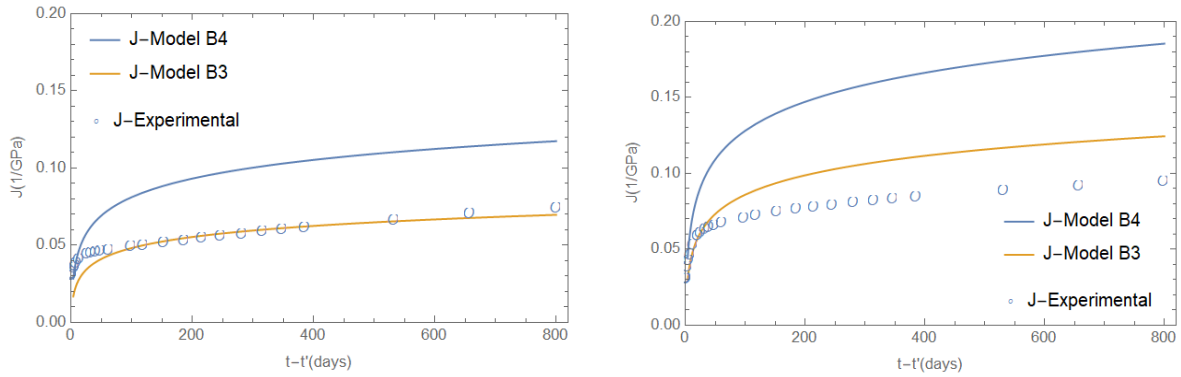

(a) 20ºC (b) 60ºC

Figure 26. Comparison of experimental data to B3 and B4 model

Since the B3 model fits more accurately with the experimental data, the significance of the drying creep in concrete test was assessed using the B3 model. Figure 27 depicts a comparative representation of the total creep compliance and the basic and drying creep compliance components at 20ºC and 60ºC as predicted by the B3 model.

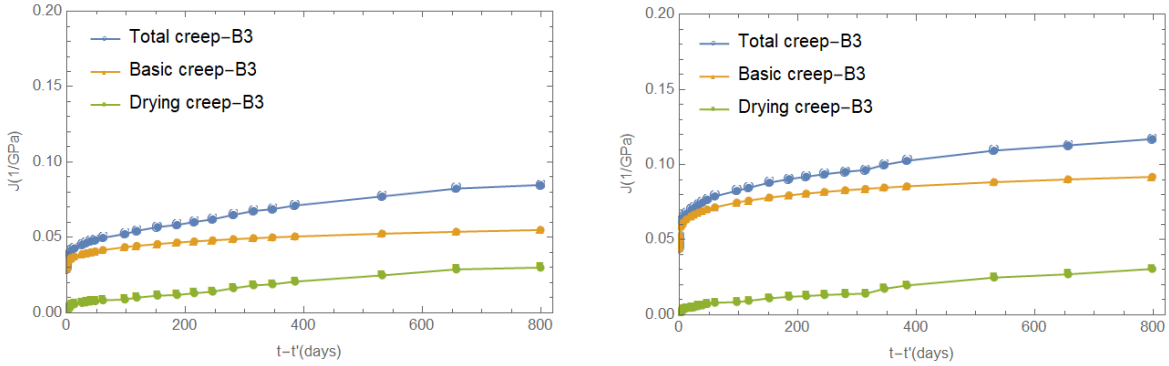

(a) 20ºC (b) 60ºC

Figure 27. B3 model used to depict the components of creep compliance (i) Total creep, (ii) Basic creep and (iii) Drying creep.

Creep Compliance Master Curve for Concrete using TTS Principle

Using the B3 model, the drying component of the creep was removed from the total experimental creep compliance to obtain the basic creep compliance. The basic creep curves obtained at 20°C and 60°C were plotted on a logarithmic time axis. It was observed that the creep compliance curves were similar shapes, implying that the material was thermorheologically simple. Hence the creep compliance curve at 60°C was shifted laterally to the right using the TTS principle to obtain a creep compliance master curve at room temperature (20°C) as shown in Figure 28.

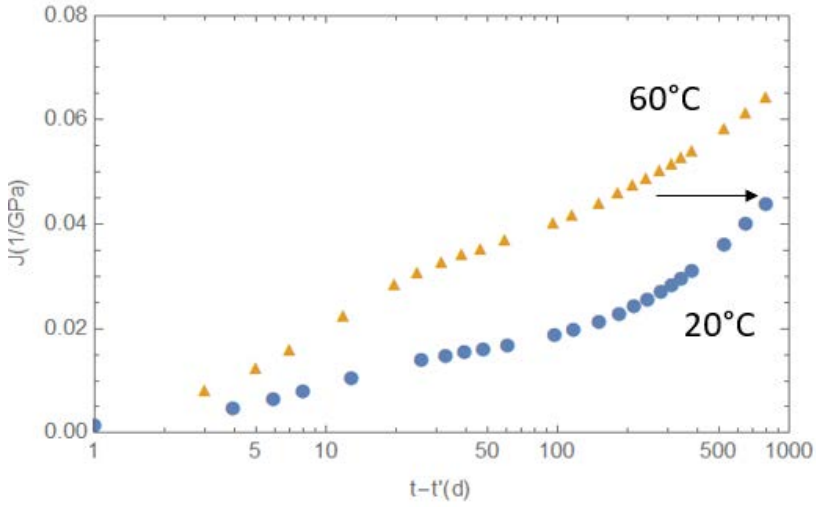

Figure 28. Basic creep compliance function at 60°C shifted along the logarithmic time axis to produce a basic creep compliance master curve at 20°C.

The temperature dependent shift factor, β_{Tc} that is needed to shift the curve laterally from 60°C to 20°C was calculated to be 12. A basic creep compliance master curve was obtained to predict creep of concrete for up to 9,800 days ~ 27 years using creep experiments performed for 800 days. The shifted data was fitted into a five-unit logarithmic chain shown in Equation 30. The creep compliance has units of 1/GPa.

$$J(t) = 0.0047 Log[1+t] + 2.8379*10^{-9} Log\left[1+\frac{t}{10}\right] + 7.1326*10^{-9} Log\left[1+\frac{t}{100}\right] + 6.9882*10^{-8} Log\left[1+\frac{t}{1000}\right] + 0.0047 Log\left[1+\frac{t}{10000}\right] \quad (30)$$

The creep compliance master curve is presented in Figure 29. The master curve allows for predicting creep in structures for several decades beyond the range of the original results obtained using laboratory creep experiments.

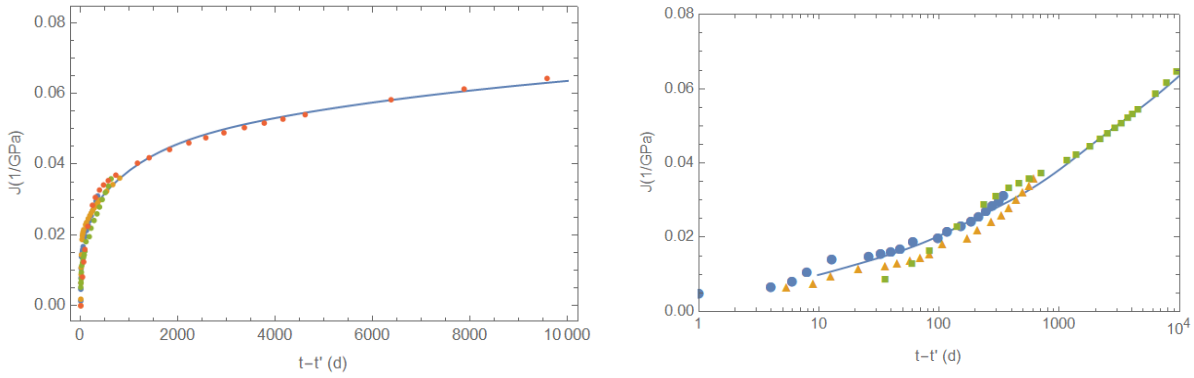

(a) (b)

Figure 29. Basic creep compliance master curve in (a) normal time scale and (b) logarithmic time scale.

Mechanical Properties

It is well known that concrete creep causes prestress losses in steel reinforcement with time. At the time of repairs, it is critical to be aware of the residual mechanical properties of the material that has undergone creep. Hence, in the current study the mechanical properties (i.e. dynamic modulus and tensile strength) of concrete is investigated.

Dynamic Modulus

At the end of creep tests, the concrete cylinders are pulled out and the dynamic modulus of the sample was evaluated in accordance to ASTM C215-19. The experiment is based on the principle of fundamental resonant frequencies using the impact resonance method. In this method, the specimen is struck with an impactor and the response is collected by an accelerometer. The accelerometer records the fundamental frequency of vibration. Two different modes of vibration were tested: transverse mode and longitudinal mode. In the transverse mode, the impact strikes the specimen on the circumferential surface whereas, in the longitudinal mode, the impactor strikes the surface on end of the sample longitudinally. Once the resonant frequencies are picked up, the dynamic Young's modulus of elasticity, E is calculated as follow:

$$E_T = \frac{1.6067 \cdot L^3 \cdot T \cdot M \cdot n^2}{d^4} \tag{31}$$

where, L is the length of specimen in meters, M is the mass of specimen in kg, n is the fundamental transverse frequency in Hz, d is the diameter of the specimen in meters and T is a correction factor that depends on radius of gyration, Length of specimen and Poisson's ratio.

$$E_L = \frac{5.092 \cdot L \cdot T \cdot M \cdot n'^2}{d^2} \tag{32}$$

where, n' is the fundamental longitudinal frequency in Hz.

The results from the experiment on concrete samples that were unloaded (free) and loaded (undergone creep) are shown in Figure 29. It can be seen that there is slight increase in stiffness (around 10%) on concrete samples that had undergone creep for 800 days.

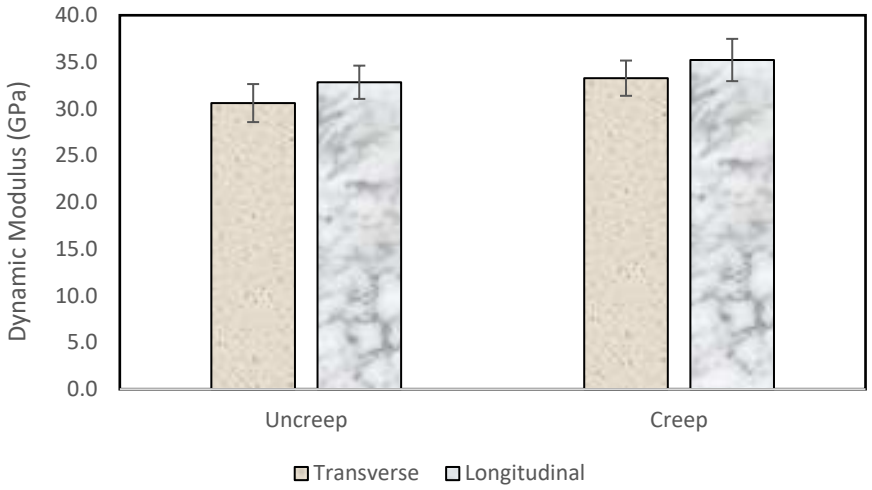

Figure 30. Transverse and Longitudinal Dynamic Modulus of concrete on loaded and unloaded specimens.

Split Tensile Test

Since the dynamic modulus test is a non-destructive test, the same samples were broken under split tensile test. The test was conducted in accordance to ASTM C496. Two bearing strips (usually plywood) 3 mm thick, 25 mm wide, and length equal to that of the specimen was used between the specimen and supplemental plates. Load was applied continuously at the rate of 0.7 to 1.4 MPa/min splitting tensile stress until failure. The maximum load applied at failure was noted. The splitting tensile strength of the specimen was calculated as:

$$T = \frac{2P}{\pi ld} \tag{33}$$

where, P is the maximum load applied causing failure in N, l is the length of the specimen in mm and d is the diameter of the specimen in mm. Figure 29 shows the experimental set up.

Figure 31. Experimental set up of splitting tensile test.

The test was conducted on unloaded (free) specimen as reference and on specimens under load for 800 days. Figure 29 shows the mean results of 4 cylinders tested in each category along with standard error. Though creep has not greatly affected the strength of the concrete, there is still a decrease in strength compared to virgin samples. Creep strains have been known to induce structural failure, especially when the stress levels are very high (Bažant et al. 2012).

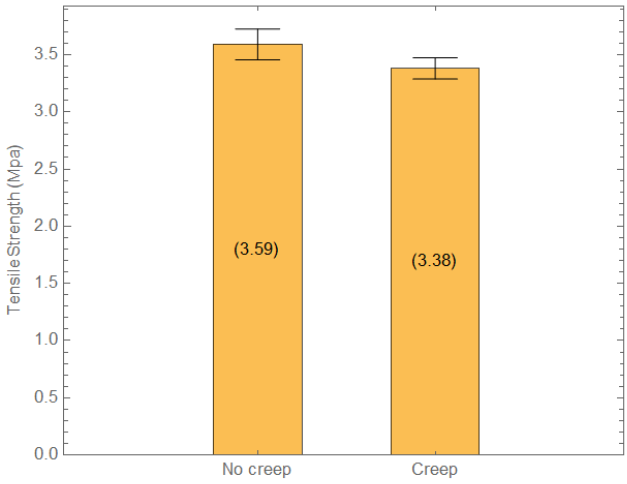

Figure 32. Splitting tensile strength of concrete specimens with no creep and creeped sample.

2.5 Conclusions

The primary contribution of this work is the development of a robust, experimentally validated model to predict creep in nuclear concrete structures for up to 60 years using short-term creep data thereby enabling a longer service life of critical facilities and early detection of structural failure.

The significant findings obtained as part of the study include the following:

- Creep increases as a function of temperature. The magnitude of creep strain of cement mortar increased by a factor of 1.50 and 2.40 at 60ºC and 80ºC, respectively, compared to the creep strain at 20ºC measured at 600 days.
- For the first time, the TTS principle was successfully used to generate a uniaxial creep compliance master curve to predict mortar creep response for up to 22,500 days (nearly 60 years) at a reference temperature of 20°C.
- By running creep tests at 80°C, creep at 20°C was predicted at 37 times the time duration of the 80°C test using temperature shifting.
- The confined creep test was used to determine the dilatational and deviatoric compliance functions from a single test.
- The viscoelastic Poisson's ratio of cement mortar was found to be a nearly constant value of 0.14 at 20ºC over a period of 100 days after initial loading.
- From the concrete creep test, uniaxial creep compliance master curve was developed that predicts concrete creep response for up to 9,800 days (nearly 27 years) at a reference temperature of 20°C.
- The Bažant B3 and B4 model was used to remove the drying creep component from the total creep, if any to obtain only the basic creep compliance.
- The concrete samples under creep showed an increase in stiffness (around 10%), whereas the split tensile strength showed a decrease in strength (around 6%) compared to the virgin samples.

References

1. Aili, A., Vandamme, M., Torrenti, J.M. and Masson, B.: Theoretical and practical differences between creep and relaxation Poisson's ratios in linear viscoelasticity. Mech. Time-Depend. Mater. **19** (4), 537-555 (2015).
2. Aili, A., Vandamme, M., Torrenti, J.M. and Masson, B and Sanahuja, J.: Time evolutions of non-aging viscoelastic Poisson's ratio of concrete and implications for creep of CSH. Cem. Conc. Res. **90**, 144-161(2016).
3. Atheel, E., Allos, L.H. and Martin.: Factors affecting Poisson's ratio for concrete. Bldg. Env. **16** (1), 1-9 (1981).

4. Baranikumar, A.: Prediction of Long-Term Creep for Nuclear Concrete Structures. Ph.D. Dissertation, Texas A&M University, College Station, TX (2020).
5. Bažant, Z. P.: Theory of Creep and Shrinkage in Concrete Structures: A Precis of Recent Developments. Reprinted from Mechanics Today, **2** (1), 1-93 (1975).
6. Bažant Z. P., Panula, L.: Practical prediction of time-dependent deformations of concrete. Mater. Struct. (RILEM, Paris) **11**, 307–316, 317–328, 415–424 (1978).
7. Bažant, Z. P.: Mathematical Modeling of Creep and Shrinkage of Concrete. Wiley, Chichester (1988).
8. Bažant, Z. P., and Xi, Y.: New test method to separate microcracking from drying creep: Curvature creep at equal bending moments and various axial forces. Proc., 5th International RILEM Symposium on Creep and Shrinkage of Concrete (ConCreep 5), held at U.P.C., Barcelona (1993).
9. Bažant, Z. P. and Baweja, S.: Creep and Shrinkage Prediction Model for Analysis and Design of Concrete Structures: Model B3. Am. Concrete Institute, Michigan, 1–83 (2000).
10. Bažant, Z. P.: Prediction of concrete creep and shrinkage: past, present and future. Northwestern, Nuclear Engineering and Design 203, 27-38 (2001).
11. Bažant, Z. P., Cusatis, G. and Cedolin, L.: Temperature Effect on Concrete Creep Modeled by Microprestress-Solidification Theory. J. Eng. Mech. **130** (6), 691-699 (2004).
12. Bažant, Z. P., Yu., Q. and Li, G.: Excessive Long-Time Deflections of Prestressed Box Girders. I: Record-Span Bridge in Palau and Other Paradigms. J. Struct. Eng. **138**, 676-686 (2012).
13. Bažant Z. P., Hubler, M., Wendner, R.: Model B4 for creep, drying shrinkage and autogenous shrinkage of normal and high-strength concretes with multi-decade applicability. TC-242-MDC multi-decade creep and shrinkage of concrete: material model and structural analysis. RILEM Mater Struct. (2014).
14. Bažant, Z. P., Jirasek, M.: Creep and Hygrothermal Effects in Concrete Structures. Sol. Mech. Appl. **225** (2018).
15. Benboudjema, F., Meftab, F. and Torrenti, J. M.: Interaction between drying, shrinkage, creep and cracking phenomenon in concrete, France..Engineering Structures 27, 239-250. (2005).
16. Bernard, O., Ulm, F.-J. and Germaine, J.T.: Volume and deviator creep of calcium-leached cement-based materials. Cem. Concr. Res. **33** (8), 1127–1136 (2003).
17. Brooks, J. J.: 30-year creep and shrinkage of concrete. Mag. Concr. Res. **57** (9), 545-556 (2005).
18. Browne, R. D. and Blundell, R.: The influence of loading age and temperature on the long-term creep behavior of concrete in a sealed, moisture stable state. Mat. Struct. **2** (8), 133-143 (1969).
19. Charpin, L., Pape, Y. L., Coustabeau, E., Masson, B. and Montalvo, J.: EDF Study of 10-years concrete creep under unidirectional and biaxial loading: Evolution of poisson coefficient under sealed and unsealed conditions. Concreep 10, Vienna, Austria (2015).

20. Charpin, L. and Sanahuja, J.: Creep and relaxation poisson's ratio: Back to the foundations of linear viscoelasticity. Application to concrete. Int. J. Sol. Struct. 110-111, 2-14 (2017).
21. Charpin, L., Le Pape, Y., Coustabeau, E., Toppani, E., Heinfling, G., Le Bellego, C., Masson, B., Montalvo, J., Courtois, A., Sanahuja, J. and Reviron, N.: A 12 year EDF study of concrete creep under uniaxial and biaxial loading. Cem. Conc. Res. **103**, 140-159 (2018).
22. Christensen, R.: Theory of Viscoelasticity, Dover (2003).
23. Cruz, C. R.: Elastic properties of concrete at high temperatures. J. PCA R&D Lab. **8**, 37–45 (1966).
24. Drozdov, A.: Viscoelastic Structures - Mechanics of Growth and Aging, Academic Press, (ISBN 0-12-388589-2) (1998).
25. EDF: Vercors an experimental mock-up of a reactor containment building. http://researchers.edf.com/research-activities/generation/vercors-an-experimental-mock-up-of-a-reactor-containment-building-290900.htm (2014).
26. Ehm, C.: Experimental Investigations of the Biaxial Strength and Deformation of Concrete at High Temperatures. Dissertation, Technical University of Braunschweig, Germany. (1985).
27. Gopalakrishnan,K.: Creep of concrete under multiaxial compressive stresses. Univ of Calgary, Canada, PhD thesis. (1968).
28. Gopalakrishnan, K., Neville, A. and Ghali, A.: Creep Poisson's ratio of concrete under multiaxial compression. J. Proc., **66**, 1008-1019 (1969).
29. Grasley, Z. C.: Measuring and Modeling the Time-dependent Response of Cementitious Materials to Internal Stresses. Ph.D, Univ. of Ill. (2006).
30. Grasley, Z. and Lange, D.: The viscoelastic response of cement paste to three-dimensional loading. Mech. Time-Depend. Mater. **11**, 27-46 (2007).
31. Grasley, Z. C., Leung, C. K.: Desiccation shrinkage of cementitious materials as an aging, poroviscoelastic response. Cem. Concr. Res., **41** (1), 77-89 (2011).
32. Hanson, J. A.: A 10-year study of creep properties of concrete. Engineering Laboratories Branch, Design and Construction Division (1953).
33. Hatt, W. K.: A Note on the Effect of Time Element in Loading Reinforced Concrete Beams. Engineering News **58**(17): 438–439 (1907).
34. Hernández, W. P., Castello, D, A., Roitman, N., Magluta, C.: Thermorheologically simple materials: A bayesian framework for model calibration and validation. J. Sound Vib., **402**, 14-30 (2017).
35. Hilton, H.H.: Implications and Constraints of Time-Independent Poisson Ratios in Linear Isotropic and Anisotropic Viscoelasticity. J. Elast. **63,** 221–251 (2001).
36. Jordaan, I. J.: Analysis of creep in concrete structures under general states of stress, seminar on concrete structures subjected to triaxial stresses. Italy, 111-118 (1974).
37. Jordaan, I. and Illston, J.: The creep of sealed concrete under multiaxial compressive stresses. Mag. Concr. Res. **21** (69), 195–204 (1969).

38. Kassem, E., Grasley, Z. and Masad, E.: Viscoelastic poisson's ratio of asphalt mixtures. Int. J. Geomech. **13** (2), 162-169 (2013).
39. Kesler, C. E.: Creep behavior of Portland cement mortar and concrete under biaxial stress. Univ. of Urbana-Champaign (1977).
40. Kim, J. K., Kwon, S.H., Kim, S. Y. and Kim, Y.Y.: Experimental studies on creep of sealed concrete under multiaxial stresses. Mag. Concr. Res. **57** (10), 623-634 (2005).
41. Kommendant, G. J., Polivka, M., and Pirtz, D.: Study of concrete properties for prestressed concrete reactor vessels. Final report UCSESM 76-3 (to General Atomic Company). UC Berkeley (1976).
42. Ladaoui, W., Vidal, T., Sellier, A. and Bourbon, X.: Effect of a temperature change from 20 to 50ºC on the basic creep of HPC and HPFRC. Mater. Struct. **44** (9), 1629-1639 (2011).
43. Lakes, R.S.: The time-dependent Poisson's ratio of viscoelastic materials can increase or decrease. Cell. Polym. **11**, 466–469 (1992).
44. Lakes, R. S. and Wineman, A.: On Poisson's ratio in linearly viscoelastic solids. J. Elast. **85** (1), 45-63 (2006).
45. Ma, Z. and Ravi-Chandar, K.: Confined compression: A stable homogeneous deformation for constitutive characterization. Exp. Mech. **40** (1), 38-45 (2000).
46. Mc Donald, J. E.: Time dependent deformation of concrete under multiaxial stress conditions. In: Technical Report C-75-4 Concrete Laboratory, US Army Engineering Waterways Experiment Station, Vicksburg, MS (1975).
47. McDonald, J. E.: Creep of concrete under various temperature, moisture, and loading conditions. Final report. Reactor vessels, Illinois Univ.Urbana for ORNL (1975).
48. Mindess, S, Young, F. J. and Darwin, D. Concrete. 2nd. ed. Pearson Education, Inc. (2003).
49. Nasser, K. W. and Neville, A. M.: Creep of Concrete at Elevated Temperature. ACI J. Proc. **62** (12), 1567-1579 (1965).
50. Neville, A. M. and Dilger, W.: Creep of Concrete: Plain, Reinforced, Prestressed. North-Holland, Amsterdam (1970).
51. Neville, A. M., Dilger, W. H., and Brooks, J. J.: Creep of plain and structural concrete. Construction Press. (1983).
52. NRC: NUREG/CR–7031- A Compilation of Elevated Temperature Concrete Material Property Data and Information for Use in Assessments of Nuclear Power Plant Reinforced Concrete Structures. Naus, D. J. (2010).
53. Park, S. J. and Roy, K. M.: Simplified bulk experiments and hygrothermal nonlinear viscoelasticity. Mech. Time-Depend. Mater. **8** (4), 303-344 (2004).
54. Parrott, L.: Lateral strains in hardened cement paste under short-and long-term loading. Mag. Concr. Res. **26** (89), 198–202 (1974).
55. Ross, A. D.: Experiments on the creep of concrete under two-dimensional stressing. Mag. Concr. Res. **6** (16), 3-10 (1954).

56. Schwarzl, F. and Staverman, A. J.: Time-Temperature Dependence of Linear Viscoelastic Behavior. J. Appl. Phys. **23** (1952).
57. Sellier, A., Stephane, M., Laurie, B., Vidal, T., Bourbon, X. and Camps, G.: Concrete creep modelling for structural applications: Non-linearity, multi-axiality, temperature and drying effects. France. Cem. Conc. Res. (2016).
58. Torrence, C., Baranikumar, A. and Grasley, Z.: Nuclear concrete microstructure generation and analysis of long-term performance. 19th International Conference on Environmental Degradation of Materials in Nuclear Power Systems – Water Reactors, Boston, August 18-22, American Nuclear Society (2019a).
59. Torrence, C.E., Baranikumar, A. and Grasley, Z.: Homogenization of concrete in nuclear power plants. 25th International Conference on Structural Mechanics in Reactor Technology, Charlotte, August (2019b).
60. Torrenti, J. M. and Le Roy, R.: Analysis and Modelling of Basic Creep. CONCREEP 10, 1400-1409. France (2015).
61. Troxell, G. E., Raphael, J. M. and Davis, R. E.: Long-time creep and shrinkage tests of plain and reinforced concrete. Sixty-first Annual meeting of the Society, June 22-27 (1958).
62. Tschoegl, N. W., Knauss, W.G. and Emri, I.: Poisson's ratio in linear viscoelasticity – a critical review. Mech. Time-Depend. Mater. **7** (6),198-202 (2002).
63. Tulin, L. G. Creep of Portland cement mortar as a function of time. Iowa state university (1965).
64. Vidal, T., Sellier, A., Ladaoui, W., and Bourbon, X.: Effect of temperature on basic creep of High-Performance Concretes heated between 20ºC and 80ºC. J. Mater. Civil Eng. **27** (7) (2015).
65. Wittmann, F.H. and Roelfstra, P.E.: Total deformation of loaded drying concrete. Delft. Cem. Conc. Res., 10, pg. 601-610, (1980).

3 CEMENT MORTAR TO CONCRETE UPSCALING

3.1 Introduction

Concrete is composed of cement paste, fine aggregate, and coarse aggregate. Since cement paste is the only viscoelastic phase, concrete creep occurs entirely due to creep within the cement past. As such, creep data can be captured from cement mortar data, where mortar is the mixture of cement paste and fine aggregates. This allows for concrete to be simplified as a two-phase material of coarse aggregates suspended in a mortar matrix, an approach that has been taken in several previous concrete models (Kim 2011) (Huang, Yan et al. 2016) (Wriggers and Moftah 2006).

In this work, three-dimensional (3D) virtual microstructures are generated, as a review of the literature has indicated that two-dimensional (2D) microstructures do not accurately predict the stiffness (Hbaieb, Wang et al. 2007, Huang, Yan et al. 2016), the stress-strain behavior (Zhou, Song et al. 2017), and changes in the stress field (Shen and Brinson 2007) in simulations of concrete. Concrete in structural applications is subjected to a 3D state of stress and deformation – thus a 2D approach to modeling concrete creep is inapt.

On a similar note, research has shown that the morphology of aggregates influences a variety of physical properties in concrete, including diffusivity (Zheng, An et al. 2012, Dehghanpoor Abyaneh, Wong et al. 2013), fracture patterns (Giaccio and Zerbino 1998, Man 2008), rheology (Cepuritis, Garboczi et al. 2017), and mechanical behavior (Man 2008, Piotrowska, Malecot et al. 2014).

Viscoelasticity in concrete using 3D simulations is not well researched in published scientific literature. A recent study by Bernachy-Barbe and Bary (2019) in 2019 generated a variety of 3D concrete microstructures spheres, Voronoi polygon aggregates, as well as real coarse aggregate shapes extracted from XCT scans. Simulations using the spheres and Voronoi polygons overpredicted creep, while the microstructures with realistic aggregates exhibited creep behavior in good agreement with experimental data. In 2D simulations, Aydin, Arslan et al. (2007) found that the use of irregularly shaped aggregates resulted in a higher resistance to creep than smooth, regular shaped aggregates, confirming the link between simplified aggregate shapes and overprediction of concrete creep.

The objective of this work is to create random 3D concrete microstructures with real, reconstructed aggregate shapes to virtualize long-term concrete creep experiments. Through these virtual experiments, mortar experimental data is upscaled to concrete level data – meaning the homogenized viscoelastic properties of concrete can be obtained significantly faster than traditional concrete laboratory experiments. A microstructure generation code is developed, based on the Anm model (Qian, Garboczi et al. 2014, Thomas, Lu et al. 2015), with the addition of a novel overlap detection algorithm (Torrence 2020). To simulate the viscoelastic behavior of

concrete, finite element analysis is employed to conduct virtual experiments to obtain the creep compliance over time. To validate these virtual experiments, comparison to a concrete creep compliance master curve constructed using the Time-Temperature Superposition (TTS) principle.

3.2 Generation of Random, Realistic Concrete Microstructures

3.2.1 Aggregate Reconstruction

This work utilizes real aggregate shapes that have been reconstructed from micro-X-Ray Computed Tomography (XCT) scans (Garboczi 2002). Specifically, the data from these scans is fit to a spherical harmonics series, defined as

$$Y_n^m(\theta,\phi) = \sqrt{\frac{(2n+1)(n-m)!}{4\pi+m)!}} \cdot P_n^m(\cos(\theta)) \cdot e^{im\phi}, \tag{34}$$

where the term P_n^m represents the associated Legendre functions and *i* is the square root of -1, also called the imaginary number. Spherical harmonics is a mathematical technique that uses associated Legendre functions and cosines to mathematically deform a sphere in a spherical coordinate system. Equation (1) is used to define the radial surface of a particle in a spherical coordinate system by defining the radius, *r*, at every set of angles,

$$r(\theta,\phi) = \sum_{n=0}^{n_{\max}} \sum_{m=-n}^{n} a_{nm} \cdot Y_n^m(\theta,\phi), \tag{35}$$

where θ represents the azimuth angle which ranges from 0 to 2π, and ϕ, refers to the polar angle, ranging from 0 to π. Spherical harmonics accurately represents the morphology of irregular, star-shaped particles by calculating the a_{nm} coefficients at each *n* and *m* pair. Star-shaped particles are defined as those that contain at least one interior point from which a line segment connecting this point to all points on the surface is entirely enclosed within the particle. All aggregates used in this work are star-shaped, an example shown in Figure 33. The origin is considered to be the center of mass in Equation (35). The ideal n_{max} value in Equation (35) is suggested to fall between 18 and 26, as a higher n_{max} value will not result in additional appreciative morphological detail (Garboczi 2002). An example of reconstructed aggregates is given in Figure 33.

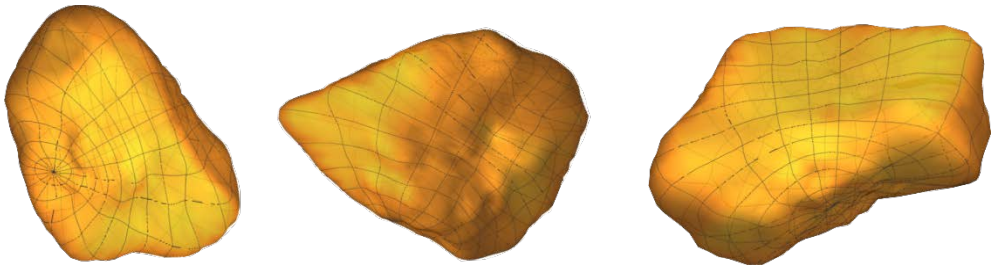

Figure 33. Three aggregates reconstructed from XCT data using spherical harmonics

3.2.2 Random 3D Microstructure Generation

Over 200 coarse limestone aggregates are reconstructed to build a virtual 'stockpile' of aggregates, which can be sieved, sorted, and measured the same way that 'real-life' aggregates are (Garboczi 2002). To generate a random concrete microstructure, these virtual aggregates are randomly placed into a cubic domain. As in real life, two aggregates cannot occupy the same physical space at the same time, so the virtual aggregates are carefully checked for overlap with any previously-placed virtual aggregates.

Periodic boundary conditions are applied when generating the microstructure to prevent wall effects and minimize the size of the representative volume element (RVE). A periodic RVE is the smallest RVE that represents the qualities of a very large, random system like concrete (Sun and Vaidya 1996). In terms of periodicity in the microstructure, an important morphological outcome is that the walls, edges, and corners are all identical to their opposite counterpart. When placing an aggregate into the domain, if it intersects any boundary, it is cut at the boundary and the external piece(s) are translated to the internal face(s) of the opposite boundary. An example of periodicity is given in Figure 34, depicting an aggregate intersecting the wall of the domain.

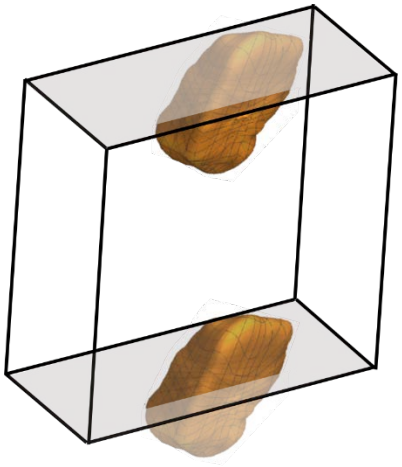

Figure 34. Visualization of an aggregate intersecting the wall of the domain. The 'cut' portions of the aggregate are indicated by translucency.

The microstructure generation code is primarily based on the Anm model, originally published in 2014 (Qian, Garboczi et al. 2014, Thomas, Lu et al. 2015), with adjustments to the aggregate storage and overlap check approaches. The code starts by calculating the volume fraction of aggregates from each sieve size that are needed to reach the total desired volume fraction, based on a user-defined sieve gradation. Next, the code begins by randomly selecting an aggregate from the largest sieve size, where it is then assigned random center coordinates, and rotated about the X-, Y-, and Z- axes, each by a random angle α, β, and γ respectively. This rotation is carried out by the application of three rotation matrices, $R_x(\alpha)$,

$$R_x(\alpha) = \begin{bmatrix} 1 & 0 & 0 \\ 0 & \cos(\alpha) & -\sin(\alpha) \\ 0 & \sin(\alpha) & \cos(\alpha) \end{bmatrix}, \tag{36}$$

$R_y(\beta)$,

$$R_y(\beta) = \begin{bmatrix} \cos(\beta) & 0 & \sin(\beta) \\ 0 & 1 & 0 \\ -\sin(\beta) & 0 & \cos(\beta) \end{bmatrix}, \tag{37}$$

and $R_z(\gamma)$,

$$R_z(\gamma) = \begin{bmatrix} \cos(\gamma) & -\sin(\gamma) & 0 \\ \sin(\gamma) & \cos(\gamma) & 0 \\ 0 & 0 & 1 \end{bmatrix}. \tag{38}$$

Subsequent aggregates are selected from the sieve size dictated by the instantaneous volume fraction of the microstructure and the defined sieve gradation. The aggregate is then temporarily placed into the domain and if the aggregate traverses any of the domain boundaries, it is cut along the boundary and the external portion is translated to the internal face of the opposing boundary. Next, the aggregate is checked for overlap with previously placed aggregates. If an aggregate is periodic, each piece of the aggregate is checked for overlap individually (Bullard and Garboczi 2013). In instances where overlap is detected, the aggregate is rotated by new random angles and assessed for overlap again. This process repeats for up to N_{max} times, at which point the aggregate is translated to a new location in the domain given by randomly selected coordinates (Qian, Garboczi et al. 2014, Thomas, Lu et al. 2015). The variable P_{max} serves as the maximum number of translation attempts per aggregate, a counter used to prevent the code from attempting to place an aggregate in the domain infinite times. N_{max} and P_{max} were selected as five and fifty, respectively, after convergence studies were performed to identify the optimal values.

The overall microstructure generation process is depicted in Figure 35. Detection of overlap is the slowest, most computationally intensive portion of the code, and as a result, much attention was paid to improving the efficiency. The proceeding section provides more detail regarding the overlap check procedure. Once all the aggregates are placed suitably into the domain, the remaining space in the domain is characterized as mortar. An example of a completed microstructure is seen in Figure 36.

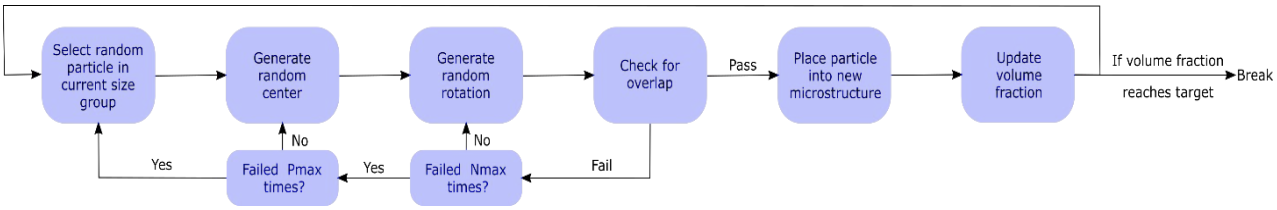

Figure 35. Flowchart of the process used to place aggregates into the domain

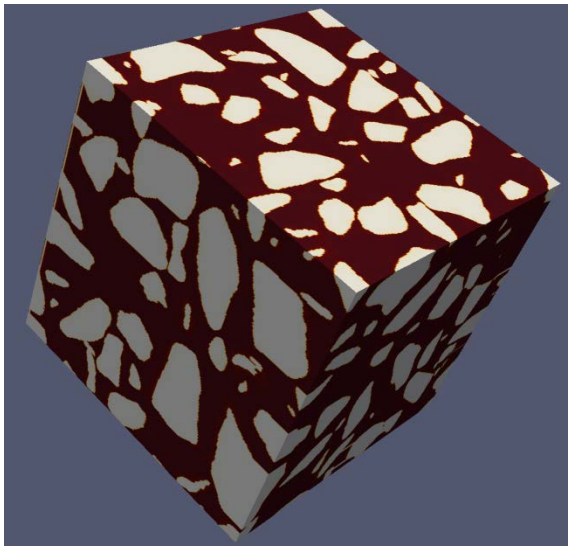

Figure 36. Completed three-dimensional microstructure containing 38% volume coarse aggregate, generated with periodic boundary conditions

The interfacial transition zone (ITZ) between the coarse aggregates and the mortar matrix is very small, on the order of micrometers, relative to the centimeter scale concrete used in this work. The mortar phase includes ITZ around each sand particle, thus it assumed in this work that the influence of the ITZ is captured in the mortar experimental creep data. Furthermore, simulations of concrete creep have suggested that the ITZ has little influence on the rate and magnitude of creep (Bary, Bourcier et al. 2015). Therefore, the authors have chosen to not include the ITZ in this work.

3.2.3 Overlap Check Algorithm

Aggregate-aggregate overlap is prevented in the code through an extensive overlap detection function. This portion of the code is very important because in real life, two aggregates cannot occupy the same physical space at the same time, so this cannot be permitted in the code. Detection of overlap between two virtual particles is an important aspect in a variety of fields, including computer graphics, molecular dynamics, and discrete element method, to name a few.

A novel overlap check was developed in this work to improve the efficiency of overlap detection. This method identifies maxima in the radii function, given in Equation (2), and stores the locations of these maxima a priori for each aggregate. The first spatial derivative of Equation (2) with respect to ϕ is,

$$r_{\phi} = \sum_{n=1}^{n_{\max}} \sum_{m=-n}^{m=n} (im) a_{nm} Y_n^m(\theta, \phi), \tag{39}$$

and the first derivative with respect to θ is,

$$r_{\theta} = \sum_{n=1}^{n=n_{\max}} \sum_{m=n}^{m=-n} \frac{-a_{nm} f_{nm}}{\sin(\theta)} [(n+1)\cos(\theta) P_n^m - (n-m+1) P_{n+1}^m] e^{im\phi}, \tag{40}$$

where f_{nm} is a parameter representing the factorials common to the derivatives with respect to θ, defined as

$$f_{nm} = \sqrt{\frac{(2n+1)(n-m)!}{4\pi(n+m)!}}. \tag{41}$$

The second derivative with respect to ϕ is

$$r_{\phi\phi} = \sum_{n=1}^{n=n_{\max}} \sum_{m=-n}^{m=n} (-m^2) a_{nm} Y_n^m(\theta, \phi) \tag{42}$$

and the second derivative with respect to θ is

$$r_{\theta\theta} = \sum_{n=1}^{n=n_{\max}} \sum_{m=-n}^{m=n} \frac{a_{nm} f_{nm}}{\sin^2(\theta)} \begin{aligned} &[(n+1+(n+1)^2 \cos^2(\theta)) P_n^m \\ &-2\cos(\theta)(n-m+1)(n+2) P_{n+1}^m \\ &+(n-m+1)(n-m+2) P_{n+2}^m] e^{im\phi} \end{aligned}. \tag{43}$$

Asperities on the surface of the aggregates are identified by determining the locations where the first derivatives, Equations (39) and (40), are equal to zero, and the second derivatives, Equations (42) and (43) are negative. This method will identify all asperities on the surface, including minor

surface details and bumps, however the asperities of interest are the most significant maxima in the radii, a smaller n_{max} value, chosen as 10, is used in Equations (39), (40), (42), and (43) in order to neglect the minor asperities. Figure 37 shows asperities identified on aggregates reconstructed with n_{max} values, where the increasing level of fine detail can be seen in the rising n_{max} values. The identified asperities for each aggregate are stored in a text file for retrieval during the overlap check function.

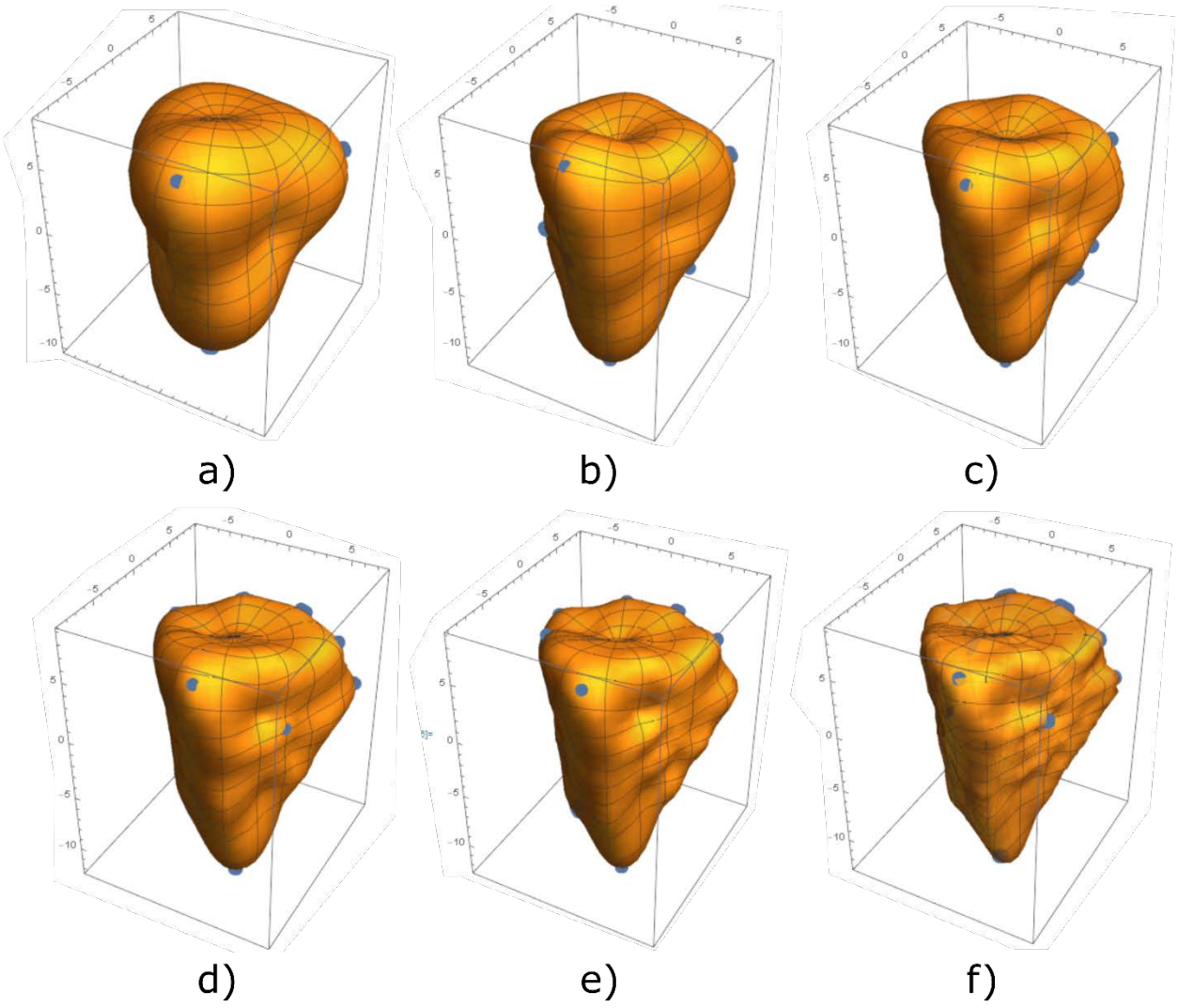

Figure 37. Asperities identified on a particle plotted and analyzed with an n_{max}value of a) 4, b) 6, c) 8, d) 10, e) 12, f) 20. The largest asperities are identified on all, with increasingly subtle asperities detected as n_{max} increases

The overlap check function is divided into three parts. The first part compares the distance between the centroids of a previously-placed aggregate and the aggregate in question. Each aggregate is considered to be enclosed by a bounding sphere with the radius equal to the maximum radius of the aggregate. Additionally, an inscribed sphere is defined as the largest sphere, centered at the center of mass, that is fully contained within the aggregate. If the enclosing spheres do not intersect, there is no possibility that the two aggregate particles can intersect. If these spheres do intersect, the inscribed spheres are compared next. If the inscribed spheres intersect, there is no possibility that the two aggregates *do not* intersect. When this occurs, a flag is raised to bypass rotation of the particle in question and move directly to translating it to a new, random location in the domain. In the case that the inscribed spheres do not overlap, the code moves on to the second filter, where the surface asperities that fall into the lens of potential intersection are assessed. The lens of potential intersection, an example depicted in Figure 38, is the volume shared by two bounding spheres. Only asperities in this lens are assessed for overlap, as this lens represents the only 3D space where the two aggregates have the potential for overlap with one another.

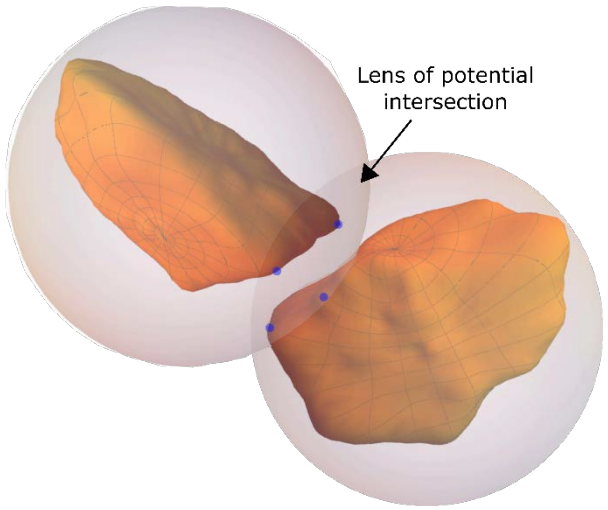

Figure 38. Lens of potential intersection formed by two bounding spheres. Only asperities in this lens are checked, in this example the qualifying asperities are labelled with blue circular markers

Starting with the particle in question, deemed aggregate A, the list of asperities in the lens of potential intersection are assessed for overlap with the previously-placed aggregate, called particle B. For each asperity on aggregate A, a line segment is drawn that connects the center of aggregate B to the asperity on aggregate A. The segment's magnitude is the compared to the radius of aggregate B in the direction of the line segment. If the radius is shorter, as shown on the left of Figure 39, overlap is not detected. On the other hand, if the radius is longer, as on the right of Figure 39, overlap is detected.

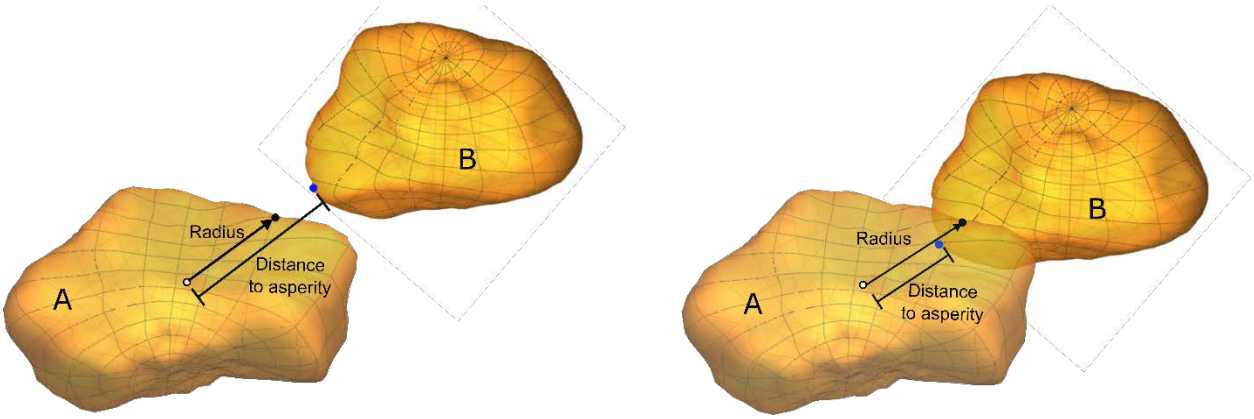

Figure 39 - Diagram of the comparison of the radius of aggregate A to the distance to the asperity on aggregate B. On the left, the radius is shorter, thus no overlap is detected at the asperity, while on the right the radius is longer than the distance to the asperity, leading to the detection of overlap.

Once all the asperities on aggregate A that lie within the lens of potential intersection are checked for overlap, the asperities on aggregate B are then checked using the same method. If no overlap is detected, the code moves on to the third and final filter where a brute force check is performed to determine if any points on aggregate B lie within the point cloud that composes aggregate A and vice versa. This brute force check is the slowest, however it is the most thorough and ensures that any overlap that isn't caught by the first two filters is detected. Asperity-based overlap detection has been shown to be highly effective in reducing the computational time to generate a concrete microstructure, as seen in Figure 40.

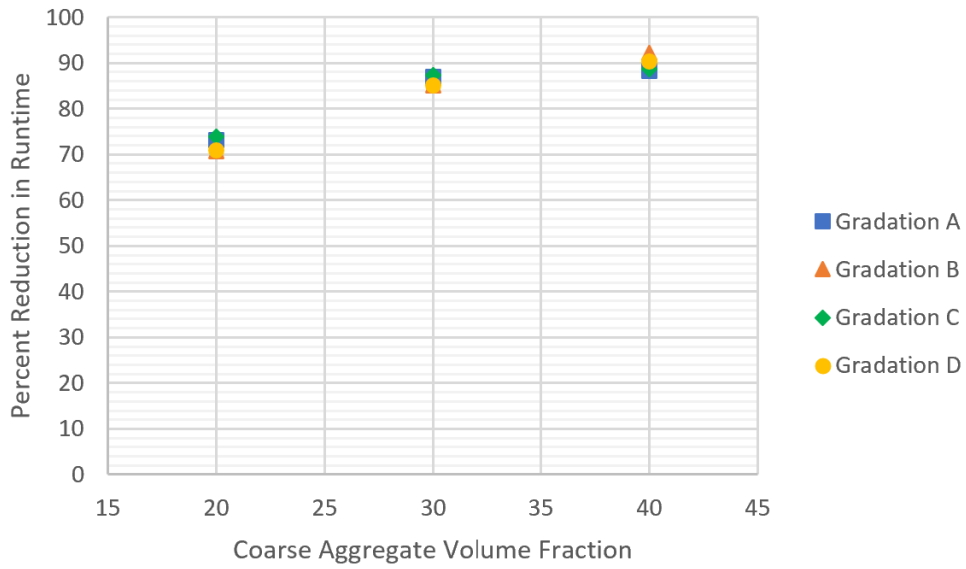

Figure 40 - Decrease in computational time to generate a concrete microstructure resulting from the implementation of the asperity check overlap detection approach

3.3 Finite Element Analysis

3.3.1 Finite Element Mesh Generation

Conversion of the generated microstructure to a finite element mesh is a multi-step process. First, the 3D microstructure is 'sliced' along the Z-direction into a stack of images, where each image represents a thickness of 0.3mm. These images are then imported into OOF3D, a software package developed by the National Institute of Standards and Technology (NIST) (https://www.ctcms.nist.gov/oof/oof3d/). Within OOF3D, a built-in burn algorithm is used to differentiate the matrix and aggregate pixels in each image. This method works very well for composites with a continuous matrix. Next, a uniform finite element mesh is generated, followed by refinement of the mesh to bring nodes to aggregate surfaces and subdivide heterogeneous elements to better represent the aggregate shape. A meshed microstructure using tetrahedral elements is shown in Figure 41.

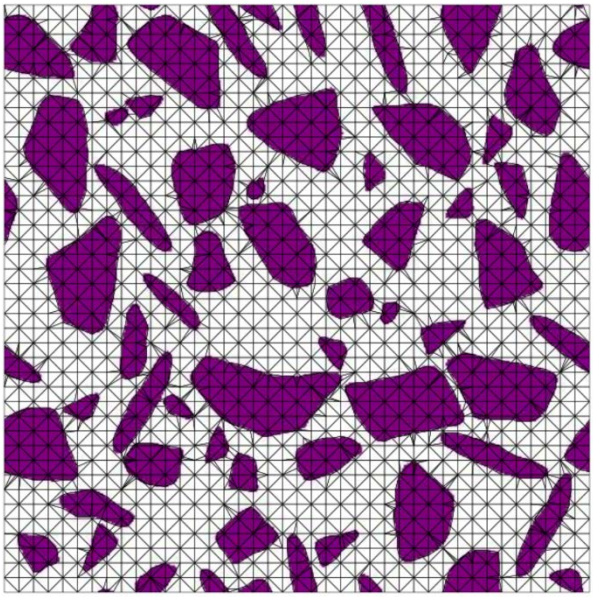

Figure 41. Top-down view of a single plane of a meshed microstructure

3.3.2 Material Behavior Parameters

In this work, the software Abaqus is utilized as the finite element solver. The coarse aggregates are assumed to be linear elastic with a Young's modulus of 36 GPa and a Poisson's ratio of 0.22 (Al-Shayea 2004). A Young's modulus of 25.5 GPa and a Poisson's ratio of 0.15 are assigned to the mortar phase. The viscoelastic behavior of the mortar is described by the data collected from laboratory mortar creep experiments. The creep compliance, $J(t)$, was calculated from the experimental mortar data (Baranikumar et al., 2020), provided in Equation (44) where t represents the number of days under loading.

$$J(t) = 1.86 \cdot 10^{-3} \cdot Log[1+t] + -5.19 \cdot 10^{-10} \cdot Log[1+\frac{t}{10}] + 3.85 \cdot 10^{-2} \cdot Log[1+\frac{t}{100}] + 8.55 \cdot 10^{-3} \cdot Log[1+\frac{t}{1000}] + 2.59 \cdot 10^{-9} \cdot Log[1+\frac{t}{100000}] \frac{1}{GPa} \quad (44)$$

It should be noted that only basic creep is represented in Equation (44) and the subsequent simulations. Because the Poisson's ratio of the mortar is nearly constant, the conversion between the bulk, $B(t)$, and shear, $L(t)$, compliance functions can be calculated from $J(t)$ directly using the relationships given by

$$B(t) = \frac{J(t)}{3 \cdot (1-2 \cdot v)}, \quad (45)$$

and

$$L(t) = \frac{J(t)}{2 \cdot (1+v)}. \quad (46)$$

If the Poisson's ratio was not constant, the relationships in Equation (45) and (46) would hold only in the Laplace domain. The bulk and shear compliance data were then normalized by their values at t = 0 and given as input to Abaqus, where a Prony series is calculated to define the dimensionless relaxation modulus. A virtual stress relaxation experiment is simulated in Abaqus by applying a constant uniaxial compressive strain of 0.02% in the X-direction for 17,000 days. A stress relaxation experiment is selected instead of a virtual creep experiment due to the relative ease of applying a constant strain boundary condition to the surface nodes in Abaqus. Moreover, the creep compliance, $J(t)$, and relaxation modulus, $E(t)$,can be easily interchanged in the Laplace domain through the inverse relationship,

$$\bar{J}(s) = \frac{1}{\bar{E}(s) \cdot s^2}, \quad (47)$$

where $\bar{J}(s)$ is the Laplace transformed creep compliance and $\bar{E}(s)$ is the Laplace transformed relaxation modulus.

3.3.3 Application of Periodic Boundary Conditions

In addition to being a morphological feature of the generated microstructures, periodic boundary conditions also serve mathematical roles. Periodicity in the stress and strain fields is defined as displaying continuity between opposite boundaries. This is imposed in Abaqus by pairing nodes on the surface with their most closely aligned counterpart on the opposite surface. For example, nodes on the ±X-Y walls of the microstructure are paired together. These node pairings are used to write constraint equations into the Abaqus input file to constrain the displacement, *u*, in each direction to be continuous between the two nodes, *a* and *b*, through the equations

$$\begin{aligned} u_x^a + u_x^b &= 0 \\ u_y^a + u_y^b &= 0 \\ u_z^a + u_z^b &= 0. \end{aligned} \tag{48}$$

To ensure that periodic boundary conditions are properly applied and are effective, the stress and strain along the edges of the positive X-Z face were analyzed. This line spanned the entire width of the face. As seen in Figure 42, the value of the strain along the top and bottom edges, defined as the edges of the X-Z plane parallel to the Z-axis, align well with one another indicating periodicity in the strain field. The small differences between the strain on the top and bottom edges can be attributed to differences in the finite element mesh along the two edges. OOF3D, the software used to generate the finite element mesh does not currently include the capability to create a periodic mesh, therefore while the microstructure is perfectly periodic, the mesh is not.

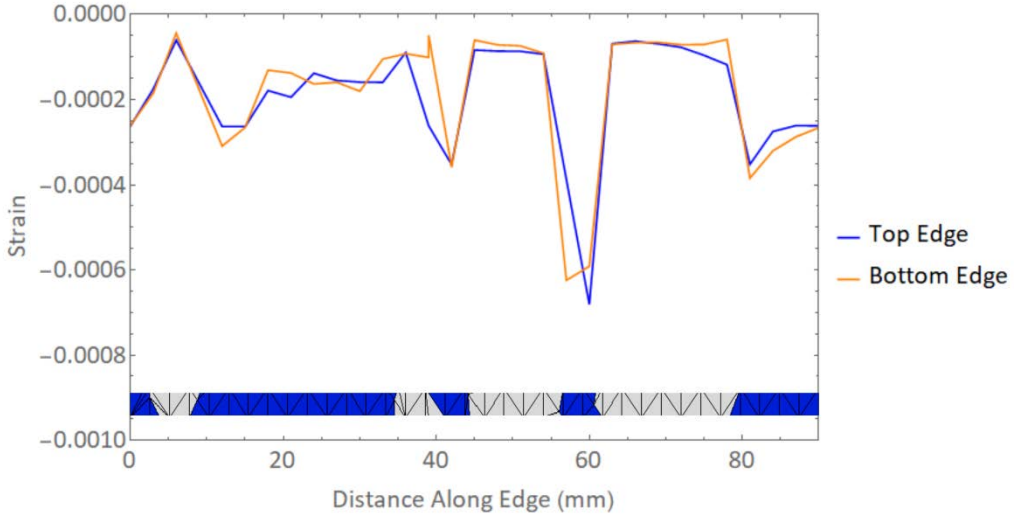

Figure 42. The XX component of the strain tensor at time = 7084 days along a line parallel to the Z-axis on the X-Z face of the cubic microstructure. For references, the composition of the edge of the microstructure is overlaid below the data, where mortar is identified in blue and the aggregates in gray. Small differences in the curves are due to differences in the finite element mesh between the two edges.

The stress field was also analyzed along the two edges line, first at the instantaneous moment of loading, followed by 7,000 days of relaxation time. Stress along the top and bottom edges can be seen in Figure 43, indicating that the application of periodic boundary conditions, through both the generation of the virtual microstructure as well as the mathematical constraints placed on pair nodes, is successful in imposing periodicity in the stress and strain fields.

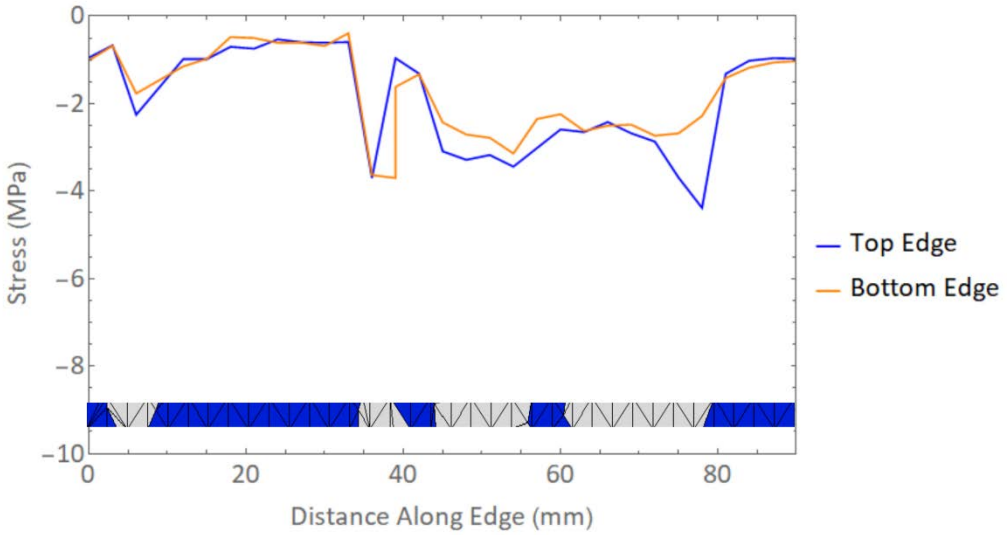

Figure 43. The XX component of the stress tensor at time = 7,084 days along a line parallel to the Z-axis on the X-Z face of the cubic microstructure. The composition of the edge of the microstructure is overlaid below the data, where mortar is identified in blue and the aggregates in gray. Small differences in the curves are due to differences in the finite element mesh between the two edges.

3.3.4 Data Analysis

The raw stress and strain data from the finite element simulations are used to calculate the stress relaxation and creep compliance functions. The uniaxial relaxation modulus is presumed to be of the form

$$E(t) = E_0 + E_1 \cdot e^{-\frac{t}{\tau_1}} + E_2 \cdot e^{-\frac{t}{\tau_2}} + E_3 \cdot e^{-\frac{t}{\tau_3}} + E_4 \cdot e^{-\frac{t}{\tau_4}} + E_5 \cdot e^{-\frac{t}{\tau_5}} + E_6 \cdot e^{-\frac{t}{\tau_6}} \text{ GPa}, \quad (49)$$

where the parameters E_0, E_1, E_2, E_3, E_4, E_5, and E_6, are coefficients with units of GPa and τ_1, τ_2, τ_3, τ_4, τ_5, and τ_6 are relaxation times in days. In this research, τ_1, τ_2, τ_3, τ_4, τ_5, and τ_6 are selected as 1, 10, 100, 1,000, 10,000, and 100,000 days, respectively. Equation (50) is then integrated to determine $\sigma(t)$ where the constitutive relationship between stress, strain, and relaxation modulus over time is defined as

$$\sigma(t) = \int_0^t E(t-t') \frac{\delta\varepsilon(t')}{\delta t'} dt, \quad (50)$$

where ε(t) is known from the Abaqus output data. This results in the $\sigma(t)$ function taking the form of a polynomial with the E_0, E_1, E_2, E_3, E_4, E_5, and E_6 coefficients still present. The $\sigma(t)$ function is then fit to the ε(t) data to determine the E_1, E_2, E_3, E_4, E_5, and E_6 coefficients.

3.3.5 Convergence Studies

To minimize the computational expense of the stress relaxation simulations, it is of interest to perform these simulations on the optimal microstructure RVE size and finite element mesh density. Two convergence studies were performed to identify these values.

Finite Element Mesh Density

A convergence study was performed as part of this research to identify the optimal density of finite elements, defined as the lowest density of elements that provides simulation results consistent with the results of simulations of higher mesh densities. To locate this value, a single microstructure was meshed multiple times with an increasingly mesh density. Each mesh was then used to run identical relaxation simulations with periodic boundary conditions. The output data was then assessed to compute the relaxation modulus, which was compared at four time points to determine at which the mesh density value the results begin to converge to a relatively constant value. As seen in Figure 44, the resulting plots indicate that convergence can be seen beyond a mesh density value of about 0.6 elements/mm^3. Meshes with a density above 0.8 elements/mm^3 were of have poor mesh quality and were therefore excluded from this work.

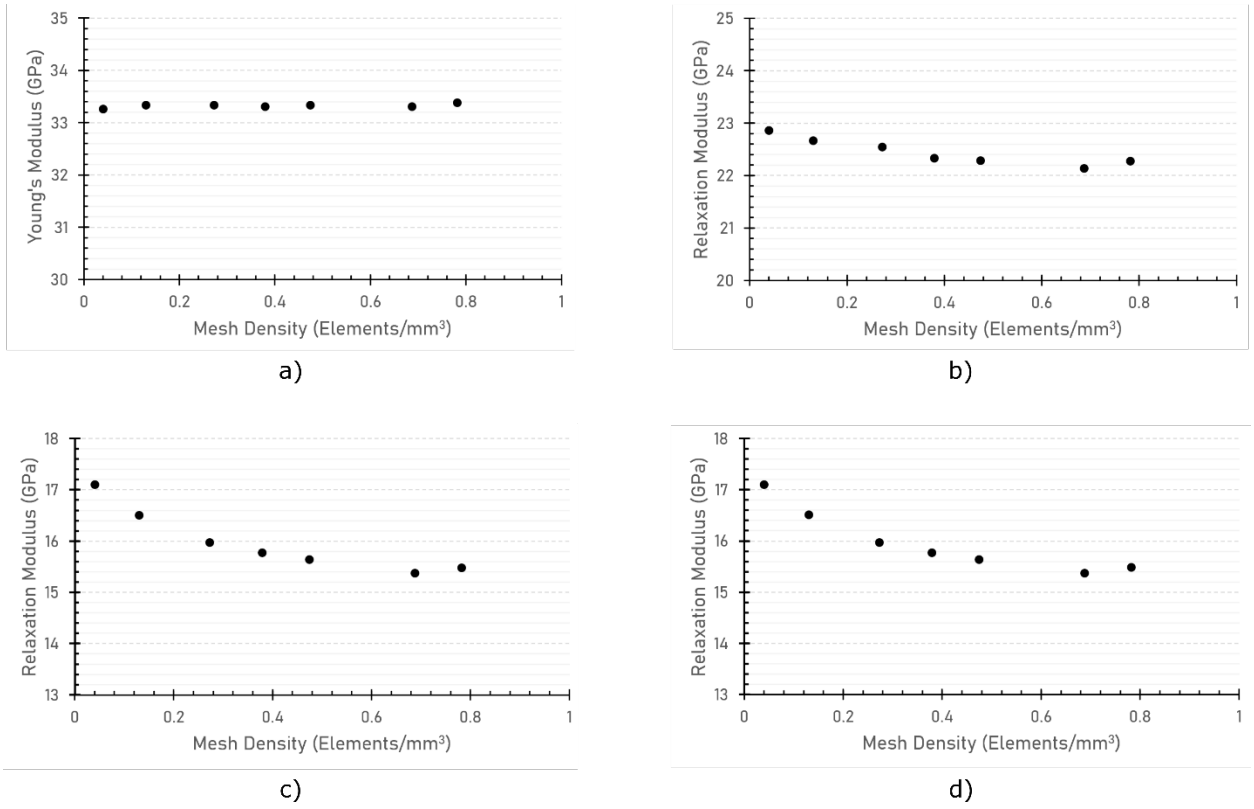

Figure 44. Young's modulus (a) and the relaxation modulus at 100 days (b), 1,000 days(c), and 5,000 days (d) plotted against the finite element mesh density to determine convergence using a 75mm cubic microstructure with 38% coarse aggregate volume fraction

RVE Size Convergence Study

Large microstructures take lengthier time to generate, and as a larger microstructure will require more finite elements to maintain the optimal density, it is computationally more expensive to simulate larger microstructures. The optimal RVE size is established by generating microstructures across a range of sizes, followed by comparing the simulated relaxation modulus at four time points – the same manner used to determine the optimal finite element mesh density. As seen in Figure 45, convergence can be seen occur at an edge length of 90 mm.

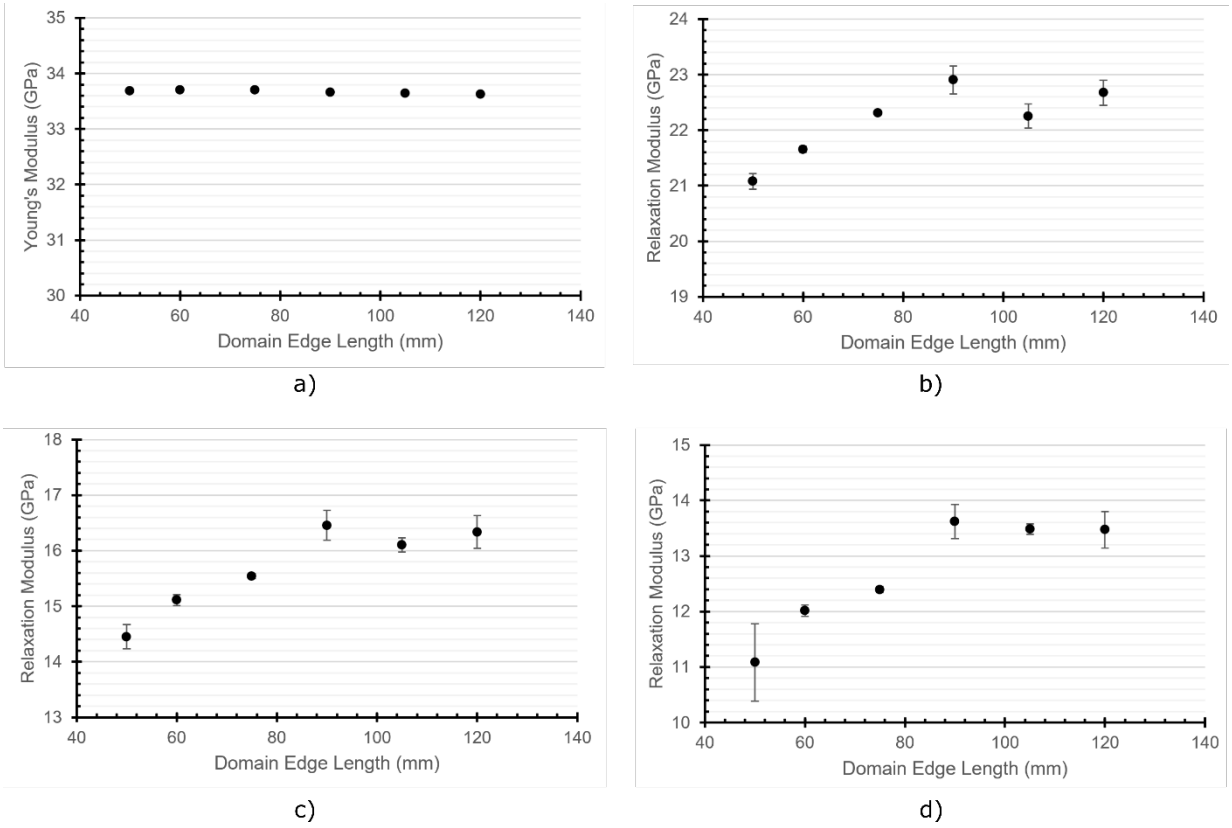

Figure 45. Young's modulus (a) and the relaxation modulus at 100 days (b), 1,000 days(c), and 5,000 days (d) plotted against the domain edge length of the microstructure to determine convergence of 38% coarse aggregate volume fraction microstructure size meshed with a density of approximately 0.6 elements/mm^3

3.4 Results and Discussion

With confidence in the application of periodic boundary conditions and optimal RVE and finite element mesh density values, comparison to 800 days experimental concrete creep data was performed. Five cubic microstructures with an edge length of 90 mm were generated and subjected to a stress relaxation simulation in Abaqus. The average creep compliance results are shown in

Figure 47, where the error bars on the experimental data points represent the standard error, defined by

$$\text{Standard Error} = \frac{\text{Standard Deviation}}{\sqrt{\text{Number of Samples}}}. \quad (51)$$

Data from both the internal strain gauges and the DEMEC strain gauges are shown in Figure 46. While some surface drying was measured, the external (DEMEC) strain gauge data represents only the basic creep, as Bazant and Baweja's Model B3 was used to subtract off the drying creep (Bazant and Baweja 2000). As shown in Figure 46, the creep compliance predicted by the 3D simulations falls within the experimental data bounds over the entire 800 day period.

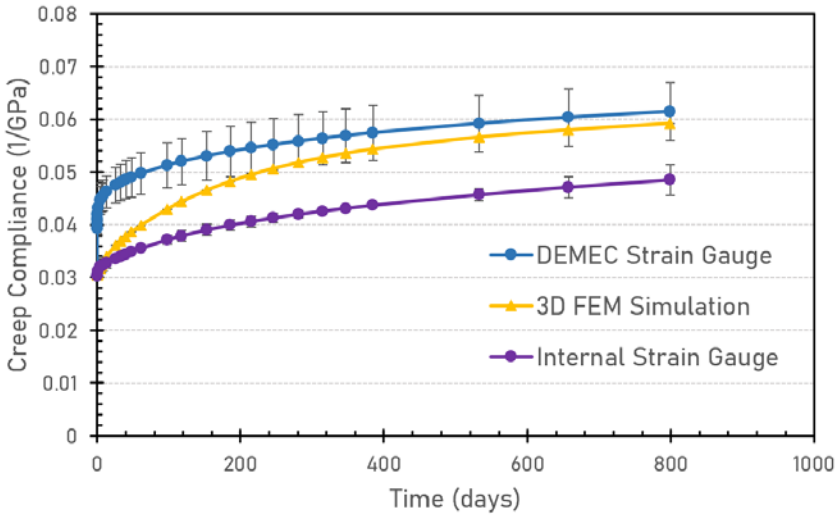

Figure 46. Comparison of 800 days of experimental creep data to FEM creep simulation results

Moving forward, simulations of 17,000 days, or 27 years, of concrete creep were performed using five 3D cubic microstructures with an edge length of 90 mm. The TTS principle was used to build a creep compliance master curve using the external surface strain data collected from the DEMEC strain gauges at 20° C and 60° C. The shift factor for the 60° C data was 12.5, resulting in a master curve for creep at 20° C that extends 800 days of data to 10,000 days, or 27 years. Figure 47 displays the master curve, in black, plotted with the average of five simulations, where excellent agreement is seen between the simulated and experimental concrete viscoelastic behavior over two and a half decades. The numerical difference between the curves at 10,000 days is 3%, indicating that the assumptions to treat the aggregates as linear elastic and neglect the ITZ did not impact the accuracy of the 3D concrete creep compliance simulations. This aligns with the findings of Bary, Bourcier et al. (2015), which suggested the ITZ plays only a minor role in the creep of concrete at this scale.

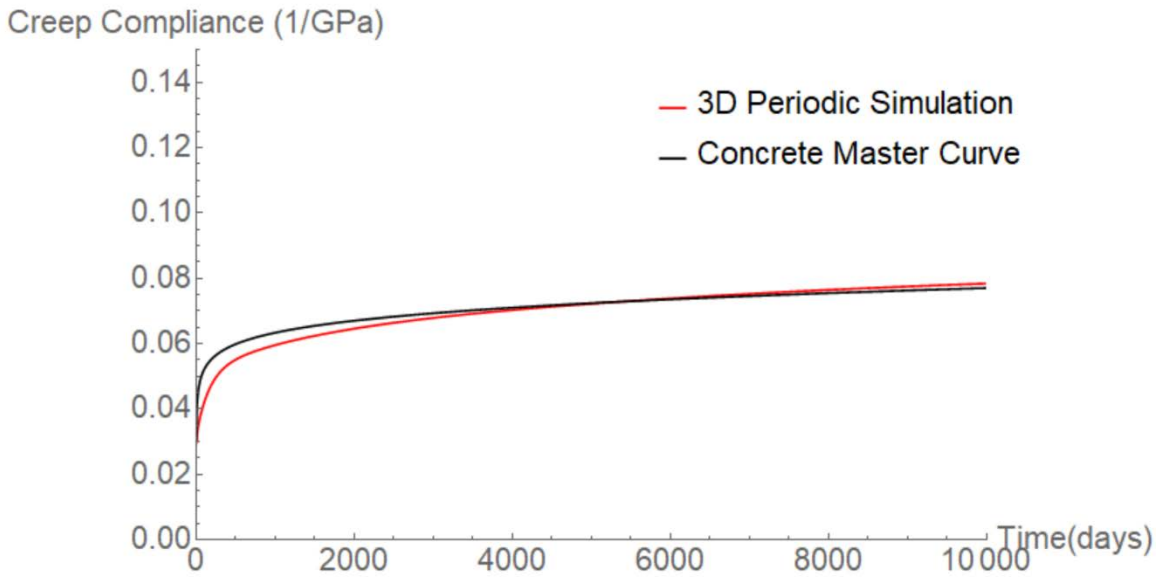

Figure 47. Experimental concrete creep compliance data plotted with simulated concrete creep compliance out to 27 years

The concrete master curve is valid to 10,000 days, however the mortar master curve is valid to over 17,000 days (46.5 years). As the finite element simulations are run with the mortar master curve data, the simulations can be run up to 17,000 days with valid mortar data. Figure 48 shows the predicted creep compliance in the concrete finite element simulations up to 17,000 days. Although comparison to the concrete master curve cannot be performed beyond 10,000 days without extrapolation of the master curve, the simulation results show good agreement with the master curve up until that point.

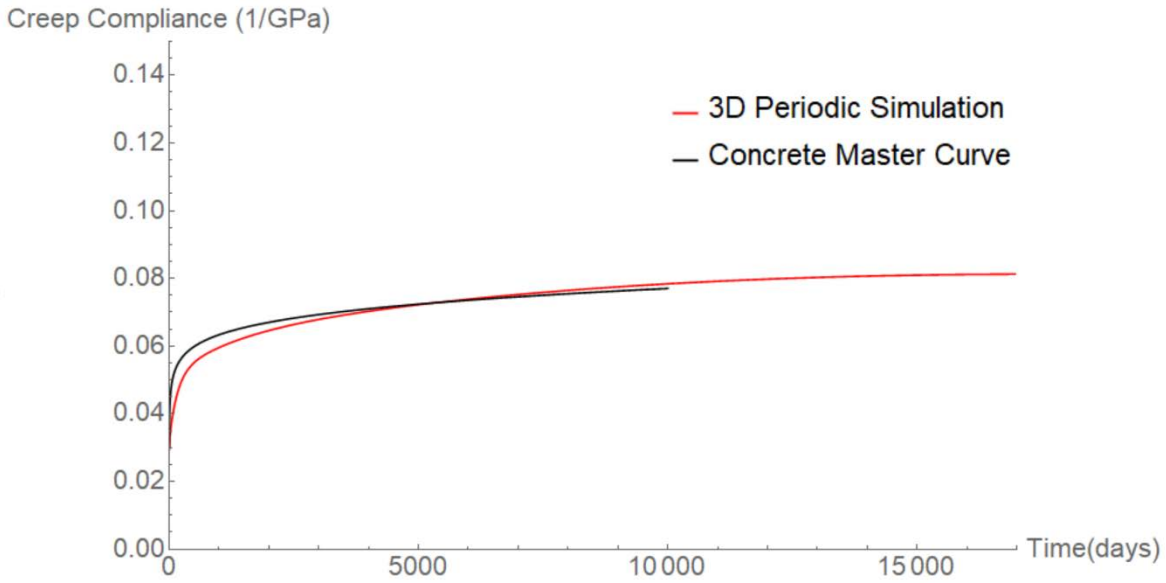

Figure 48. Concrete creep compliance simulated to 17,000 days, compared to 10,000 days of experimental concrete creep data extended using the TTS principle

3.5 Conclusions

In this work, a computational framework to generate random, 3D concrete microstructures from reconstructed coarse limestone aggregates has been developed. These codes are flexible, able to account for a variety of aggregate size gradations aggregate morphologies, and volume fractions. Finite element analysis performed on these virtual microstructures highlights the primary usefulness of this work – the ability to quickly upscale mortar viscoelastic behavior to long-term concrete creep/relaxation data. A master creep compliance curve, constructed from the TTS principle, spanning 20 years was used to validate two decades of simulated concrete creep. The following conclusions can be drawn from this work:

- Periodic boundary conditions are successfully applied to both the microstructure generation and the numerical constraints in the finite element analysis. The stress and strain along opposite edge elements in 3D microstructures were compared and found to have good, but not perfect, agreement, indicating true periodicity, with small differences resulting from the differences in non-periodic mesh between the opposite edges.

- Convergence of the finite element mesh density was determined to be approximately 0.6 elements/mm^3 for the microstructures. Simulations performed with lower mesh densities showed up to 20 % difference from the converged results, displaying the importance of using a suitable finite element mesh.

- Convergence of the RVE size was found to be at approximately 90 mm, equivalent to an edge length approximately 3x longer than the largest aggregate's length.

- The assumptions to treat aggregates as linear elastic and the choice to disregard the ITZ in this research appear to be valid simplifications given the close agreement between the 3D simulation results and experimental data.

- Due to the time-dependent nature of concrete creep, it is challenging to collect creep behavior data in a timely fashion. This approach has successfully upscaled experimental mortar creep data, which is significantly easier to test than concrete, using the TTS principle.

Acknowledgements

Edward J. Garboczi performed the XCT scans and data analysis to determine the a_{nm} coefficients that were used in this work to reconstruct real aggregate shapes. Portions of this research were conducted with high performance research computing resources provided by Texas A&M University (https://hprc.tamu.edu).

References

1. Al-Shayea, N. A. (2004). "Effects of testing methods and conditions on the elastic properties of limestone rock." Engineering Geology **74**(1): 139 - 156.
2. Aydin, A. C., A. Arslan and R. Gl (2007). "Mesoscale simulation of cement based materials' time-dependent behavior." Computational Materials Science.
3. Bary, B., C. Bourcier and T. Helfer (2015). Numerical analysis of concrete creep on mesoscopic 3D specimens.
4. Bazant, Z. P. and L. Panula (1978). Practical prediction of time-dependent deformations of concrete. **12:** 169--174.
5. Bernachy-Barbe, F. and B. Bary (2019). "Effect of aggregate shapes on local fields in 3D mesoscale simulations of the concrete creep behavior." Finite Elements in Analysis and Design **156**(September 2018): 13--23.
6. Bullard, J. W. and E. J. Garboczi (2013). "Defining shape measures for 3D star-shaped particles: Sphericity, roundness, and dimensions." Powder Technology **249**: 241--252.
7. Cepuritis, R., E. J. Garboczi, C. F. Ferraris, S. Jacobsen and B. E. Srensen (2017). "Measurement of particle size distribution and specific surface area for crushed concrete aggregate fines." Advanced Powder Technology **28**(3): 706--720.
8. Dehghanpoor Abyaneh, S., H. S. Wong and N. R. Buenfeld (2013). "Modelling the diffusivity of mortar and concrete using a three-dimensional mesostructure with several aggregate shapes." Computational Materials Science.
9. Garboczi, E. J. (2002). "Three-dimensional mathematical analysis of particle shape using X-ray tomography and spherical harmonics: Application to aggregates used in concrete." Cement and Concrete Research **32**(10): 1621--1638.
10. Giaccio, G. and R. Zerbino (1998). "Failure mechanism of concrete: combined effects of coarse aggregates and strength level." Advanced Cement Based Materials.
11. Graves, H., Y. Le Pape, D. Naus, J. Rashid, V. Saouma, A. Sheikh and J. Wall (2014). Expanded Materials Degradation Assessment (EMDA): Aging of Concrete and Civil Structures (NUREG/CR-7153), Nuclear Regulatory Commission. **4**.

12. Hbaieb, K., Q. X. Wang, Y. H. J. Chia and B. Cotterell (2007). "Modelling stiffness of polymer/clay nanocomposites." Polymer.
13. Huang, Y., D. Yan, Z. Yang and G. Liu (2016). "2D and 3D homogenization and fracture analysis of concrete based on in-situ X-ray Computed Tomography images and Monte Carlo simulations." Engineering Fracture Mechanics **163**: 37--54.
14. Jordaan, I. J. (1974). "A note on concrete creep analysis under static temperature fields." Mat \' e riaux et Constructions **7**(5): 329--333.
15. Kim, S. M. a. (2011). "Meso-scale computational modeling of the plastic-damage response of cementitious composites." Cement and Concrete Research **41**(3): 339--358.
16. Man, H.-K. a. (2008). "Size effect on strength and fracture energy for numerical concrete with realistic aggregate shapes." **154**: 61--72.
17. Piotrowska, E., Y. Malecot and Y. Ke (2014). "Experimental investigation of the effect of coarse aggregate shape and composition on concrete triaxial behavior." Mechanics of Materials.
18. Qian, Z., E. J. Garboczi, G. Ye and E. Schlangen (2014). "Anm: a geometrical model for the composite structure of mortar and concrete using real-shape particles." Materials and Structures/Materiaux et Constructions **49**(1-2): 149--158.
19. Scheiner, S., C. Hellmich and A. M. Asce (2009). "Continuum Microviscoelasticity Model for Aging Basic Creep of Early-Age Concrete." Journal of Engineering Mechanics.
20. Shen, H. and L. C. Brinson (2007). "Finite element modeling of porous titanium." International Journal of Solids and Structures.
21. Sun, C. T. and R. S. Vaidya (1996). "Prediction of composite properties from a representative volume element." Composites Science and Technology **56**(2): 171--179.
22. Thomas, S., Y. Lu and E. J. Garboczi (2015). "Improved Model for Three-Dimensional Virtual Concrete: Anm Model." Journal of Computing in Civil Engineering **30**(2): 04015027.
23. Torrence, C., E.: Generation of Virtual 3D Microstructures Applied to Modeling Creep and Relaxation. Ph.D. Dissertation, Texas A&M University, College Station, TX (2020).
24. Tulin, L. G. (1965). Creep of a Portland cement mortar as a function of stress-level and time. PhD, Iowa State University.
25. Wriggers, P. and S. O. Moftah (2006). "Mesoscale models for concrete: Homogenisation and damage behaviour." Finite Elements in Analysis and Design **42**(7 SPEC. ISS.): 623--636.
26. Zheng, J., X. An and M. Huang (2012). "GPU-based parallel algorithm for particle contact detection and its application in self-compacting concrete flow simulations." Computers and Structures **112-113**: 193--204.
27. Zhou, R., Z. Song and Y. Lu (2017). "3D mesoscale finite element modelling of concrete." Computers and Structures **192**: 96--113.

4 LARGE-SCALE STRUCTURAL CONCRETE CREEP EXPERIMENT

4.1 Introduction

In this study, concrete creep was evaluated on large scale specimen testing, accompanied by complementary small-scale materials testing. Three concrete wall specimens, containing instrumentation to measure concrete strain, temperature, and strains in post-tensioning bars, was constructed with varying wall reinforcement ratios, thicknesses, and post-tensioning load to model the effects of creep.

4.2 Factors Contributing to Creep

To fully define the scope of the project, it is necessary to identify the factors that affect creep. Some of the factors that influence creep are humidity, external temperature, concrete mix design parameters, and curing method. Other contributing factors that was focused on this study are the level of concrete prestress, environmental conditions, wall thickness, wall reinforcement ratio, and the combined effects of creep and stress redistribution.

4.2.1 Level of Stress

The level of applied stress on the concrete is a factor that contributes to the basic creep mechanism. If the level of stress is high with respect to the concrete compressive strength f'_c, then a non-linear creep curve is assumed, whereas low levels of concrete stress, including typical service stresses, are assumed to follow a linear creep model (Bazant 1988). ACI 318-14 limits the compressive stress at service loads of prestressed concrete to 0.45f'c to prevent excessive creep deformations (American Concrete Institute 2014). Above this limit, the creep behavior is presumed to be non-linear.

4.2.2 Environmental Conditions

Environmental conditions typically influence the drying creep mechanism due to the varying external humidity, precipitation, and temperature. Since drying creep depends on the relative humidity of the concrete, the humidity of the environment, precipitation, and temperature fluctuations, differential creep can develop through the thickness of a specimen resulting in a stress gradient from the surface of the specimen that is directly in contact with the environment to the inside of the specimen. Another important environmental condition is the temperature of the specimen when the specimen is loaded. If the temperature during loading is relatively high, then there can be more creep induced by the load (Marques and Barbosa 2013).

4.2.3 Reinforcement Ratio

The longitudinal and transverse reinforcement ratios of a concrete specimen are important parameters in studying creep because of the ability of the steel to carry compressive loading and to potentially confine the concrete, resulting in enhanced triaxial stress-strain behavior. As concrete creeps over time, the reinforcing steel within the concrete can be forced to carry additional loading due to the redistribution of forces, which could potentially yield the steel. In addition, as the concrete can be confined by both longitudinal and transverse reinforcement, there can be less air voids inside the concrete where moisture would migrate, leading to less creep strain and less shrinkage (Lin et al. 2014).

4.2.4 Redistribution of Stress

For repair and maintenance purposes of nuclear containment concrete walls, it is important to identify the combined effects of concrete creep and stress redistribution. In post-tensioned nuclear containment walls, post-tensioning strands must undergo maintenance and repairs to keep the facility safe and operable, therefore there may be a need to retighten or even cut tendons periodically. Cutting tendons leads to instantaneous stress redistribution through the structure, adding more load to the other strands as well as the concrete in the surrounding area. Creep on its own leads to stress redistribution between the concrete, reinforcing steel, and post-tensioning strands, which can overstress the structure when a post-tensioning tendon is cut, potentially causing failure (Stefanou 1981). Long term concrete creep is the leading cause of prestress losses in a structure as well (Song et al. 2002), therefore it is important to have a method of tightening tendons periodically over time, if necessary, to keep the structure safe and operable.

4.3 Research Objectives

The purpose of this research is to determine how creep influences the long-term life span of nuclear containment structures by determining the creep induced strain in the concrete and the loss of post-tensioning force as a result of creep in the concrete. Different design parameters were adjusted for each specimen to determine how the structural detailing can directly influence creep propagation as well, including varying vertical and circumferential reinforcement ratios and wall thicknesses. Sensors was carefully selected and tested to ensure compatibility with the environmental conditions and strain demands of the specimens. A sustainable data acquisition system (DAQ) was developed to capture data associated with strains and temperatures in the concrete and strains in the post-tensioning bars, ensuring long-term monitoring capabilities. Three concrete wall specimens were constructed, each with different wall thicknesses, levels of reinforcement, and applied post-tensioning steel forces, to analyze the influence of varying structural parameters on concrete creep propagation. Each specimen was equipped with full bridge concrete strain gages and thermocouples at varying depths in three directions to measure concrete strain and temperature over time.

Specimens 1 and 2 contains steel reinforcement and was stressed with unbonded post-tensioning steel bars equipped with strain gages to measure the strains in the post-tensioning steel bars over time. Specimen 3 acts as a control specimen, containing only concrete with no reinforcement and no applied post-tensioning forces. Given the large diameter of typical prototype containment vessels, the actual wall stresses in such curved sections are similar to that in straight walls, exhibiting a biaxial state of stress. Thus, for experimental ease, the specimens for this study were designed and constructed as straight wall segments.

4.4 Specimen Design and Construction

4.4.1 Design of Large Scale Specimens

In order to model the long-term behavior of concrete creep in the walls of nuclear containment facilities, three large-scale straight wall concrete specimens were designed and constructed. It is worth noting that the middle 91 cm by 91 cm (3 ft by 3 ft) of each specimen was the focus of the data collection and design decisions. In order to ensure structural stability and resistance to overstress around the edges of each specimen as a result of post-tensioning forces, the outside perimeters of the two loaded specimens had doubly reinforced longitudinal steel and confined transverse steel. The middle 91 cm by 91 cm (3 ft by 3 ft) of each specimen, consisting of 2 wall face mesh layers of steel near the wall cover, were constructed to represent the conditions designed for this study.

The design of Specimen 1 (Figure 49 - Figure 54) was based on Sandia's 1:4 experimental specimen (Hessheimer et al. 2003). The prototype used in Sandia's study was based on an actual nuclear power plant in Japan called Ohi-3. Sandia constructed a thin-walled cylindrical concrete structure with a dome top and an internal steel liner. The prototype was stressed with unbonded post-tensioning steel cables running both vertically and circumferentially through the structure. The wall thickness of Sandia's model was about 33 cm (13 in), which was the thickness used in Specimen 1 of this research. The height of the Sandia model (excluding the dome top) was approximately 10.8 m (35.3 ft) tall. However, due to cost, construction, and materials transportation limitations, a height and width of 2.4 m (8 ft) were adopted in the design of Specimen 1. Based on strut and tie theory, which assumes stress propagation at 45º from the loading point, it was determined that the height and width of Specimen 1 was sufficient to create a similar biaxial state of stress in portions of the full Sandia model. An additional 30 cm (1 ft) clearance at the bottom of Specimen 1 was required to provide space for the post-tensioning steel bars, so a 2.4 m by 2.4 m (8 ft by 8 ft) wall was designed with 30 cm by 46 cm (1 ft by 1.5 ft) feet on both sides, resulting in a 2.7 m (9 ft) wall height.

The reinforcement ratio of the Sandia model was 6 to 10 times larger than the minimum reinforcement ratio according to ACI 318-14, Chapter 11 (American Concrete Institute 2014). First, the two perimeter vertical cages of Specimen 1 were assembled, composed of 2 rows of 3 #6 longitudinal bars running vertically, spaced at about 16.5 cm (6.5 in). The vertical #6 bars were

tied transversely by #4 closed hoops, spaced at about 11 cm (4.5 in) from the top and mid-height of the specimen and about 10 cm (4 in) near the feet of the specimen. Next, the upper and lower horizontal perimeter cages were assembled, which consisted of 2 rows of 3 #7 longitudinal bars spaced at about 10 cm (3.8 in) and tied transversely by #4 closed hoops spaced at about 15 cm (6 in). The horizontal cages bent inwards to tie into the vertical cages. Next, the two layers of wall face mesh steel were connected to the horizontal and vertical perimeter cages, composed of alternating #5 and #6 vertical bars spaced at about 15 cm (6 in), and tied directly to the horizontal #7 bars spaced at about 11 cm (4.4 in). Finally, the radial ties were installed through the wall thickness, providing a connection between the two mats of steel on both faces of the wall. Due to very tight spacing and constructing the walls flat on the ground, some of the radial ties were left out of the assembly in non-critical locations. However, the center 91 cm by 91 cm (3 ft by 3 ft) section was constructed per design. The circumferential reinforcement ratio for Specimen 1 was about 0.0212 and the vertical reinforcement ratio was about 0.0098, similar to the Sandia test specimen.

The Sandia model contained unbonded post-tensioning strands in both the vertical and circumferential directions. In the circumferential direction, post-tensioning strands were spaced every 11 cm (4.4 in), each with about 445 kN (100 kips) of applied force, resulting in a circumferential stress in the concrete of about 12 MPa (1.8 ksi), ignoring Poisson's effect. In the vertical direction, the strands were spaced every 61 cm (2 ft), each with about 445 kN (100 kips) of applied force, resulting in a vertical stress in the concrete of 2.3 MPa (0.3 ksi), ignoring the gravity load and Poisson's effect. To mimic the stress field that is modeled in Sandia's test structure, Specimen 1 was loaded in a similar manner. However, rather than utilizing unbonded post tensioning strands, unbonded steel DYWIDAG bars with an ultimate stress of 1030 MPa (150 ksi) were used, which allowed larger spacing between post-tensioning bars to accommodate anchor plate clearances. In order to mimic the level of stress used in the Sandia specimen, Specimen 1 had nine 36 mm (1.4 in) diameter DYWIDAG bars in the circumferential direction, spaced at 18 cm (7 in), each with about 670 kN (150 kips) of applied force, resulting in a circumferential stress of about 11.5 MPa (1.7 ksi), ignoring Poisson's effect. In the vertical direction, Specimen 1 had three 33 mm (1.3 in) diameter DYWIDAG bars spaced at 61 cm (2 ft), each with about 445 kN (100 kips) of applied force, resulting in a vertical stress of about 2.2 MPa (0.3 ksi), ignoring the gravity load and Poisson's effect. Specimen 1 contained 9 concrete gages with thermocouples to measure concrete strain and temperature over time at three locations through the wall thickness. In addition, 7 of the DYWIDAG post-tensioning steel bars in Specimen 1 were equipped with strain gages to monitor the bar strains over time.

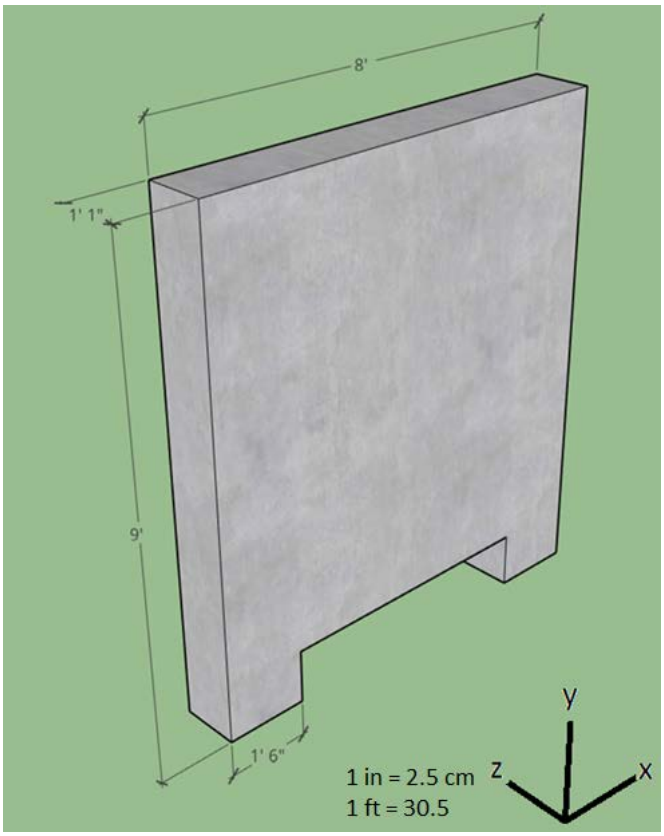

Figure 49 Specimen 1- Dimensions

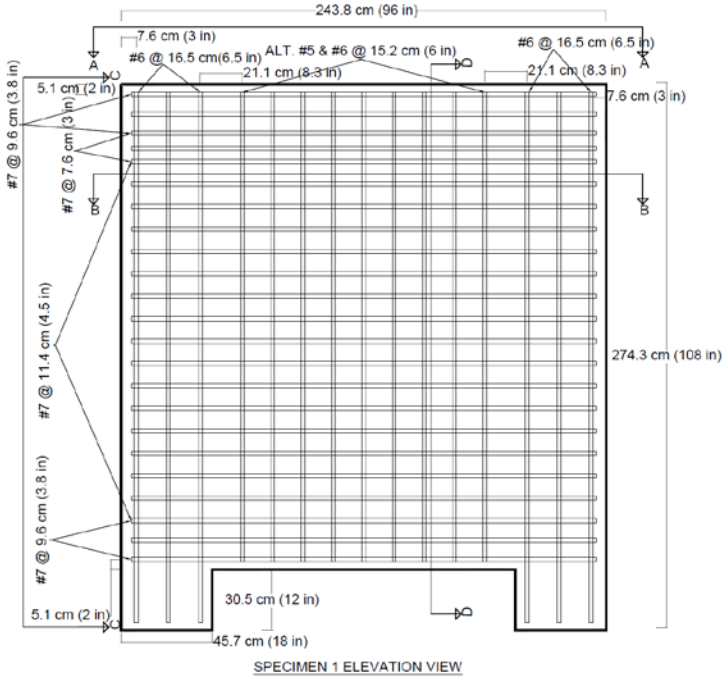

Figure 50 Specimen 1- Reinforcing Steel Layout Elevation View

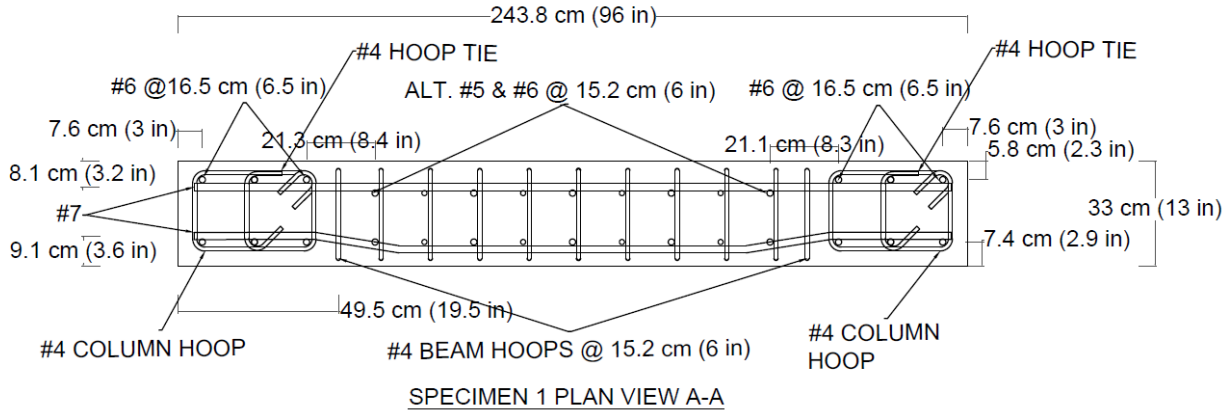

Figure 51 Specimen 1- Reinforcing Steel Layout Plan View A-A

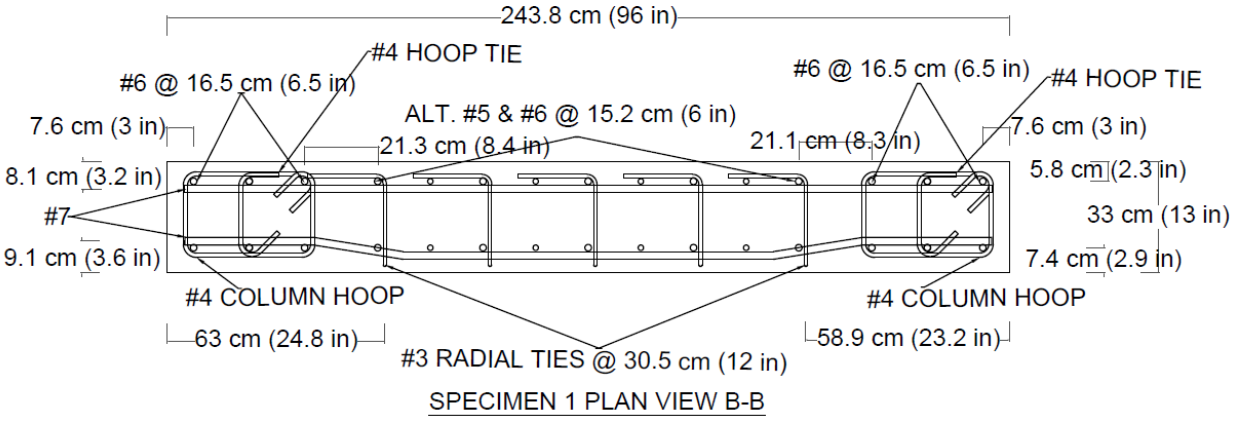

Figure 52 Specimen 1- Reinforcing Steel Layout Plan View B-B

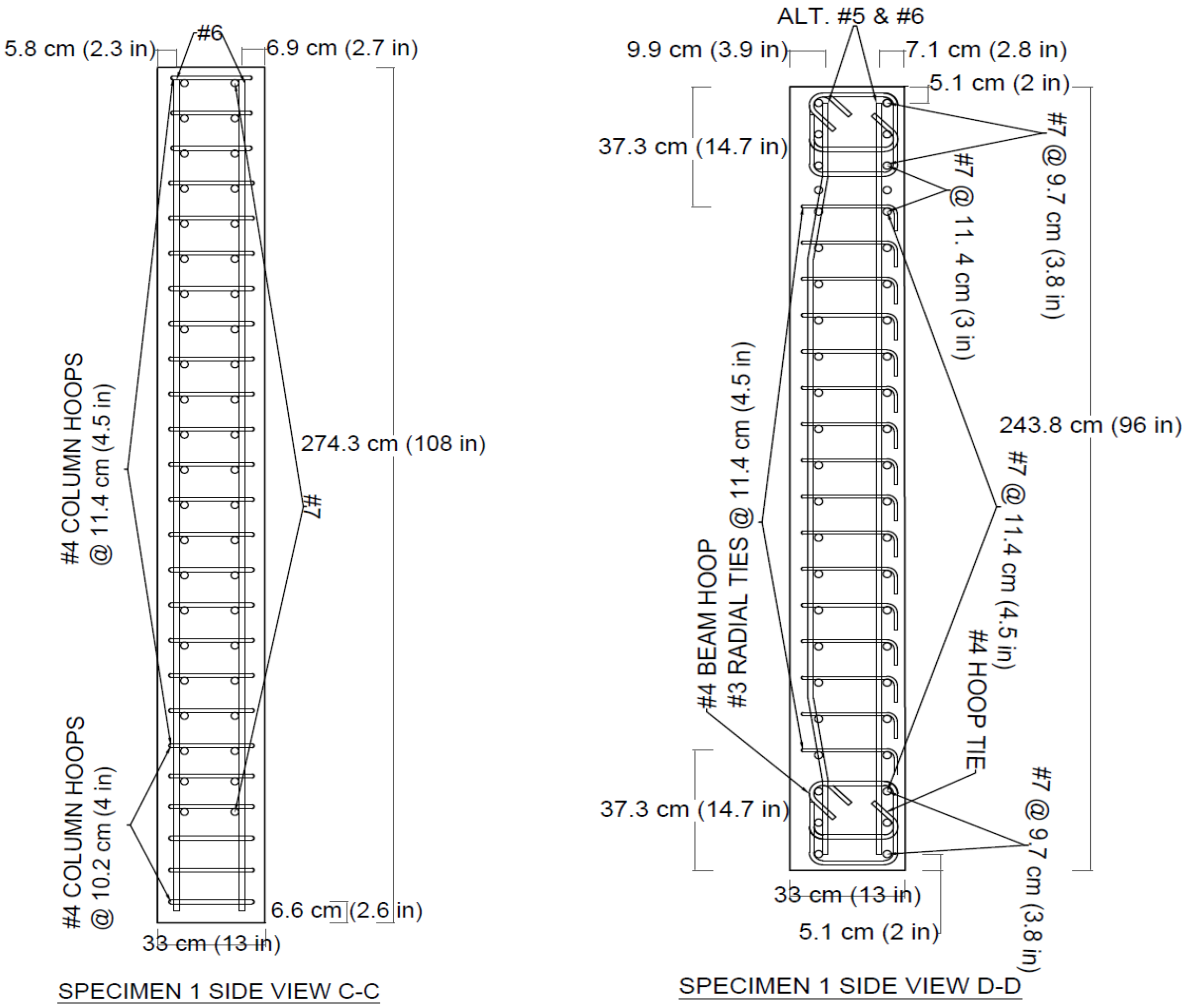

Figure 53 Specimen 1- Reinforcing Steel Layout Side View C-C and View D-D

Figure 54 Specimen 1- Reinforcing Steel Assembled Cage

To capture the effects of changing the geometry and reinforcement ratios (since compression steel is known to reduce the overall influence of concrete creep) in the vertical and circumferential directions on creep propagation, Specimen 2 was designed with 3 times the thickness (Figure 55-Figure 60) of Specimen 1 and about 1/3 of the steel reinforcing ratios (Figs. 16–20). The reinforcement ratios used in Specimen 2 were also a more practicable ratio as used in typical concrete building construction. The level of applied stress was approximately the same for Specimens 1 and 2. The comparison of creep between Specimens 1 and 2 may vary due to differential drying creep through the different thicknesses of the specimens. Thus Specimen 2 was equipped with 9 concrete gages to measure strain and temperature at varying thicknesses of the wall to capture any through thickness differentials. In addition, 14 of the DYWIDAG bars in Specimen 2 were equipped with strain gages to monitor the bar strains over time.

Similar to the assembly of Specimen 1, the vertical perimeter cages were assembled first, then the horizontal perimeter cages were assembled and connected to the vertical cages, and finally the wall face mesh steel was connected to the perimeter cages with radial ties running through the thickness to connect the two mats of steel. The vertical perimeter cages consisted of 8 #9 bars, enclosed in #6 closed hoops spaced vertically at about 11 cm (4.5 in). The horizontal perimeter cages consisted of 8 #10 bars enclosed in #6 closed hoops spaced horizontally at about 20 cm (8 in). The wall face mesh steel consisted of #9 vertical bars spaced at about 0.41 m (16 in) tied directly to #10 horizontal bars spaced at about 23 cm (9 in). #5 radial ties (with 90°and 135° hooked ends) were installed to provide a connection between the two mats of steel. The reinforcement ratio was about 0.0078 in the circumferential direction and 0.0035 in the vertical direction.

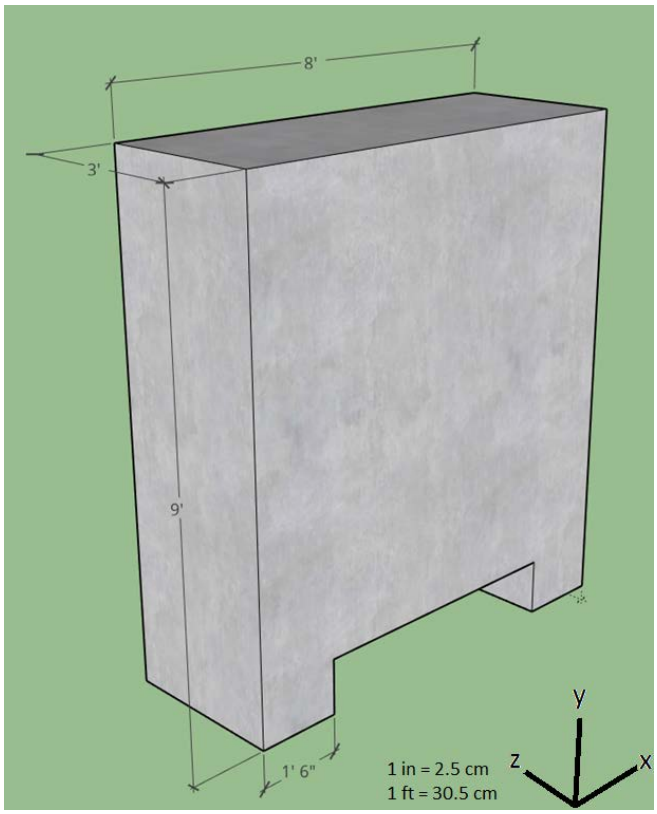

Figure 55 Specimen 2-Dimensions

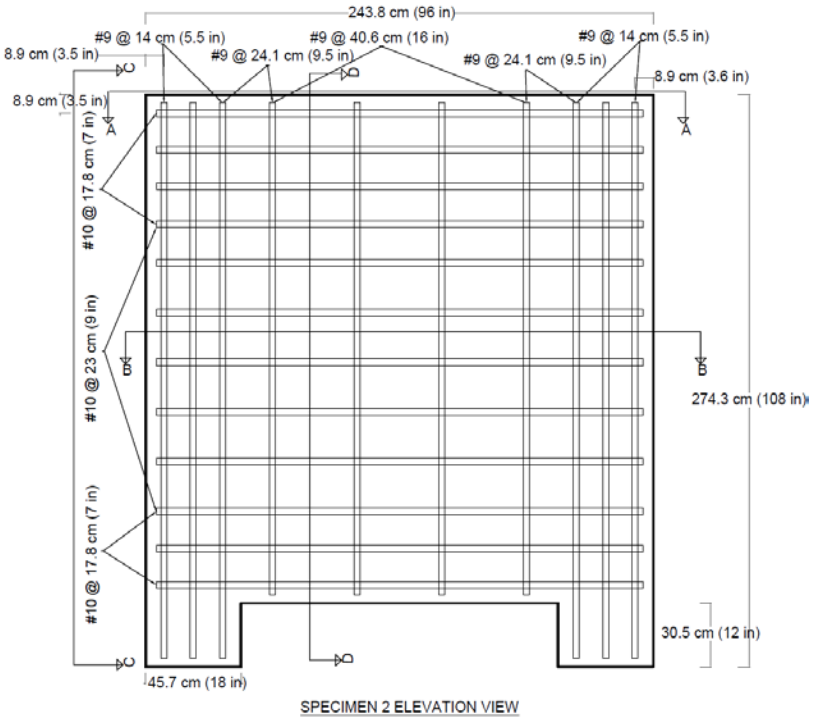

Figure 56 Specimen 2- Reinforcing Steel Layout Elevation View

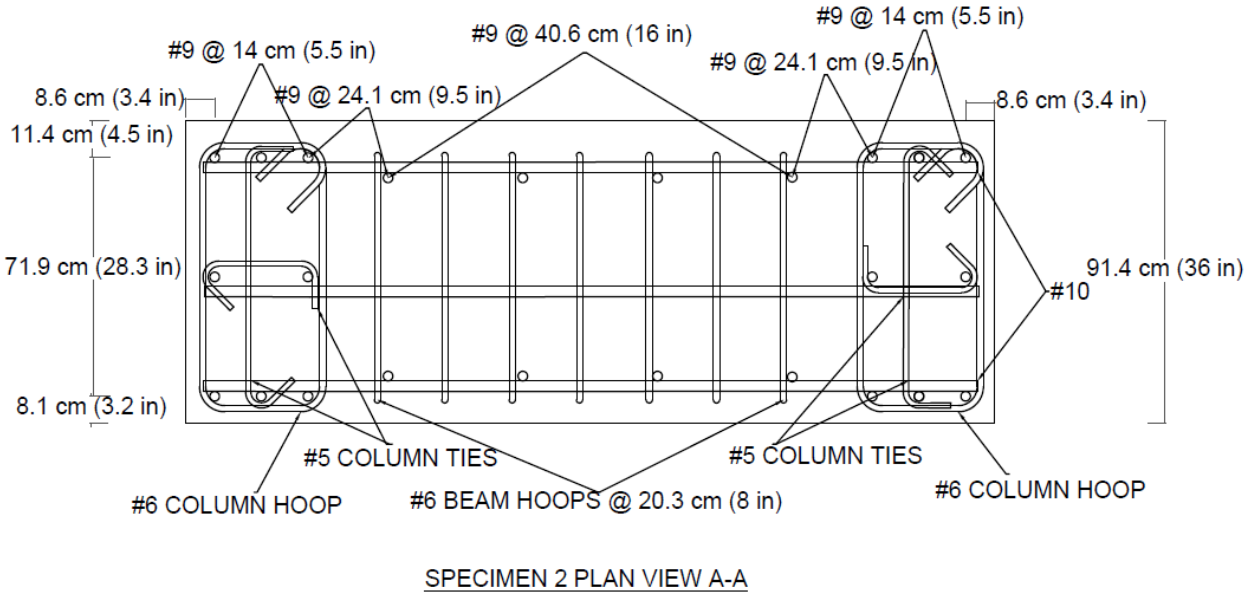

Figure 57 Specimen 2- Reinforcing Steel Layout Plan View A-A

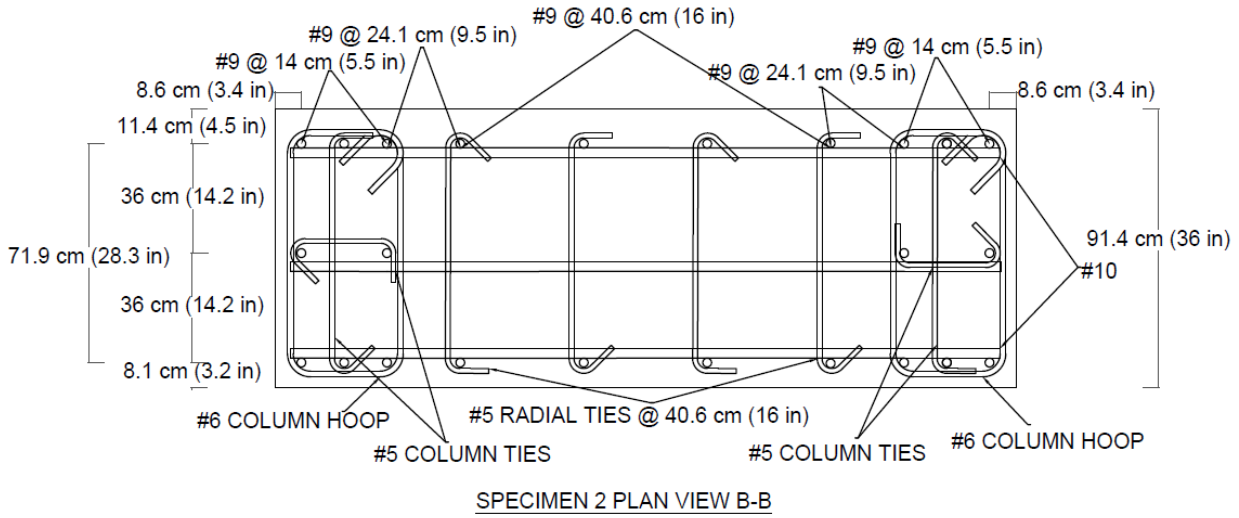

Figure 58 Specimen 2- Reinforcing Steel Layout Plan View B-B

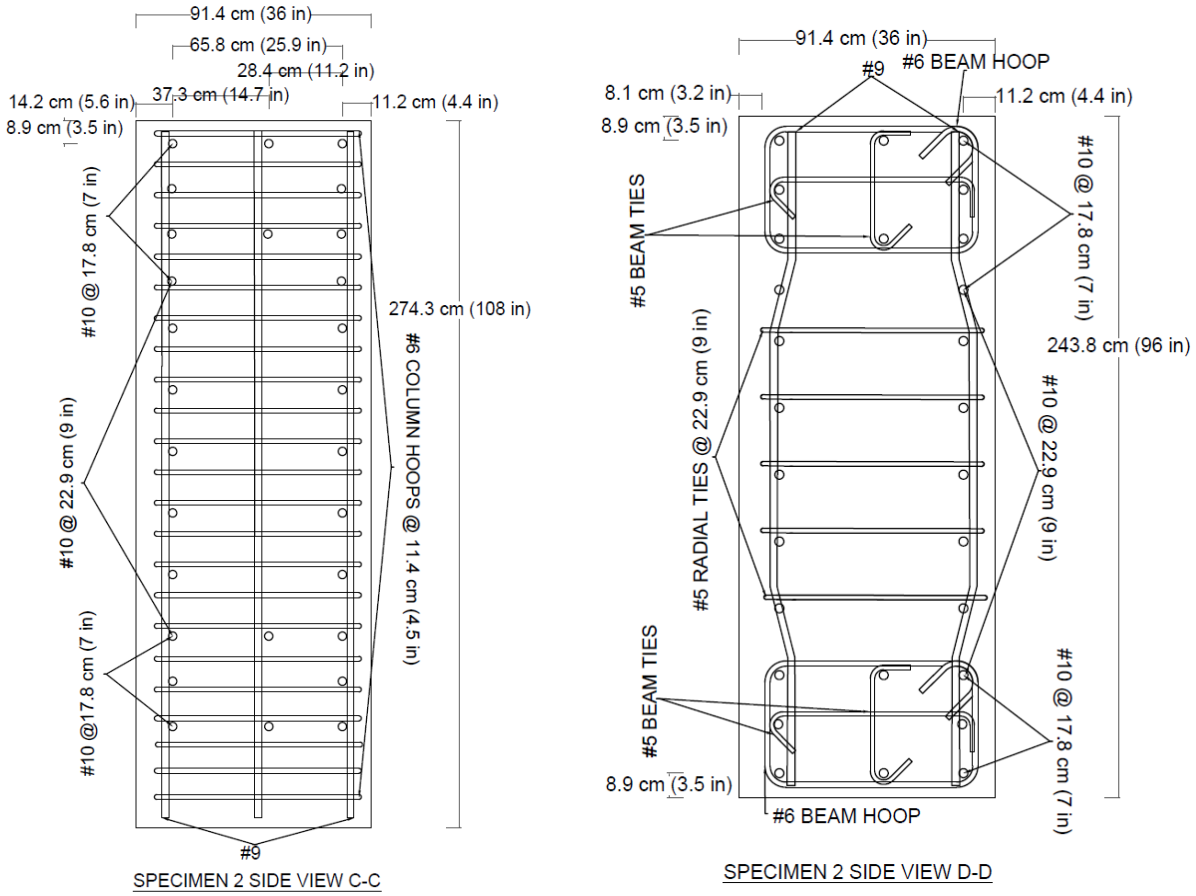

Figure 59 Specimen 2- Reinforcing Steel Layout Side View C-C and View D-D

Figure 60 Specimen 2- Reinforcing Steel Assembled Cage

Specimen 3 (Figure 61) was constructed to serve as a control specimen, containing no reinforcing steel and no post-tensioning bars, in order to identify how the concrete behaves independent of applied loading and reinforcement. Specimen 3 was about 1.5 m (5 ft) tall and 1.5 m (5 ft) wide, with the same thickness as Specimen 2. The dimensions of Specimen 3 were selected to be representative of the larger wall thickness in Specimen 2 and were also limited to the capacity of the crane and the ability to safely lift and move the specimen. Specimen 3 contained 6 concrete gages with thermocouples at varying thicknesses of the wall to measure concrete strain and temperature over time.

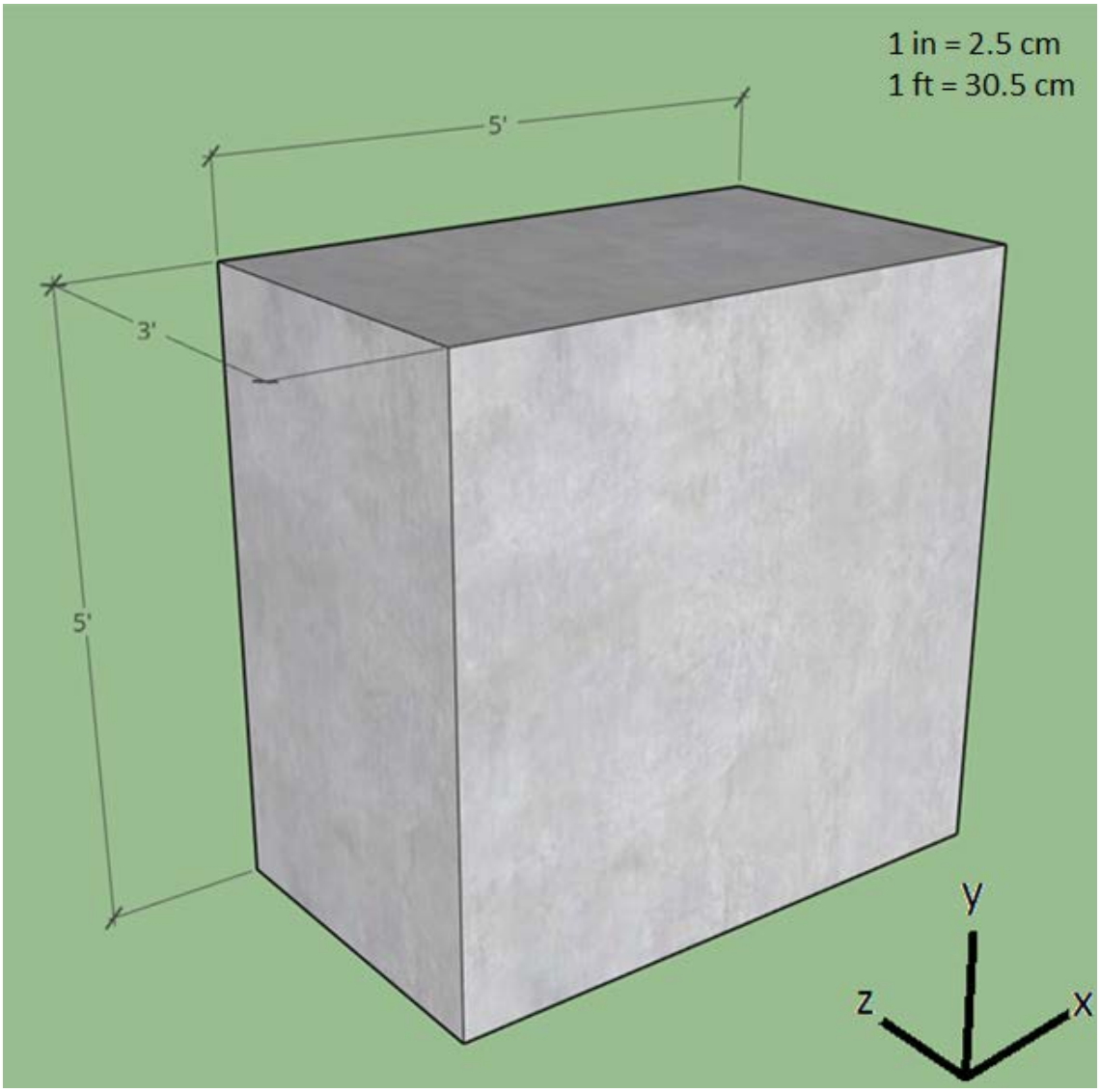

Figure 61 Specimen 3- Dimensions

One side of each of the three wall specimens was sealed by attaching water resistant wrapping such to mimic typical US containment structures. As mentioned before, each specimen was equipped with internal gages to measure the strain in the concrete in 3-dimensions at varying

depths through the wall thickness, as well as thermocouples attached to the internal gages to measure the temperature of the concrete through the thickness. A thermocouple was also added externally to the specimens to measure daily ambient temperatures. Strain gages were attached to select post-tensioning bars used to apply the specimen prestressing to measure the bar strains as well as the changes in strain over time as stress is redistributed from creep and other mechanisms such as temperature changes. Several humidity sensors were also embedded in Specimen 2 to observe the relative humidity as a function of depth through the thickness of the wall, in an attempt to distinguish the influence of drying creep. All sensors were located in the middle 91 cm by 91 cm (3 ft by 3 ft) of each specimen where the uniform biaxial stress distribution from the post-tensioning bars existed.

Measured sensor data was, and continues to be, collected into a data logger for the lifespan of the project and analyzed periodically to observe concrete and post-tensioning strains and temperatures. Data is post-processed and plotted over time to illustrate the trends in each of the sensors as well as the specimens as a whole.

4.4.2 Instrumentation

The instrumentation used for the three specimens was selected carefully based on the demands and expected range of strain and temperature for each wall. The sign convention used for the instrumentation was defined as the x-axis running parallel to the ground, the y-axis running parallel to the vertical post-tensioning steel bars, and the z-axis running through the wall thickness of the specimens. All compression measurements are negative and all tension measurements are positive. Mentions of circumferential, vertical, and radial directions correspond to the x, y, and z directions, respectively.

Full Bridge Concrete Strain Measurements

The full bridge embedded concrete gages used in this study were KM-100BT, manufactured by Tokyo Sokki Kenkyujo Co., Ltd. The gages had an approximate rated output of ±5000 με at 2.5 mV/V within a temperature range of -20 °C to 80 °C, a gage length of 100 mm (3.9 in), and a resistance of 350 Ω (Tokyo Sokki Kenkyujo Co., Ltd. 2017b). These gages are designed with a self-temperature compensated transducer that has a coefficient of thermal expansion similar to that of concrete. These gages were chosen because the loadings designed for Specimens 1 and 2 were expected to produce strains that fell well within the output range. Each gage had an individual offset value that was provided in the product data when the gages were delivered.

The raw data read from the full-bridge concrete strain gages into the data acquisition was in mV/V and converted to με by multiplying by the excitation voltage of 2.5 V and multiplying by 1000 to convert units from mε to με. In summary, the conversion of raw data from the concrete gages in mV/V to με is:

$$Concrete\ gage\ strain\ [\mu\varepsilon] = Raw\ data\left[\frac{mV}{V}\right] * Excitation\ voltage[2.5\ V] * \left[1000\ \frac{\mu\varepsilon}{m\varepsilon}\right] \quad (52)$$

A total of 24 concrete gages were installed in the 3 specimens, measuring the strain in the concrete in the x, y, and z directions at various depths of the wall thicknesses.

Half Bridge Strain Measurements on Post-Tensioning Steel

Strain gages attached to the post-tensioning steel bars were type FCA-6-11, manufactured by Tokyo Sokki Kenkyujo Co, Ltd. The gages had a gage length of 5 mm (0.2 in), a gage width of 2.3 mm (0.09 in), a backing diameter of 14 mm (0.6 in), a resistance of 120 Ω, a gage factor of 2.1, and were composed of 2 stacked elements 90° from each other (Tokyo Sokki Kenkyujo Co., Ltd. 2017a). Each strain gage had a strain limit of ±5% or 50,000 με. The maximum strain expected to be induced in the post-tensioning bars was about 4200 με, therefore these gages were deemed appropriate.

The raw data read from the half-bridge strain gages into the data acquisition was in με, therefore no conversion was required in the post-processing. However, some data offsets developed during the installation of the post-tensioning bars and were corrected during post-processing.

Thermocouple Measurements

The thermocouples were housed within the KM-100BT full bridge concrete gages, allowing for the simultaneous measurement of strain and temperature at a point (Tokyo Sokki Kenkyujo Co., Ltd. 2017b). The thermocouples were type T with an operating range of -20°C to 80°C. As per Japanese manufacturing convention, the thermocouples contained a white (-) and a red (+) wire. The wires needed to be extended due to the distance between the data acquisition and the specimens. The extension wire used in this project was United States grade, conventionally blue wire (+) and red wire (-). The data read from the thermocouples into the data acquisition was in °C. An additional thermocouple was added to the outside of Specimen 2 to monitor ambient temperature as a means for comparing outside temperature fluctuations (daily and seasonally) with internal concrete temperature fluctuations.

Data Acquisition

The data acquisition system, shown in Figure 62 that was developed for this project was a Campbell Scientific system composed of a CR1000 data logger, three AM16/32B multiplexers for the concrete gages and post-tensioning bar strain gages, and an AM25T multiplexer for the thermocouples. The system was designed with a solar panel connected to a backup battery for continuous power. The data logger was programmed to collect a data point for all of the gages once per hour.

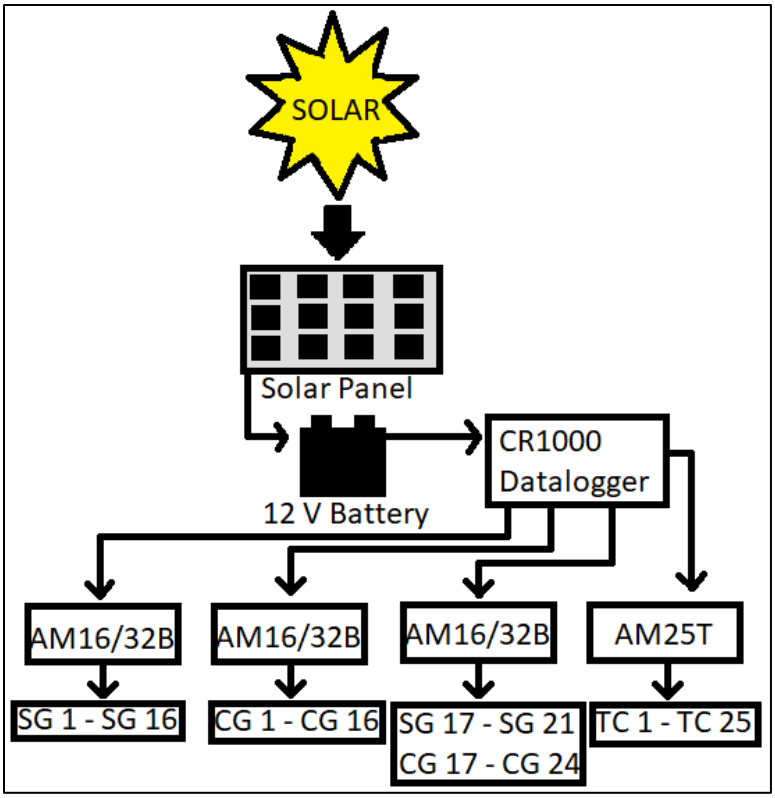

Figure 62 Representation of Data Acquisition Set Up

4.4.3 Concrete Mix Design

The materials used to construct the specimens were carefully selected to mimic those used in actual containment vessels. As used in the smaller scale materials for concrete creep test in laboratory, the same mix was used in the design of large-scale specimens. The concrete mix had an estimated 28-day compressive strength of about 38 MPa (5.5 ksi) and a design slump of about 150 mm (6 in).

Reinforcement Steel

The large-scale specimens were fabricated with Grade 60 side face mesh reinforcement steel in accordance with ASTM A615 specifications (American Society for Testing and Materials 2016).

Post-Tensioning System

The unbonded post-tensioning steel bars used in the stressing procedures of Specimens 1 and 2 were threadbars manufactured by DYWIDAG-Systems International, conforming to ASTM A722 with an ultimate stress of 1034 MPa (150 ksi) (Dywidag-Systems International 2016). The circumferential bars were about 35 mm (1.4 in) diameter, with a cross sectional area, A_{ps}, of about 1,020 mm^2 (1.6 in^2), and an ultimate stress, f_{pu}, of 1030 MPa (150 ksi). The vertical bars were about 33 mm (1.3 in) diameter, with a cross sectional area, A_{ps}, of about 806 mm^2 (1.3 in^2), and an ultimate stress, f_{pu}, of 1030 MPa (150 ksi).

Both the circumferential bars and vertical bars were initially pulled to a stress of about 0.65 f_{pu}, resulting in a force of about 667 kN (150 kips) for the horizontal bars, and about 534 kN (120 kips) in the vertical bars. After anchoring and lock off, the stress in the bars dropped to about 0.53 f_{pu}, resulting in about 534 kN (120 kips) of force in the horizontal bars, and about 445 kN (100 kips) of force in the vertical bars. Once the steel reinforcement was assembled for Specimens 1 and 2, the plastic post-tensioning ducts were installed through the cages to provide hollow holes for the post-tensioning bars to be inserted after the concrete was poured as shown in Figure 63-Figure 65.

Figure 63 Specimen 2- Post-Tensioning Bar Ducts, Reinforcing Steel Cage, and Formwork View from Between Specimen 2 Feet

Formwork Assembly

Formwork bases and walls consisted of 20 mm (0.8 in) plywood supported by 50 mm by 152 mm (2 in by 6 in) boards at a spacing of about 31 cm (12 in) center to center and braced with 50 mm by 152 mm (2 in by 6 in) boards for lateral support.

Figure 64 Specimen 2- Formwork

Concrete Gage Installation

Once the formwork was assembled and the reinforcing steel cages were lifted into the formwork, the concrete gages were attached to the reinforcing steel of Specimen 1 and 2 and to a smooth steel support in Specimen 3.

Nine concrete gages were installed in Specimen 1 with 3 bundles of 3 gages (x, y, and z-directions) at 3 different depths, all located within the center 91 cm by 91 cm (3 ft by 3 ft) of the specimen. Gages 1 through 3 (1 corresponding to the x-direction, 2 corresponding to the y-direction, and 3 corresponding to the z-direction) were installed in the cover at about 5 cm (2 in) from the surface of the side of Specimen 1 without weatherproofing. Gages 4 through 6 were installed in the center depth of Specimen 1 at about 17 cm (6.5 in). Finally, gages 7 through 9 were installed in the cover of the face of Specimen 1 that had the weatherproofing. All gages were attached to reinforcing steel with zip ties and tie wire to ensure alignment in the correct direction and to ensure maximum contact with concrete on all sides of the gages. Some initial strains were induced in the concrete gages because of the way they were attached to the reinforcing steel cage for proper alignment in their respective directions. These initial strains and offsets were accounted for in post-processing and the gages were zeroed just prior to when the concrete was poured.

Similarly, to Specimen 1, 9 concrete gages were installed in Specimen 2, similar to the layout of Specimen 1. However due to the depth of Specimen 2 (91 cm, 36 in), it was impossible to reach into the bottom of the reinforcing steel cage to install gages in the cover of the face of the specimen that was not weatherproofed (Figs. 24 and 44). Therefore, gages 10 through 12 were installed in the cover of the face with weatherproofing, gages 13 through 15 were installed at the quarter point of the depth (about 23 cm, 9 in) and gages 16 through 18 were installed at the center of the depth (about 46 cm, 18 in).

6 concrete gages were installed in Specimen 3 with 2 bundles of 3 gages in the x, y, and z-directions. Gages 19 through 21 were installed in the center depth of Specimen 3 at about 46 cm (18 in) and gages 22 through 24 were installed in the cover Specimen 3 without weatherproofing. Since there was no reinforcing steel to attach the gages to in Specimen 3, the gages were attached to a smooth steel support.

Before pouring the concrete, the gages were connected to the data acquisition (DAQ) to ensure that they responded to daily temperature changes. When the concrete was poured, care was taken to ensure that concrete was not poured directly on top of the gages to avoid shifting them in any direction.

28-day compressive strength tests were conducted on 3 cylinder samples from each truck. The samples from truck 1 (Specimen 2) had an average compressive strength of 37.9 MPa (5.5 ksi) and the samples from truck 2 (Specimens 1 and 3) had an average compressive strength of 32.3 MPa (4.7 ksi). Both strengths were slightly lower than the anticipated values from the smaller scale materials testing. However, the concrete was judged to be sufficient for this research.

28 day split tensile tests were also conducted on 3 cylinder samples from each truck. The samples from truck 1 (Specimen 2) had an average splitting tensile strength of 2.9 MPa (426 psi) and the samples from truck 2 (Specimens 1 and 3) had an average splitting tensile strength of 2.6 MPa (377 psi).

Post-Tensioning Installation

Twenty-one half bridge strain gages were attached to 21 post-tensioning steel bars in the climate controlled High Bay Lab at Texas A&M University. When the post-tensioning bars arrived to the site, the bars were placed into the ducts with the thinner diameter bars (about 33 mm, 1.3 in) running through the vertical ducts and the thicker diameter bars (about 36 mm, 1.4 in) running through the horizontal ducts. Due to the high concentration of reinforcing steel in the specimens, some of the ducts were slightly curved after concrete placement and some of the post-tensioning bars had to be forced into the ducts with a sledgehammer, which resulted in damage to some of the strain gages. Once all of the post-tensioning bars were placed in the ducts, the anchor plates were slipped on both ends of the bars and the nuts were loosely screwed onto the bars thereafter. Finally, the extension wires that were attached to the bars with strain gages were connected into the data acquisition.

Post-tensioning operations began about 46 days after the concrete was poured, beginning with the vertical bars of Specimen 2. The vertical bars were loaded with a hydraulic jack to about 534 kN (120 kips), about 15% more than the desired force of about 445 kN (100 kips) to account for losses from lock-off. Once the desired strain was attained, the nut was tightened by hand on the side of the bar where the jack was located and then the hydraulic jack was unloaded. As a result of unloading the hydraulic jack, the strain in the bar fell slightly due to anchoring and seating of the bar at the specimen ends. Next, the circumferential bars of Specimen 2 were loaded. It was

initially planned to pull the circumferential bars with 800 kN (180 kips). However, the force capacity of the jack made it dangerous to exceed 667 kN (150 kips). Therefore, the circumferential bars were pulled with about 667 kN (150 kips), which resulted in a force of about 534 kN (120 kips) once the bars were unloaded and locked-off. Specimen 1 vertical bars were loaded next to the same force as the vertical bars in Specimen 2. Finally, the circumferential bars in Specimen 1 were loaded to the same level of force as the circumferential bars in Specimen 2.

For Specimen 1, the amount of stress on the concrete from the post-tensioning in the x-direction was approximately 11.5 MPa (1.7 ksi) and was about 2.2 MPa (0.3 ksi) in the y-direction, neglecting biaxial loading effects and gravity load. For Specimen 2, the stress on the concrete in the x-direction was close to 14 MPa (2 ksi) and was about 3.5 MPa (0.5 ksi) in the y-direction, neglecting biaxial loading effects and gravity load.

Out of the 21 strain gages that were originally attached to the post-tensioning bars, only 10 survived the post-tensioning operations. The gages that were not functioning were excluded in the results section of this study.

Figure 65 Specimen 2- Post-Tensioning Bars with Anchor Plates and Nuts, Side View

4.5 Results and Discussion

4.5.1 Instrumentation Data as a result of Post-Tensioning Operations

Specimen 1

The concrete gages (CG 1 through 9) remained relatively stable up to the day of post-tensioning reflecting only the strains induced from temperature changes. For most of the concrete gages

embedded in Specimen 1, there was an evident spike in strain when post-tensioning operations took place.

On average in the x-direction (CG 1, 4, and 7), there was a total compressive strain of approximately -600 με as a result of post-tensioning operations. With the applied loading, the concrete gages in the x-direction were expected to notice an induced strain of about -423 με. The estimated strain was calculated based on the following formula, where the total applied force per bar is divided by the approximated modulus of elasticity (27.8 GPa, 4030 ksi, estimated based off of American Concrete Institute 2014), the net area (area of the wall in between the post-tensioning bars minus the area of the post-tensioning duct) and multiplied by 1,000,000 to convert strain to microstrain:

$$Est.\,Concrete\ Strain\ [\mu\varepsilon] = \frac{Jacking\ Force}{[Area\ between\ PT\ bars - Area\ duct] * E} * \left[1{,}000{,}000\ \frac{\mu\varepsilon}{\varepsilon}\right] \quad (53)$$

In the y-direction, CG 2 (in the cover of the specimen on the face of the wall without weatherproofing) read a slightly compressive strain, whereas CG 5 (in the middle thickness of the specimen) and CG 8 (in the opposite cover of the specimen) read tensile strains. Thus, the sign difference reduced the average strain in the y-direction to a lesser value of about 63 με. With the applied loading, the concrete gages in the y-direction were expected to notice an induced strain of about -80 με from eqn. (53). However, the strain estimations did not take into consideration the effects of the 3D stress field and Poissons effect. In the z-direction (CG 3, 6, and 9), CG 3 (in the cover of the specimen on the face of the wall without weatherproofing), CG 6 (in the middle thickness of the specimen) and CG 9 (in the opposite cover of the specimen) read tensile strains. The average strain in the concrete in the z-direction as a result of post-tensioning was about 180 με.

Specimen 1 was first post-tensioned in the y-direction (with the post-tensioning bars aligned at about the center of the thickness of the specimen) and then it was later post-tensioned in the x-direction with a larger jacking force, resulting in an increase of compressive stress in the x-direction. Therefore, it makes sense that the strains in the x-direction were all compressive, and that there was a variation of smaller compressive and tensile strains in the y-direction and z-direction due to Poissons effect. As the specimen was post-tensioned, it was laying on its face with gage bundles CG 1-3 at the top, CG 4-6 in the middle, and CG 7-9 at the bottom, nearest to the base formwork. Thus, when Specimen 1 was post-tensioned in the y-direction, CG 2, 5, and 7 all went into compression until post-tensioning force was applied in the x-direction. It makes sense that CG 2 (in the cover and above the post-tensioning bars) went into compression and stayed in compression when the x-direction bars were pulled because the face of the concrete at the top was free. Whereas in the center of the specimen where CG 5 ran in the y-direction and CG 6 ran in the z-direction, it follows that the concrete experienced a tensile change in strain when the x-direction bars were pulled because the stress in the x-direction was larger (a result of the Poissons effect). Similarly, CG 8 and CG 9 experienced a tensile change in strain after the x-direction bars were

pulled, most likely because the face of the concrete where the gages were located was not free and was subjected to the weight of the concrete itself, along with the larger stress induced in the x-direction from the post-tensioning operations.

After post-tensioning operations were completed, the concrete gages experienced strain variations due to daily temperature fluctuations. The thermocouple readings indicated the temperature in the concrete in the same location as each respective concrete gage. The thermocouples in Specimen 1 did not show a strong relationship between the temperatures of the concrete and depth of embedment through the thickness of the wall, most likely because the wall was relatively thin compared to Specimen 2.

The strain gages on the post-tensioning bars in Specimen 1 (SG 2, 3, and 5 in the x-direction, and SG 6 and 7 in the y-direction) each exhibited similar behavior to one another. Each bar was pulled to a certain force, and because of losses during the lock-off and anchoring, the resulting force was reduced on average by about 25%. Strain gage 2 indicated a maximum strain about 1000 με less than that of strain gages 3 and 5, therefore there may have been some malfunctioning occurring in the sensor. Excluding strain gage 2, in the x-direction the strain gages on the post-tensioning bars indicated an average maximum strain of about 2700 με, where the expected value for the maximum strains induced on the horizontal bars was about 3400 με, obtained from the following equation:

$$Est.\,PT\ Bar\ Strain\ [\mu\varepsilon] = \frac{Jacking\ Force}{Area\ of\ Bar * E} * \left[1{,}000{,}000\ \frac{\mu\varepsilon}{\varepsilon}\right] \tag{54}$$

where the jacking force in the x-direction was about 667 kN (150 kips), the area of the bar was about 1020 mm^2 (1.6 in^2) and the modulus of elasticity was about 205 MPa (29700 ksi). In the y-direction the strain gages on the post-tensioning bars indicated an average maximum strain of about 2900 με, where the expected value was about 3200 με, obtained from eqn. (54), assuming a jacking force of 534 kN (120 kips) and a bar area of 806 mm^2 (1.3 in^2).

Specimen 2

Similar to Specimen 1, the concrete gages in Specimen 2 (CG 10 through 18) remained relatively stable up to the day of post-tensioning.

On average in the x-direction (CG 10, 13, and 16), there was a compressive strain of approximately -360 με induced by the post-tensioning operations with each gage reading a compressive value. With the applied loading, the concrete gages in the x-direction were expected to experience an induced strain of about -510 με from eqn. (52). In the y-direction CG 11 (in the cover of the specimen on the face of the wall without weatherproofing) malfunctioned and is thus neglected in the analysis. CG 17 (located in the middle of the specimen) read a tensile change in strain, whereas CG 14 (located 23 cm, 9 in into the thickness of the specimen) read a compressive change in strain. Thus, the sign difference reduced the average strain in the y-direction to a lesser value of -10 με. With the applied loading, the concrete gages in the y-direction were expected to

experience an induced strain of about -130 με from eqn. (52). However, similar to the estimation made for Specimen 1, these strain predictions did not consider the effects of the 3D stress field and Poissons effect. All of the concrete gages in the z-direction (CG 12, 15, and 18) read tensile changes in strain, averaging to about 125 με as a result of post-tensioning.

Specimen 2 was first post-tensioned in the y-direction (with three layers of post-tensioning bars) and then it was later post-tensioned in the x-direction with a larger jacking force, resulting in an increase of compressive stress in the x-direction, causing compressive strains for all of the gages running in the x-direction. Similar to Specimen 1, there was a strain sign variation in the y-direction, most likely due to the fact that CG 14 was located in between the center of the thickness of the specimen and the top cover, where a high level of compressive stress was induced. CG 17 was strained in tension as the x-direction bars were pulled, indicating that the stress in the x-direction overcame that of the y-direction, and inducing a tensile strain because of the Poissons effect. As the specimen was post-tensioned, it was laying on its face with gage bundles CG 10-12 at the top, CG 13-15 in the quarter point (23 cm or 9 in), and CG 16-19 at the center thickness of the specimen, about 46 cm (18 in) below the top bundle. Similar to Specimen 1, all of the z-direction gages (CG 12, 15, 18) in Specimen 2 had induced tensile strains when the post-tensioning stresses were applied.

The thermocouples in Specimen 2 also captured temperature data. There was clearly less movement in the temperature data associated with increased embedment depth of the gages associated with Specimen 2 than compared to Specimen 1. There was a more obvious trend with the thermocouples in Specimen 2 showing less temperature variation for the gages that were embedded deeper in the thickness of the specimen.

The strain gages on the post-tensioning bars in Specimen 2 (SG 8, 10, 15, and 16 in the x-direction, and SG 18 in the y-direction) each exhibited similar behavior as the post-tensioning bar strain gages in Specimen 1. Each bar was pulled to a certain force, and because of losses during the lock-off and anchoring, the resulting force was reduced on average by about 32%. Strain gages 8 and 15 indicated about 50% losses from the maximum strain, therefore there may have been some malfunctioning occurring in the sensors. In the x-direction the strain gages on the post-tensioning bars indicated an average maximum strain of about 2800 με, where the expected value for the maximum strains induced on the horizontal bars was about 3400 με, obtained from eqn. (53), where the jacking force in the x-direction was about 667 kN (150 kips), the area of the bar was about 1020 mm^2 (1.6 in^2) and the modulus of elasticity was about 205 MPa (29700 ksi). In the y-direction the strain gages on the post-tensioning bars indicated an average maximum strain of about 2600 με, where the expected value was about 3200 με, obtained eqn. (53), assuming a jacking force of 534 kN (120 kips) and a bar area of 806 mm^2 (1.3 in^2).

4.5.2 Instrumentation Data from Post-Tensioning to End of Project

Specimen 1

As indicated above, Specimen 1 contained 9 concrete gages, 9 thermocouples, and 5 properly functioning post-tensioning bar strain gages.TC 8 began to malfunction after post-tensioning took place and was thus neglected in the following analysis of Specimen 1.

In the x-direction, the average change in concrete strain over the project period was approximately -400 με (from to -420 με to -820 με), indicating that the concrete was becoming more compressive in the x-direction. A part of this compressive behavior may be attributed to the seasonal temperature variations. The strain gages attached to the post-tensioning bars in the x-direction experienced an average change in strain of about -300 με (from 2200 με to 1900 με), indicating that the tensile forces in the post-tensioning bars were reducing as time passed. SG 2 and SG 3 both experienced a compressive change in strain, whereas SG 5 malfunctioned and was not included in the average strain change formulation.

In the y-direction, the average change in concrete strain over the project period was approximately -50 με (from 100 με to 55 με), indicating a slight compressive strain. The strain gages attached to the post-tensioning bars in the y-direction experienced an average change in strain of about -250 με (from 2500 με to 2250 με), indicating that the bars were losing some of the initial post-tensioning force.

In the z-direction, the average change in concrete strain was about 70 με (from 180 με to 250 με), indicating tensile strain due to Poisson's effect.

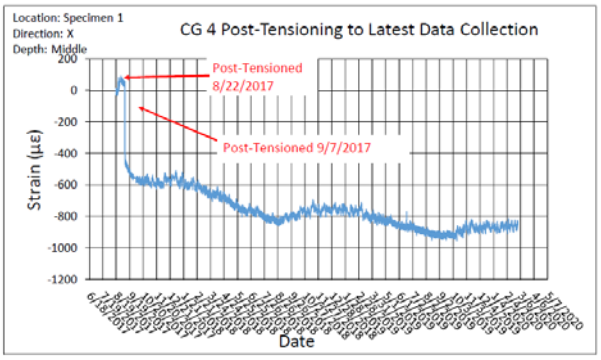

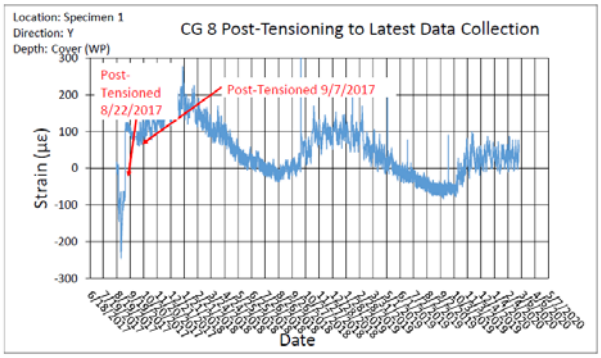

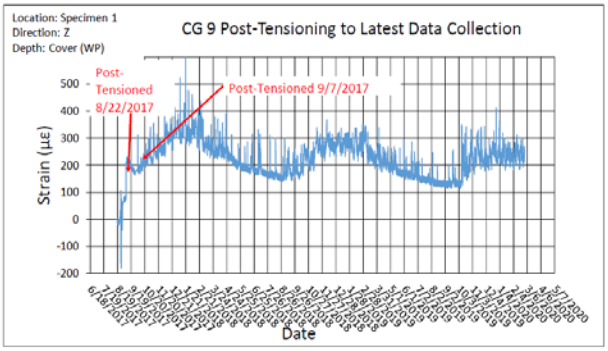

Figure 66. Concrete Gage – Strain Data from Specimen 1 in x, y and z-direction

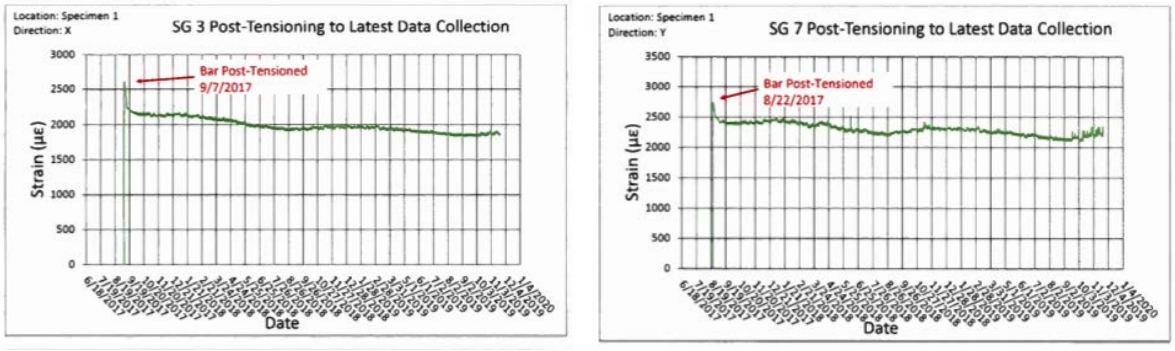

Figure 67. Post-Tensioning Bar Strain Gage Data from Specimen 1 in the x and y-direction.

Specimen 2

As mentioned before, Specimen 2 contained 9 concrete gages, 9 thermocouples and 5 properly functioning post-tensioning bar strain gages.

In the x-direction, the concrete gages experienced an average change in strain of about -450 με (from -500 με to -950 με) over the project period. The strain gages on the post-tensioning bars in the x-direction endured an average change of strain of about -350 με (from 2750 με to 2400 με), indicating that the bars were losing their tensile force over time, which was expected with the change in temperature and as a result of relaxation and primary and secondary creep.

In the y-direction, the average change in strain in the concrete was approximately -80 με (from -120 με to -200 με), indicating that the concrete in the y-direction was experiencing compression over time.

In the z-direction, the average change in concrete strain was about 75 με (from 0 με to 75 με), indicating an increase in tensile strain through the thickness of the specimen. This average change in strain was more than that found in the z-direction in Specimen 1 and may be attributed to the larger thickness of Specimen 2.

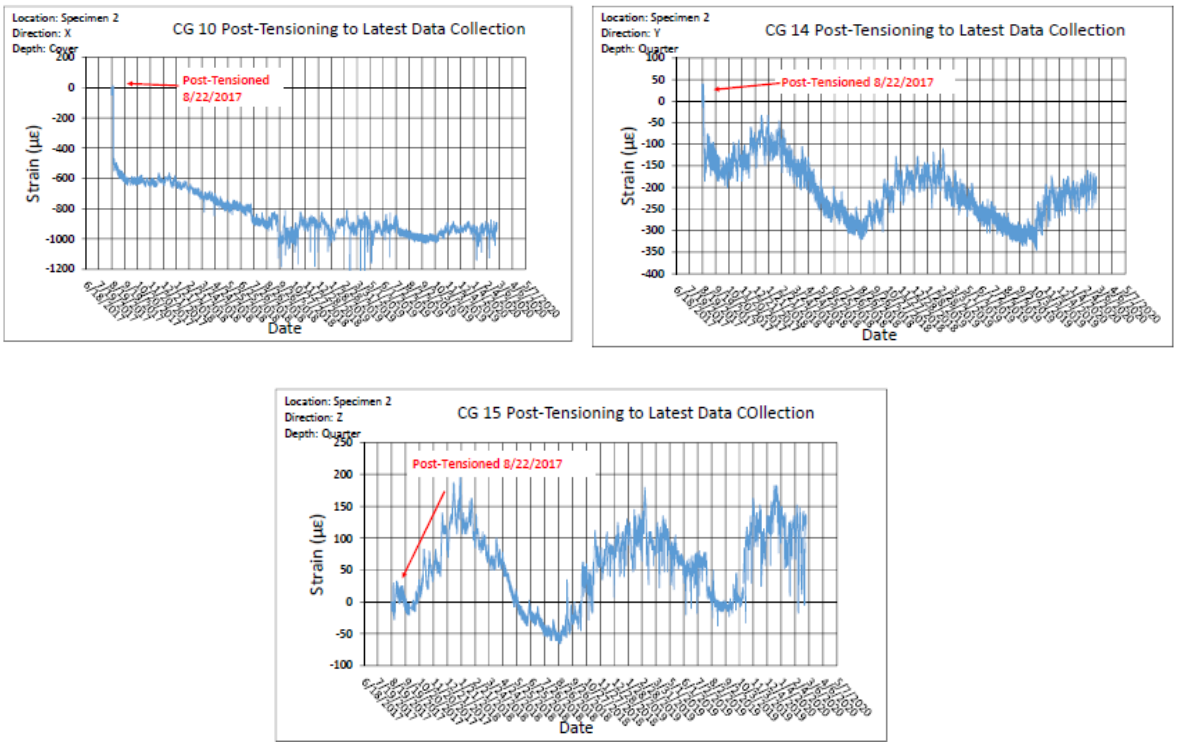

Figure 68. Concrete Gage – Strain Data from Specimen 2 in x, y and z-direction

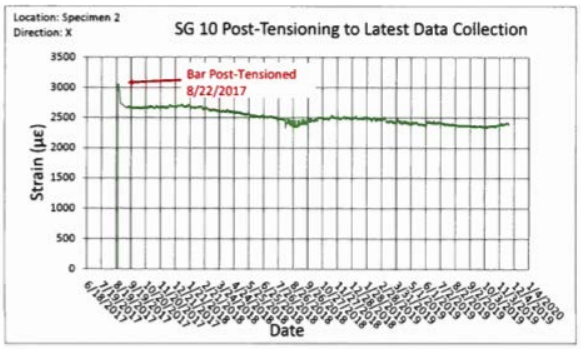

Figure 69. Post-Tensioning Bar Strain Gage Data from Specimen 2 in the x-direction.

Specimen 3

Specimen 3 contained 6 concrete gages and 6 thermocouples. Of the 6 concrete gages, CG 19, CG 21 and 23 continued to malfunction and were thus ignored in the analysis of Specimen 3. Specimen 3 experienced an average change in concrete strain of approximately -200 με in the x-direction (from 0 με to -200 με) and 0 με in the y-direction. Since only one gage was functioning properly in each direction, it was difficult to identify the relationship between concrete depth and strain variation. It was expected that the purely concrete block experienced tensile/compressive strain due to the outside temperature variations in the environment. However, since half of the gages in Specimen 3 malfunctioned, it is difficult to confirm the validity of the results.

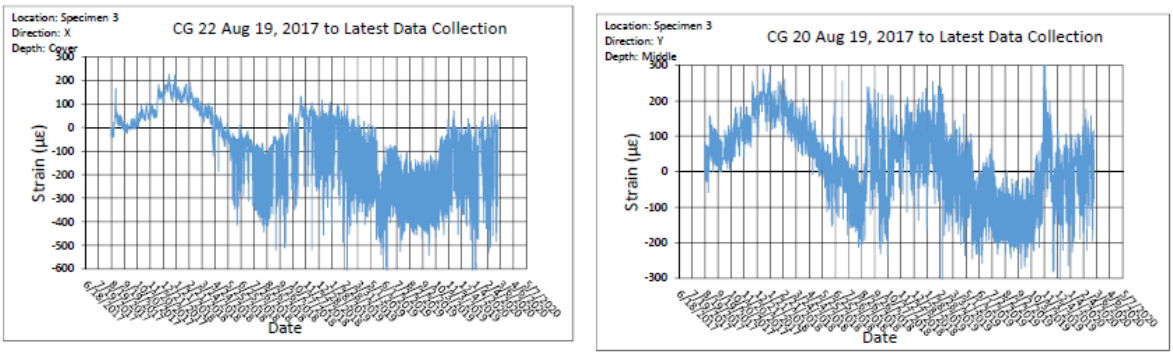

Figure 70. Concrete Gage – Strain Data from Specimen 3 in x and y-direction

Thermocouple Measurements

The thermocouple measurements in Specimen 1, 2 and 3 were monitored throughout the project period and presented in the graphs below.

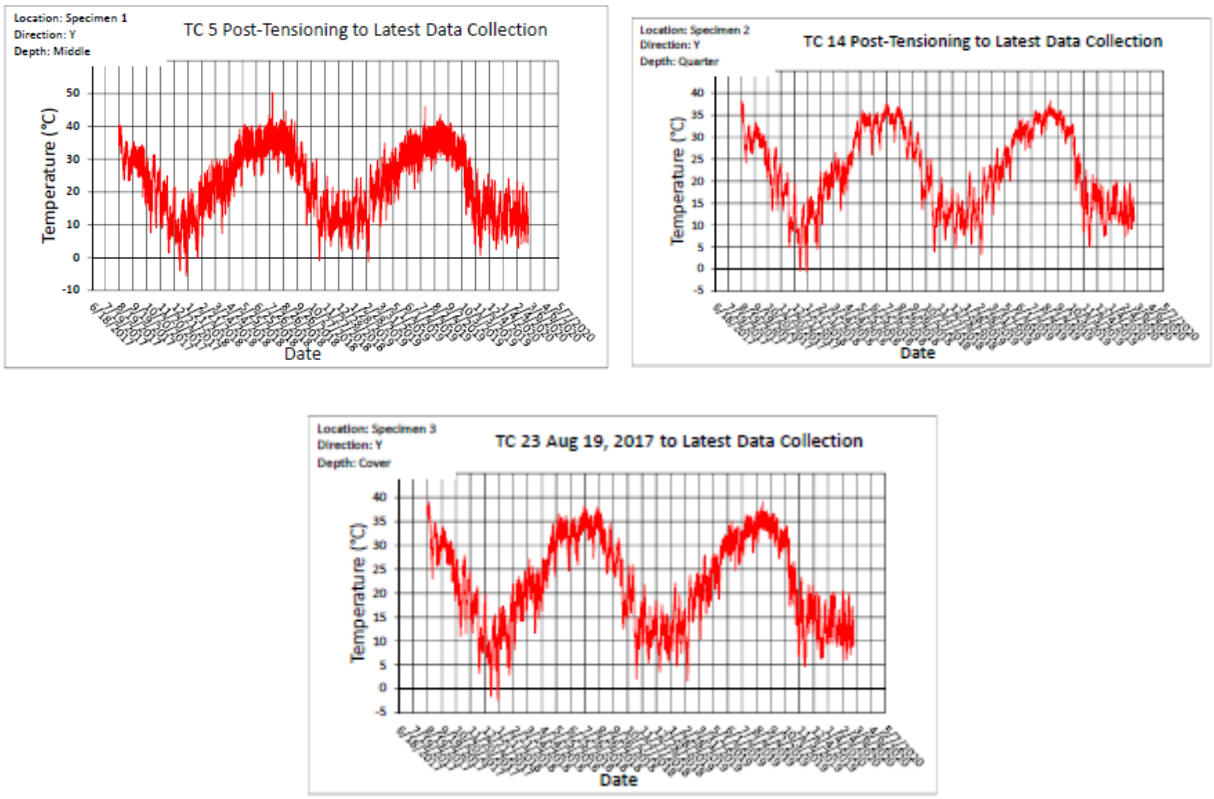

Figure 71.Thermocouple Temperature Data from Specimen 1, 2 and 3

Relative Humidity Measurements

Along with temperature measurements, Relative Humidity was investigated in large-scale specimens by drilling several holes at various critical depths (¼", ½", 1", 3", 5"), where 5" being

the deepest from the wall surface exposed. For this purpose, HIH-4000 humidity sensors from Honeywell was used. The sensor reads a voltage reading which can be converted to RH data using the sensors calibration constants. The RH values at five different months (Mar, May, Sept, Nov and Feb) was recorded to understand how it varies round the year. It was observed that the sensor at ¼" depth > 75% and the sensors at 3" and 5" were ~ 100% throughout the year. This confirms the assumption made at the beginning of the project that drying plays a role only near the surface exposed to environment and can be neglected in the study as second order effect.

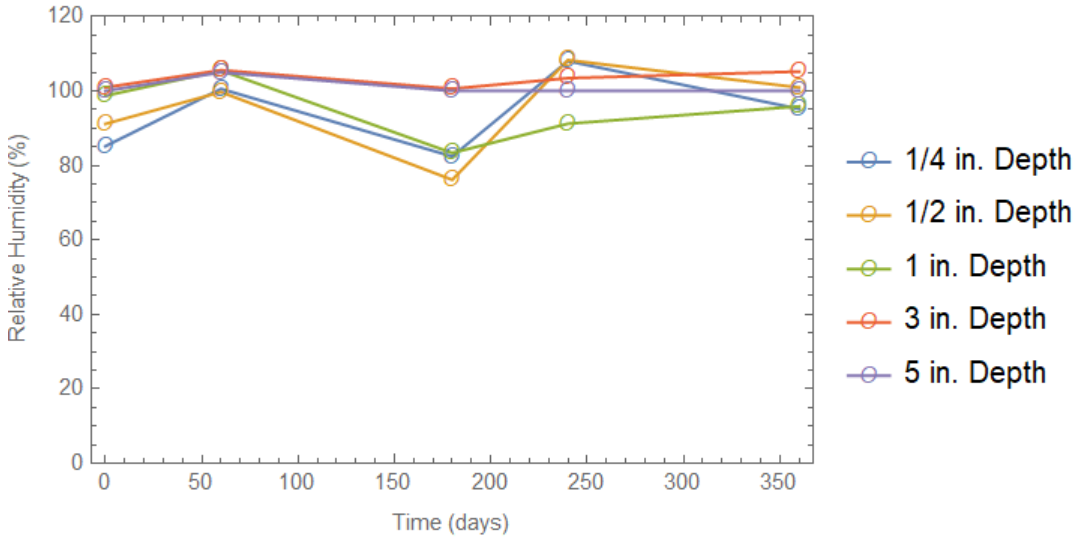

Figure 72. Relative Humidity Data from Specimen 1 at varying depths

4.6 Summary

In this study, three different simulated wall specimens were designed to mimic the behavior of post-tensioned concrete nuclear containment facility vessel walls over time as a result of concrete creep. The specimens were designed with different thicknesses, transverse and longitudinal reinforcement ratios, and level of post-tensioning stress. Each specimen contained various instrumentation to measure internal concrete temperature, concrete strain, and post-tensioning strain hourly for 3 years.

After post-tensioning was completed, the specimens were lifted and moved into their final locations. The largest post-tensioning bar losses occurred immediately after post-tensioning operations ended as a result of anchorage seat losses and primary and secondary creep. Data was collected and post-processed to determine how much strain in the concrete and post-tensioning bars changed over time, in an attempt to correlate the trends with concrete creep. Generally, the post-tensioning bars in the x-direction lost tensile strain over time. In the y-direction, the post-tensioning bars generally picked up compressive strains over time, to compensate for the stress fluctuations of the horizontal bars. The concrete gages in the x-direction generally gained more

compressive strains over the 3-year period. Most of the concrete in the y- and z- directions and post-tensioning bars in the y-direction remained relatively stable and did not change dramatically over the 3-year period.

References

1. American Concrete Institute (2014). *Building Code Requirements for Structural Concrete (ACI 318-14) and Commentary (ACI 318R-14).*
2. Bazant, Z. (1988). "Creep Analysis of Structures." *Mathematical Modeling of Creep and Shrinkage of Concrete,* Wiley, Chichester, 217-219.
3. Dywidag-Systems International (2016). "Dywidag Post-Tensioning Systems." *Dywidag Post-Tensioning Systems*, Dywidag Systems International, Bolingbrook, IL.
4. Hessheimer, M. F., Klamerus E. W., Lambert, L. D., Rightley, G. S., and Dameron, R. A. (2003). "Design and Construction of the PCCV Model." *Overpressurization Test of 1:4 Scale Prestressed Concrete Containment Vessel Model,* Albuquerque, NM, 1-12.
5. Lin, W., Liu, J. P., and Liu, J. Z. (2014). "Influence of Reinforcement Placement on the Creep of Concrete." *Key Engineering Materials*, Trans Tech Publications, Switzerland, 130-135, 629-630.
6. Marques, A. C., Bittencourt, T. N., and Barbosa, M. P. (2013). "Influence of Ambient Conditions and Loading Age on CAA Drying Influence." *IBRACON Journal of Structures and Materials*, *6* (2), 227-245.
7. Song, H. -W., Kim, S. -H., Byun, K. -J., and Song, Y. -C. (2002). "Creep prediction of concrete for reactor containment structures." *Nuclear Engineering and Design*, 217(3), 225–236.
8. Stefanou, G. D. (1981). "A General Method of Calculating Stress Redistribution Due to Differential Creep in Concrete Structures." *Computers & Structures*, 14(3-4), 231–245.
9. Tokyo Sokki Kenkyujo Co., Ltd. (2017). "Strain Gauges 2017." *Strain Gauges 2017*, Tokyo Sokki Kenkyujo Co., Ltd., Tokyo, Japan.
10. Tokyo Sokki Kenkyujo Co., Ltd. (2017). "Transducers 2017." *Transducers 2017*, Tokyo Sokki Kenkyujo Co., Ltd., Tokyo, Japan.

5 UPDATE GRIZZLY CODE WITH MATERIAL MODELS

5.1 Modeling Approach

The creep response of Specimens 1 and 2 was simulated using the BlackBear simulation tool (Spencer et al., n.d.) that was developed by Idaho National Laboratory. BlackBear is an open-source code that provides a subset of the capabilities of the Grizzly code, which simulates aging mechanisms and their effects on the integrity of nuclear power plant components. Both of these codes are built on the MOOSE framework (Permann et al. 2020), which is an open-source, finite-element-based platform for solving coupled sets of partial differential equations to represent multiple interacting physical phenomena.

This multiphysics solution platform is well-suited for the simulation of degradation mechanisms in concrete structures because they often involve interactions between thermal and moisture transport, chemical species, and mechanical deformation. Details of an initial coupled physics capability in Grizzly are described in Huang, Spencer, and Cai's 2015 report. Since that time, the majority of the concrete simulation capabilities in Grizzly (those that are not specific to nuclear reactor environments) have been moved into the BlackBear code, and incremental developments have been made to the concrete modeling capabilities in Grizzly and BlackBear, including the addition of models for creep (Giorla 2017), reinforcing bars, and concrete damage (Spencer and Hu 2018).

The primary emphasis of the present effort is to model the long-term creep response of the experimentally tested wall specimens, which are intended to be representative of prestressed concrete structures used in nuclear applications. This requires the use of models for creep and the effects of reinforcing and prestressing, as well as the effects of thermal strains in the concrete and steel. The following sections summarize the models and assumptions made in simulation runs.

5.2 Finite Element Meshes and Boundary Conditions

Because wall Specimens 1 and 2 have significantly different geometries, separate finite element models were created of these two structures, although essentially the same modeling approach was taken for both walls. Figure 73 shows the three-dimensional finite element mesh used to represent Specimen 1. The concrete wall is discretized with linear hexahedral elements, with a nominal element size of 50.8 mm (2 in). Separate material blocks are used to represent the steel blocks that serve as anchor plates to distribute the prestressing forces. As can be seen in Figure 73, a single block that represents all of the individual anchor plates is used for simplicity instead of creating separate geometric entities for each individual block. These steel blocks have a thickness of 50.8 mm (2 in), and are meshed contiguously with the concrete.

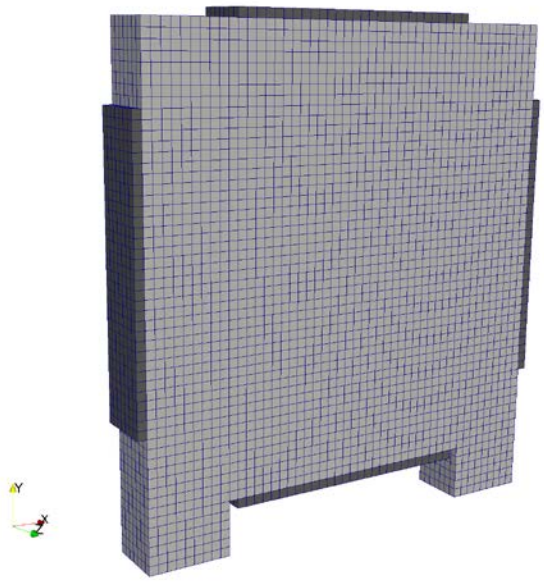

Figure 73 - Finite element mesh of Specimen 1 showing finite element discretization of concrete and steel plates

The reinforcing and prestressing bars are represented as one-dimensional truss elements that only resist axial loads and have no bending resistance. BlackBear allows these truss elements to be meshed independently of the concrete matrix that contains them by using constraints that force the nodes of the truss elements to maintain a fixed position relative to the continuum elements that they are contained within, as detailed in Spencer and Hu's 2018 document. Figure 74 shows the truss elements used to represent the prestressing and reinforcing bars in Specimen 1. These truss elements are superimposed on a translucent image of the continuum mesh of the concrete wall that contains them.

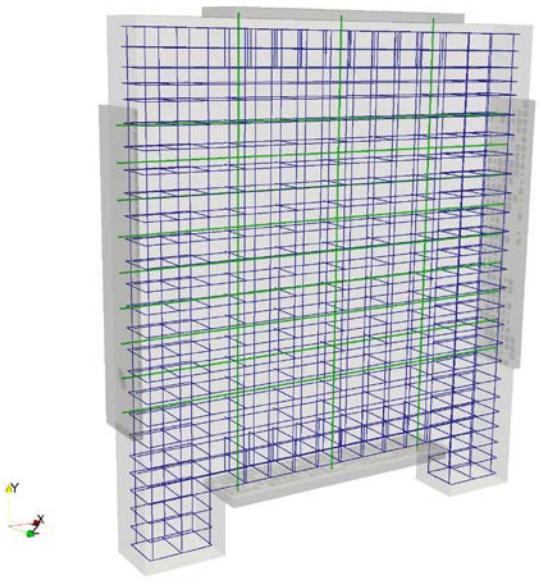

Figure 74 - Finite element mesh of Specimen 1 showing prestressing (green) and standard rebar (blue)

Although the prestressing bars and reinforcing bars are both modeled using the same types of truss elements, they are differences in the way they are used in the model. The threaded bars that are used for prestressing are not grouted, so they only have a physical connection with the concrete through the anchor plates. In the finite element model, these prestressing bars are each meshed with a single truss element, the ends of which are embedded in the steel plates at the edges of the wall. Prestressing is applied during the simulation using thermal strains that are driven by a pseudo-temperature function that is the summation of the actual temperature history and a step function that starts out with a value of zero, but suddenly decreases several days into the simulation to represent the effect of prestressing. The reinforcing bars, on the other hand, are fully bonded to the concrete, and are discretized using nominally the same density as the concrete mesh. Every node on these rebar elements is tied to its containing concrete element.

The concrete and reinforcement in Specimen 2 are represented in the same way as they are in Specimen 1, but the wall dimensions, reinforcement, and prestressing layout are different. Figure 75 shows the finite element mesh of the concrete and anchor plates for Specimen 2, and Figure 76 shows the reinforcement and prestressing in that model superimposed on the concrete mesh.

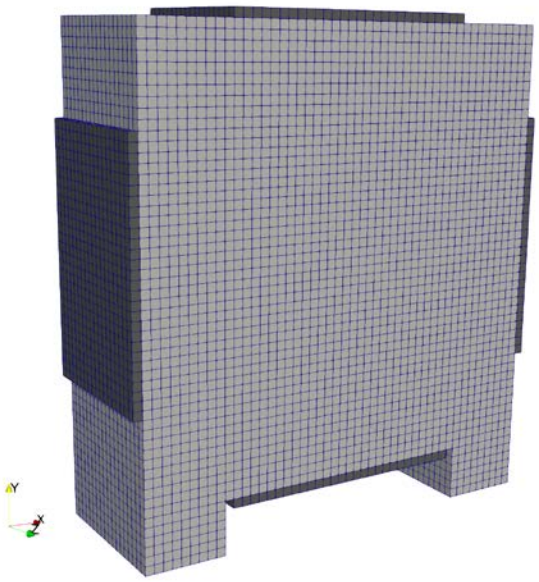

Figure 75 - Finite element mesh of Specimen 2 showing finite element discretization of concrete and steel plates

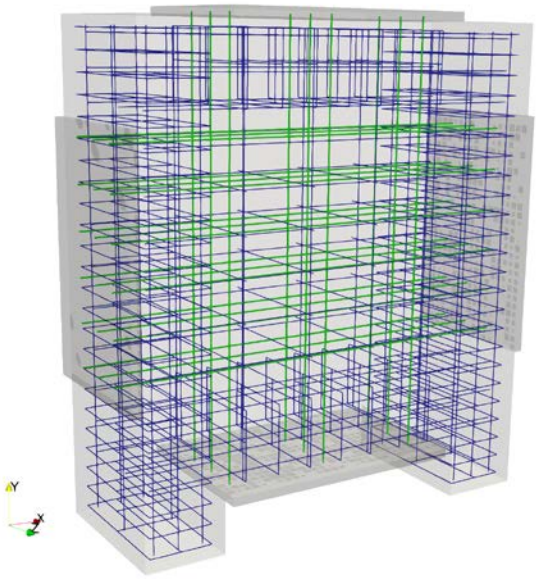

Figure 76 - Finite element mesh of Specimen 2 showing prestressing (green) and standard rebar (blue).

Because the primary objective of these experiments is to monitor long-term creep behavior, no mechanical loading was applied other than the prestressing. For both walls, a load of approximately 445 kN (100 kip) was applied to each of the vertical threaded bars, and a load of approximately 670 kN (150 kip) was applied to each of the horizontal threaded bars used for

prestressing. As previously mentioned, this was applied in the models using a pseudo-temperature function, which resulted in an applied prescribed strain. The prestressing force cannot be directly applied, so an iterative process was employed to adjust the applied strain until it resulted in a force that was approximately equal to the desired force. The same strain was applied to all of the bars in a set, so the resulting forces varied by a small amount from these target amounts. For both specimens, the prestressing was applied 4 days into the experiment. Other than the prestressing loads, the only mechanical boundary conditions applied to the model were fixed displacements at selected nodes on the bottom surface to prevent rigid body motion.

Although monitoring creep is the primary objective of these experiments, their measured strain response is affected by daily and seasonal variations in temperature because of thermal expansion, so it is important to include the effects of thermal expansion in the model. There are in general spatial variations in the temperature throughout the wall, but their effects were neglected in the simulations, and a single temperature history shown in Figure 77 was prescribed throughout the model. This temperature history was obtained by averaging the values of all of the thermocouples that had usable readings in the wall (TC4, TC6, TC7, TC10, TC12, TC13, TC14, TC15, TC16, TC18, and TC20). Because the ambient temperature can be significantly different from the internal wall temperature at a given time, it was not used in this averaged temperature.

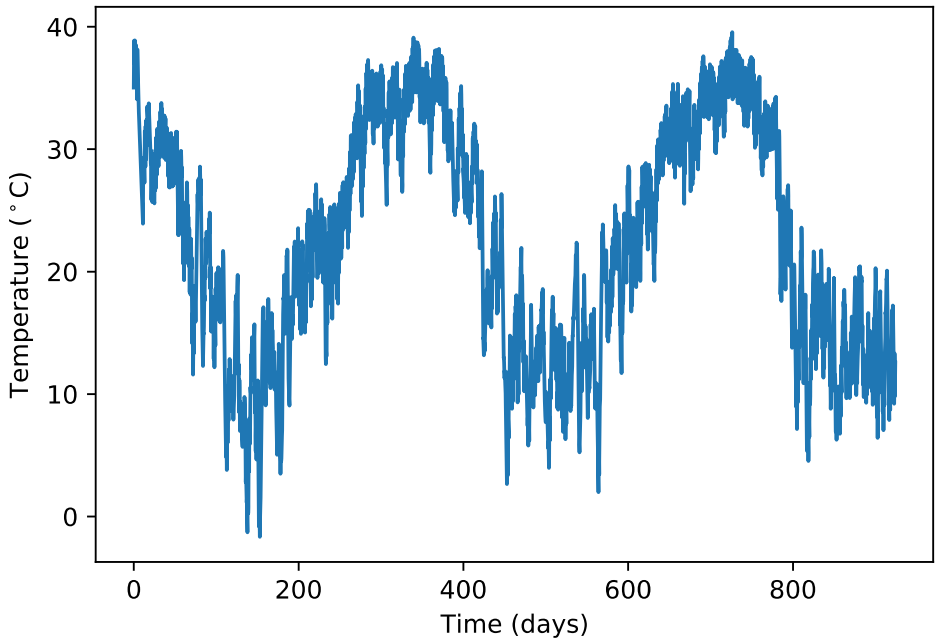

Figure 77 - Average of all thermocouple readings, applied uniformly to models for Specimens 1 and 2.

5.3 Material Properties

The concrete was modeled using a generalized Kelvin-Voigt model as described in (Giorla 2017). The material is represented by chain of spring/dashpot units, each with user-defined stiffness and viscosity. The first unit in that chain only has stiffness, and represents the instantaneous elastic response. Table 3 shows the properties of the dashpot units. The elastic modulus used for the instantaneous response is 27.8 GPa, and the Poisson's ratio is 0.2.

Table 3 - Properties of spring/dashpot units in generalized Kelvin-Voigt model for concrete creep.

Creep modulus (Pa)	Creep Viscosity (days)
1.52×10^{12}	1
5.32×10^{18}	10
6.15×10^{10}	100
6.86×10^{10}	1,000
4.48×10^{10}	10,000
1.05×10^{128}	100,000

For both the steel reinforcement and the steel anchor plates, an elastic modulus of 205 GPa is used, an a Poisson's ratio of 0.3 is used for the steel anchor plates.

A thermal expansion coefficient of $8.0\times 10^{-6}\ ^{\circ}\mathrm{C}^{-1}$ is used for the concrete and $13.0\times 10^{-6}\ ^{\circ}\mathrm{C}^{-1}$ is used for the steel.

5.4 Simulation Results

5.4.1 Processing of Experimental and Simulation Strain Data

The experimentally collected data available for comparison with simulation results primarily consists of strain gauge data in the concrete and prestressing steel. To interpret these results in the presence of temperatures that vary over time, it is important to understand how thermal strains are treated in the experimental data.

Creep strains are negligible in the prestressing steel, so the strains consist only of elastic and thermal strains. The experimentally reported strain data for the prestressing steel are only the elastic strains because of the configuration of the strain gauges. There are strain gauges oriented in the axial and transverse directions in these bars. Temperature variations cause simultaneous expansion or contractions in both of these directions, and the reported results are compensated to remove those thermal strains.

In the concrete, the strain gauges are temperature compensated, so that the raw data obtained from the gauges have the thermal strains removed. However, this thermal compensation is done for the material of the strain gauges, which has a higher coefficient of thermal expansion (CTE) than the concrete that they are embedded in so this data is not correctly temperature compensated for concrete. The internal computation of the reported strain, which is temperature-compensated for the gauge's CTE, $\varepsilon_{\text{reported}}$, at a given time is presumed to be:

$$\varepsilon_{\text{reported}} = \varepsilon_{\text{non-tc}} - \alpha_{\text{gauge}} \Delta T \tag{55}$$

where $\varepsilon_{\text{non-tc}}$ is the non-temperature-compensated strain, α_{gauge} is the CTE of the gauge material, and ΔT is the current temperature minus the temperature at the beginning of the experiment.

Assuming this is the computation done internally by the strain gauges, the non-temperature-compensated strain can thus be calculated as:

$$\varepsilon_{\text{non-tc}} = \varepsilon_{\text{reported}} + \alpha_{\text{gauge}} \Delta T \tag{56}$$

This strain would be the total strain in the concrete, which includes the elastic, creep, and thermal strains. If known, the actual CTE of the concrete, α_{conc} can be used to compute a temperature-compensated strain for the concrete, ε_{tc}, which is the summation of the creep and elastic strains:

$$\varepsilon_{\text{tc}} = \varepsilon_{\text{reported}} + (\alpha_{\text{gauge}} - \alpha_{\text{conc}}) \Delta T \tag{57}$$

Applying equations 56 and 57 to the reported data for concrete strain gauge CG4, which is oriented in the XX direction at the center of Specimen 1, result in the adjusted time histories of adjusted temperature-compensated strain and non-temperature-compensated strain shown in Figure 78. It is assumed here that $\alpha_{\text{conc}} = 8.0 \times 10^{-6}\ ^{\circ}\text{C}^{-1}$ and $\alpha_{\text{gauge}} = 11.6 \times 10^{-6}\ ^{\circ}\text{C}^{-1}$. It is evident that the time-dependent temperature variations are significantly reduced by applying these adjustments. However, even though the reported temperature-compensated strains attempt to remove the effects of thermal strain in the concrete, daily and seasonal variations are in those strains because of the effects of the thermal strains in the steel on the concrete. The computed non-temperature-adjusted strains are physically reasonable because as would be expected, they report increasingly compressive stresses shortly after initiation of the experiment, which occurred at a high point in the seasonal temperature variation and is consistent with contraction due to seasonal cooling.

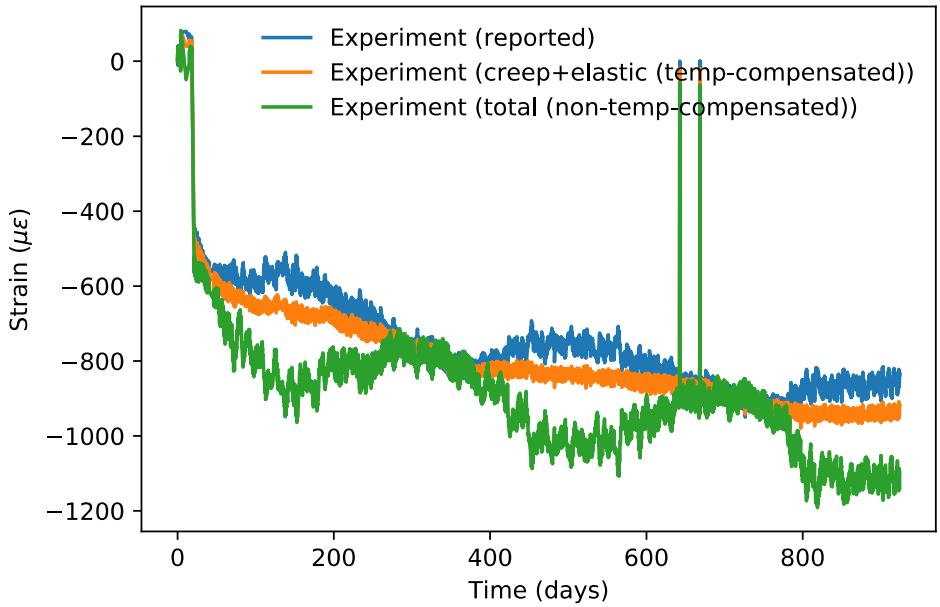

Figure 78 - Processing of raw strain data provided by instruments to provide corrected temperature-compensated strain data (which is the elastic+creep strain) and non-temperature-compensated strain data (which is the total strain). Data for CG4 (Specimen 1) are shown here

For simplicity in interpreting comparisons of the experimental results, only the adjusted temperature-compensated and non-temperature-compensated strains are shown for the concrete strain gauge locations in the results presented hereafter. These are comparable with the simulation results for the summation of the creep and elastic strain, and for the total strain, respectively, and are reported as such in the plots. For the simulations, the creep strain histories are also reported, but these cannot be directly compared with strain measurements from the experiments because the experimental creep strain cannot be isolated.

5.4.2 Specimen 1 Results

Figure 79 though Figure 82 show contour plots of the computed total strains in the XX and YY directions and total stresses in the XX and YY directions for Specimen 1. From these plots, it is evident that there is a large, roughly rectangular region in the center of the wall that experiences relatively uniform stress and strain. Also notable is the fact that the wall experiences some bending, particularly visible in the vertical direction, as evident in the stress contours on the side steel plates in Figure 82, due to the fact that the wall is relatively slender and the prestressing bars are placed slightly off-center to avoid interference between the vertical and horizontal bars.

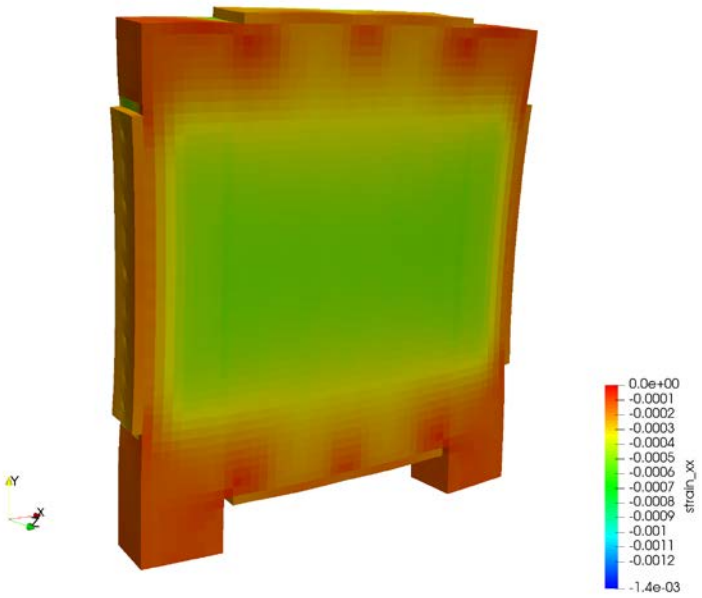

Figure 79 - Contour plot of strains in the XX direction for Specimen 1 at the end of the experiment. Deformations are magnified 100×.

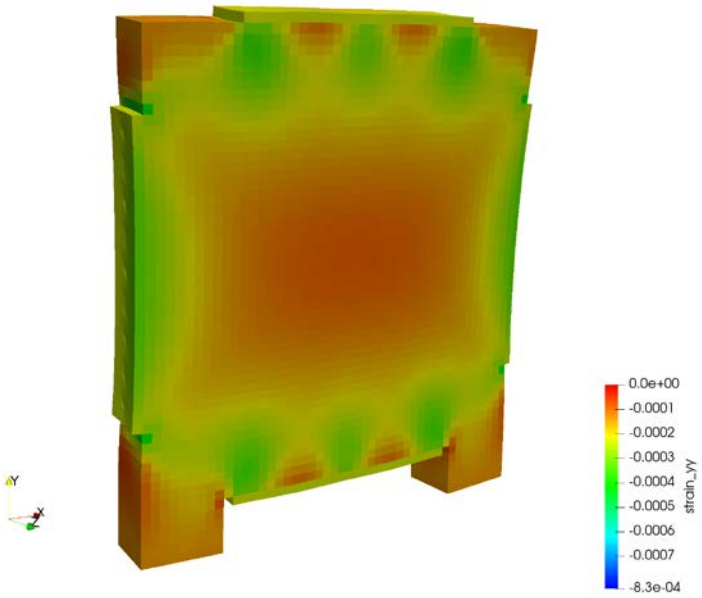

Figure 80 - Contour plot of strains in the YY direction for Specimen 1 at the end of the experiment. Deformations are magnified 100×.

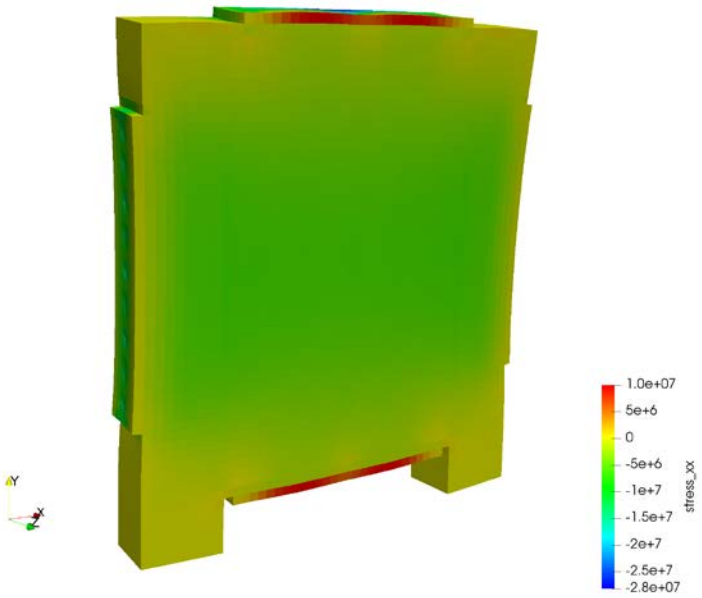

Figure 81 - Contour plot of stresses (Pa) in the XX direction for Specimen 1 at the end of the experiment. Deformations are magnified 100×.

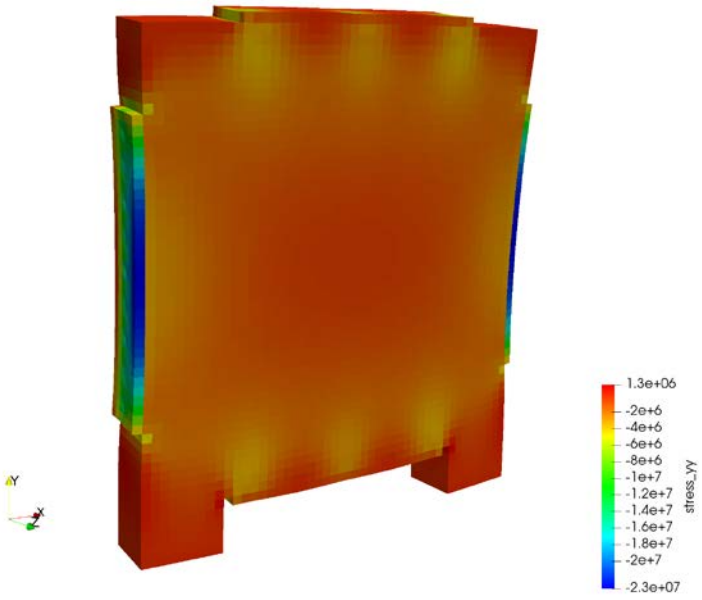

Figure 82 - Contour plot of stresses (Pa) in the YY direction for Specimen 1 at the end of the experiment. Deformations are magnified 100×.

Figure 83 - Figure 86 show time histories of the computed strain response at the locations of the concrete strain gauges that provided usable data for this experiment (CG4, CG6, CG7, and CG8). The data for CG4 and CG7 are of particular interest because these are gauges oriented in the

direction of the primary (horizontal) prestressing, and consequently experience the highest stresses and strains.

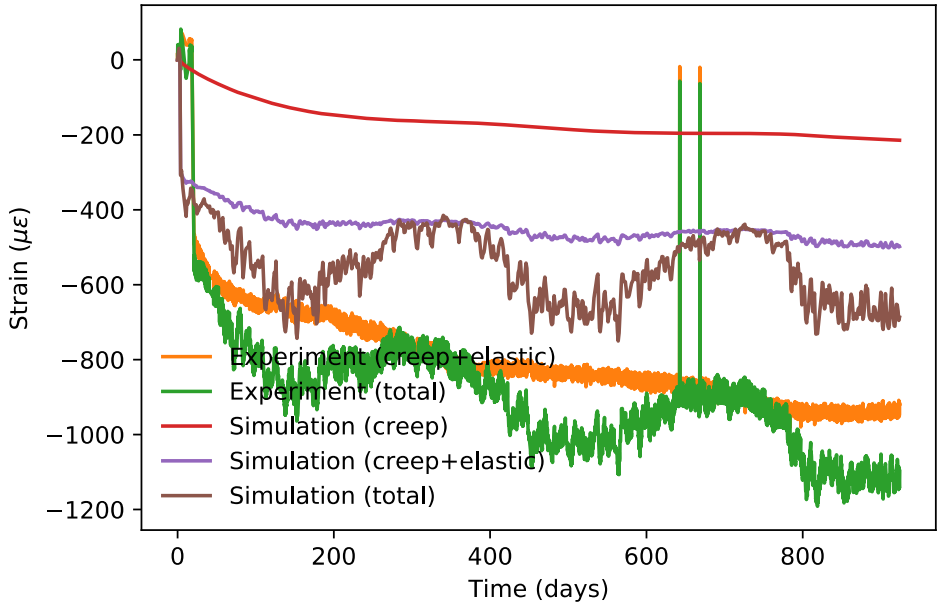

Figure 83 - Concrete gauge CG4. Specimen 1, 6.5-in. embedment (midplane of wall), XX direction.

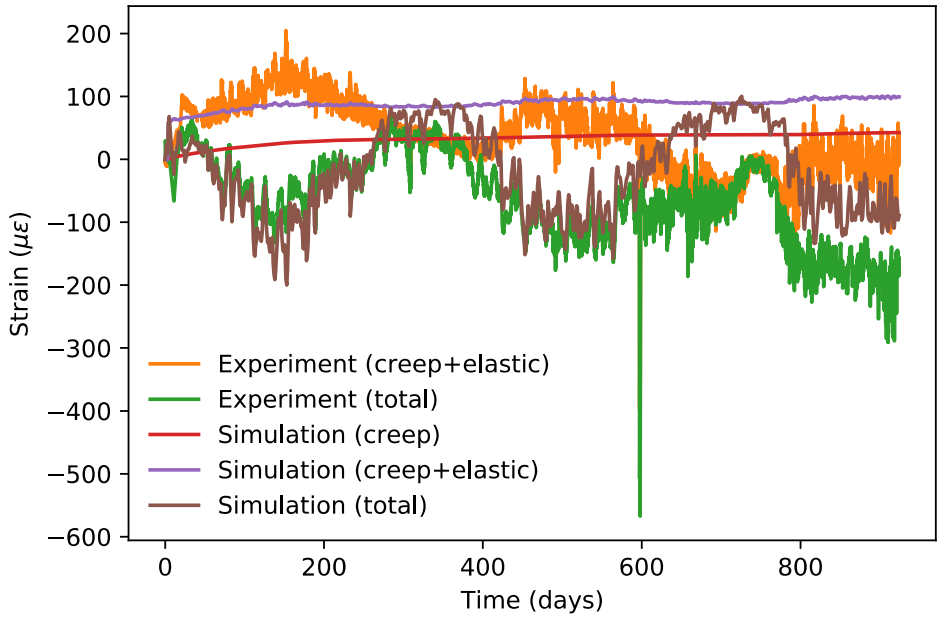

Figure 84 - Concrete gauge CG6. Specimen 1, 6.5-in. embedment (midplane of wall), ZZ direction.

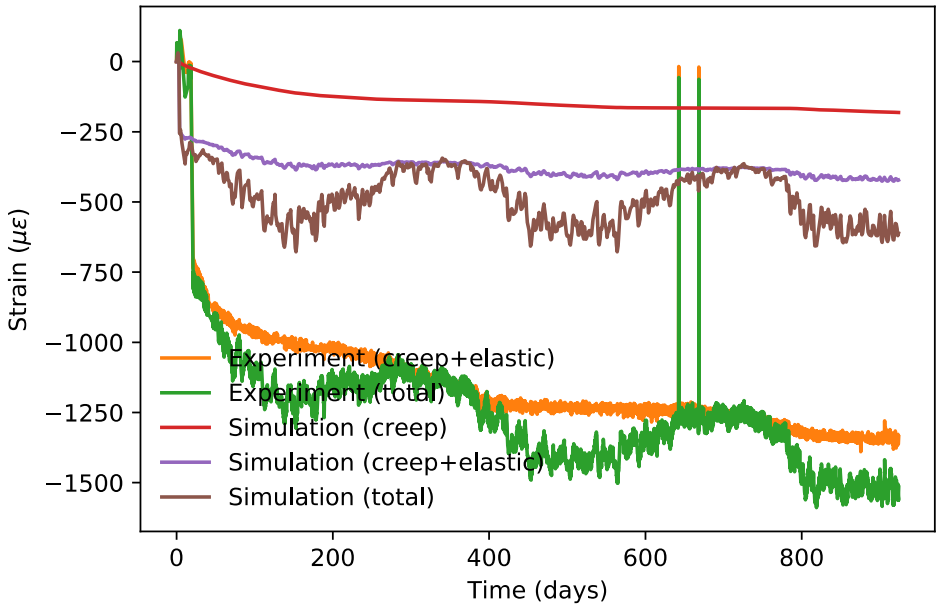

Figure 85 - Concrete gauge CG7. Specimen 1, 2.5-in. embedment (from front face), XX direction.

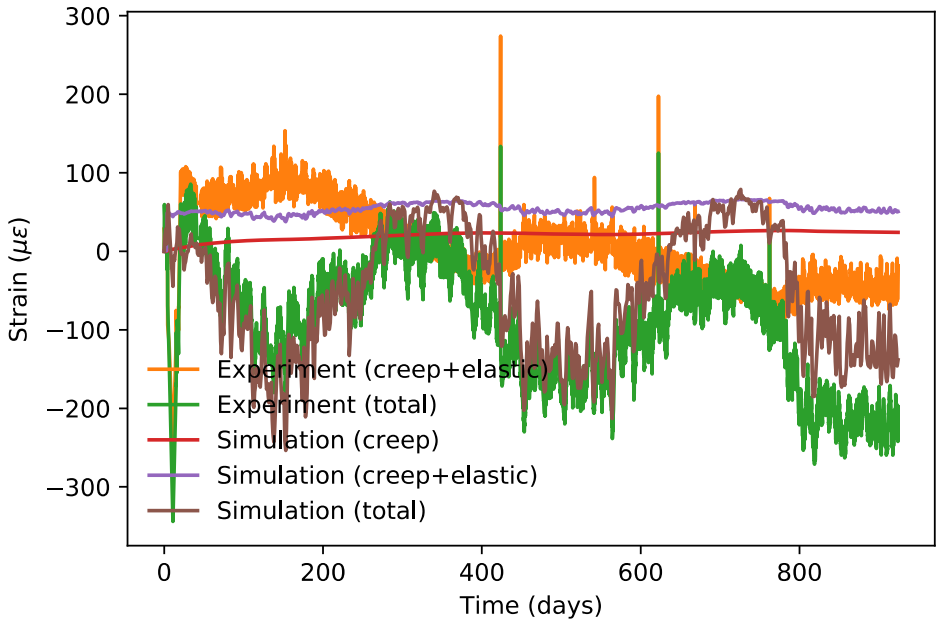

Figure 86 - Concrete gauge CG8. Specimen 1, 2.5-in. embedment (from front face), YY direction.

Figure 87 and Figure 88 show time histories of the computed strain response for the prestressing steel strain gauges that provided usable data for this experiment (SG3 and SG7). SG3 is located on the primary (horizontal) prestressing, while SG7 is located on the vertical prestressing.

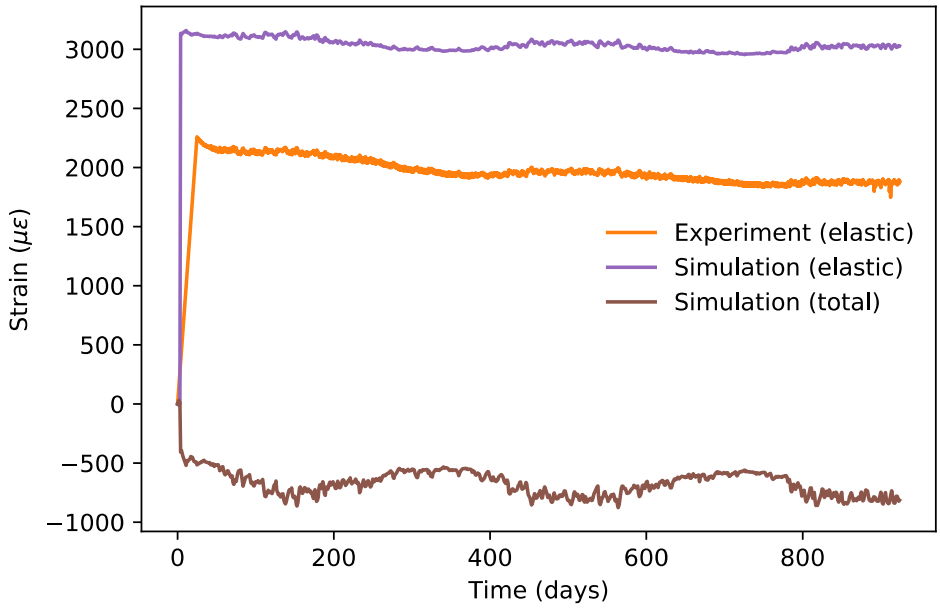

Figure 87 - Prestressing steel gauge SG3. Specimen 1, center horizontal bar

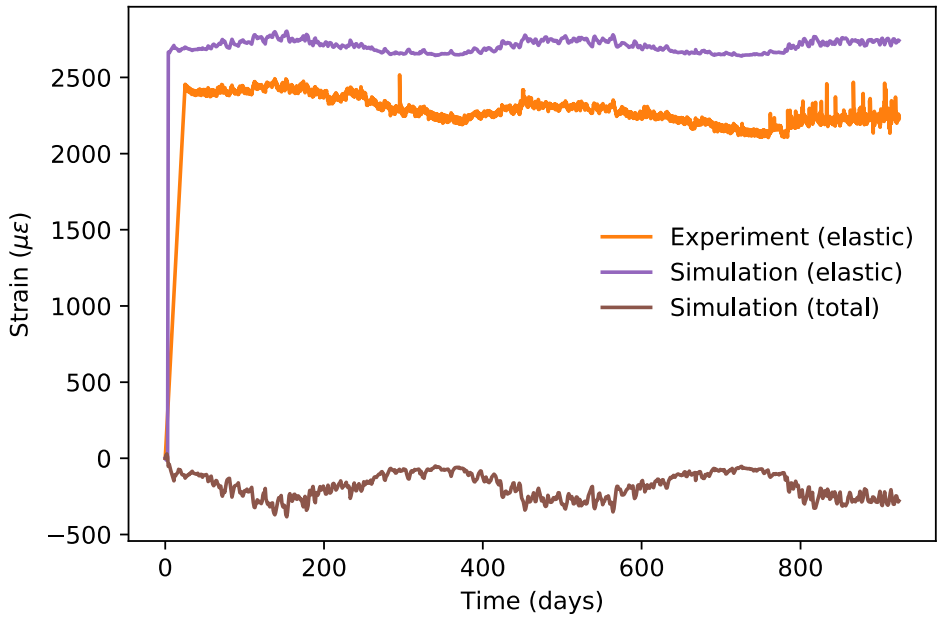

Figure 88 - Prestressing steel gauge SG7. Specimen 1, center vertical bar.

5.4.3 Specimen 2 Results

Results equivalent to those shown for Specimen 1 are also shown here for Specimen 2. Figure 89 through Figure 92 show contour plots of the computed total strains in the XX and YY directions and total stresses in the XX and YY directions for Specimen 2. These plots shown behavior that is

generally very similar to that of Specimen 1. Because there are more horizontal prestressing bars, the local deformation at the anchor points is more visible in these plots, which magnify the deformation by 100×. Also, there is less global bending of the wall than for Specimen 1 because it is much thicker and has higher stiffness, and the prestressing is less eccentric than for Specimen 1.

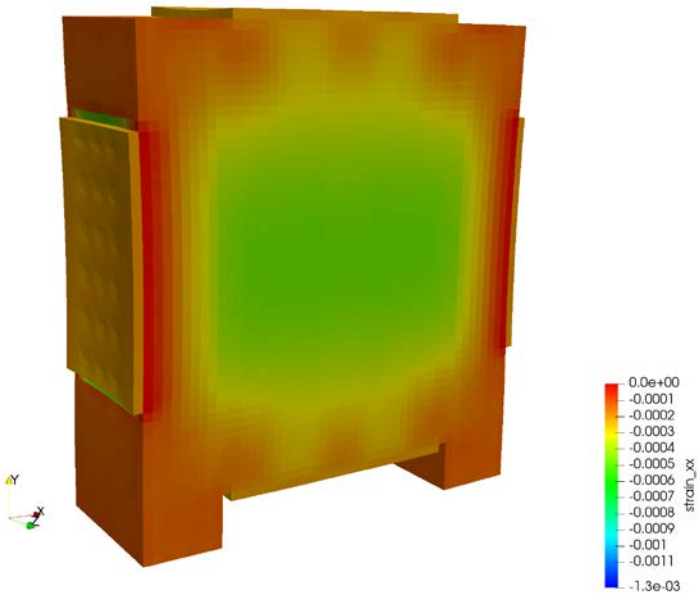

Figure 89 - Contour plot of strains in the XX direction for Specimen 2 at the end of the experiment. Deformations are magnified 100×.

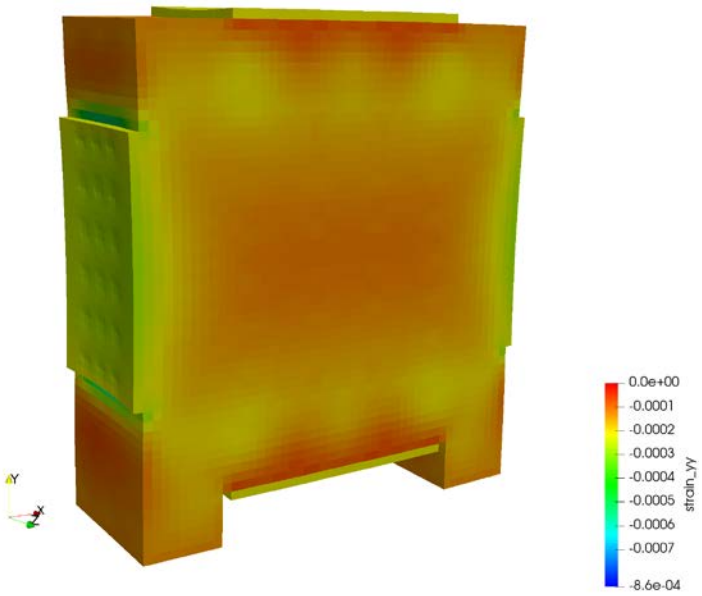

Figure 90 - Contour plot of strains in the YY direction for Specimen 2 at the end of the experiment. Deformations are magnified 100×.

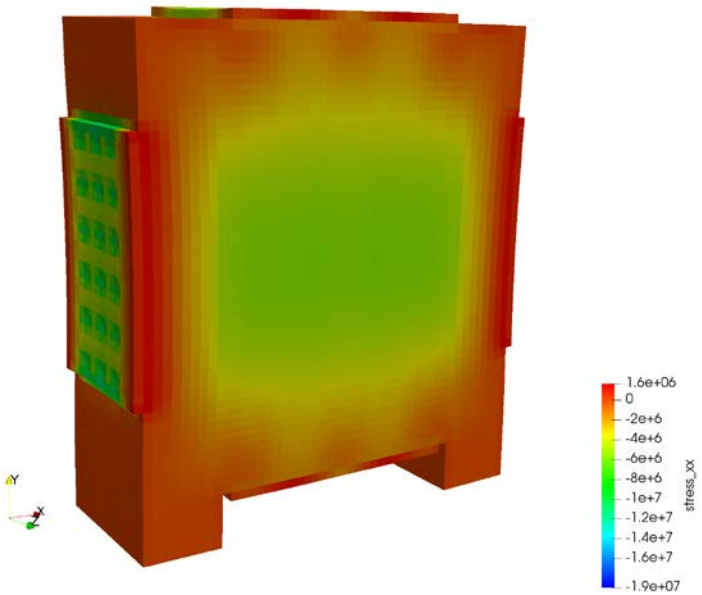

Figure 91 - Contour plot of stresses (Pa) in the XX direction for Specimen 2 at the end of the experiment. Deformations are magnified 100×.

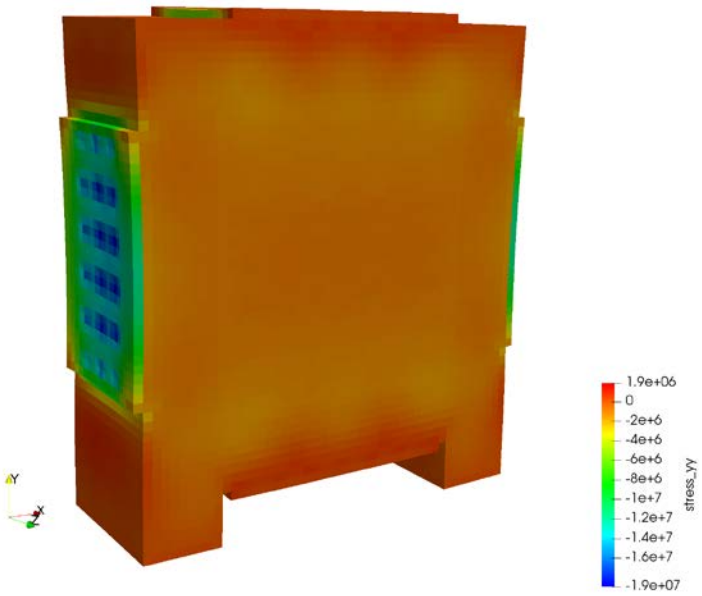

Figure 92 - Contour plot of stresses (Pa) in the YY direction for Specimen 2 at the end of the experiment. Deformations are magnified 100×.

Figure 93 through Figure 99 show time histories of the computed strain response at the locations of the concrete strain gauges that provided usable data for this experiment (CG10, CG12, CG13, CG14, CG15, CG16, and CG18). The data for CG10, CG13, and CG16 are for the gauges in the horizontal direction with the highest prestressing.

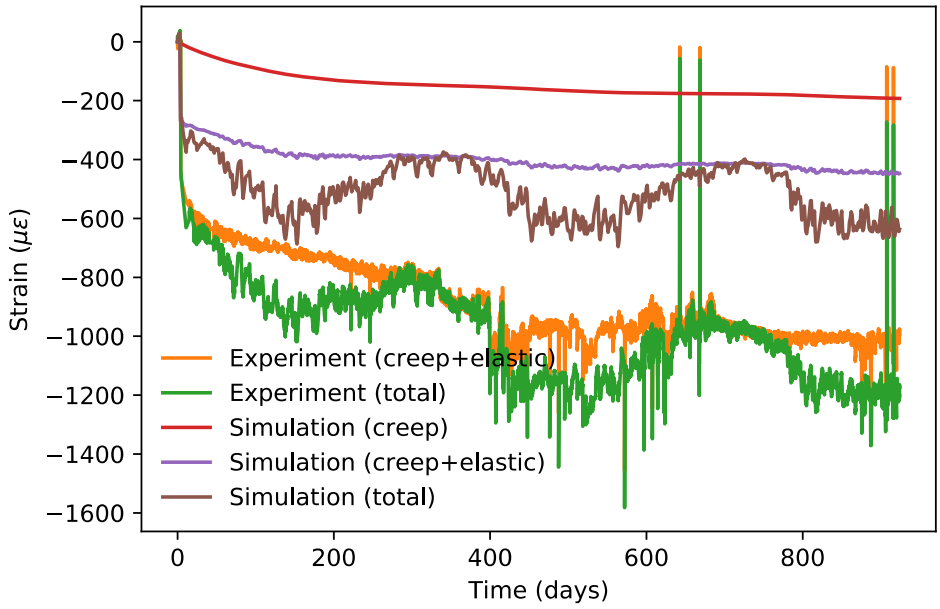

Figure 93 - Concrete gauge CG10. Specimen 2, 2.5-in. embedment (from back face), XX direction

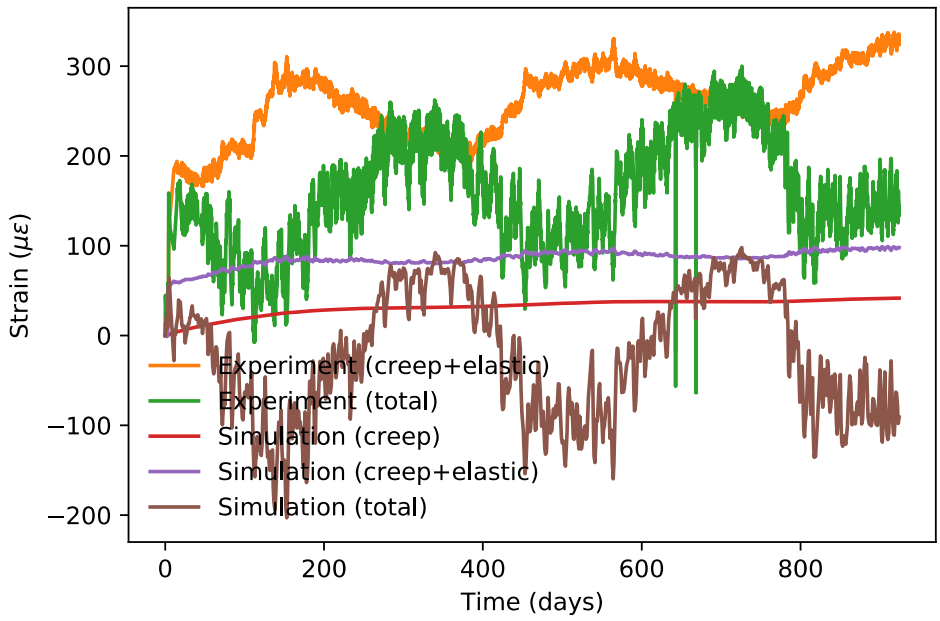

Figure 94 - Concrete gauge CG12. Specimen 2, 2.5-in. embedment (from back face), ZZ direction

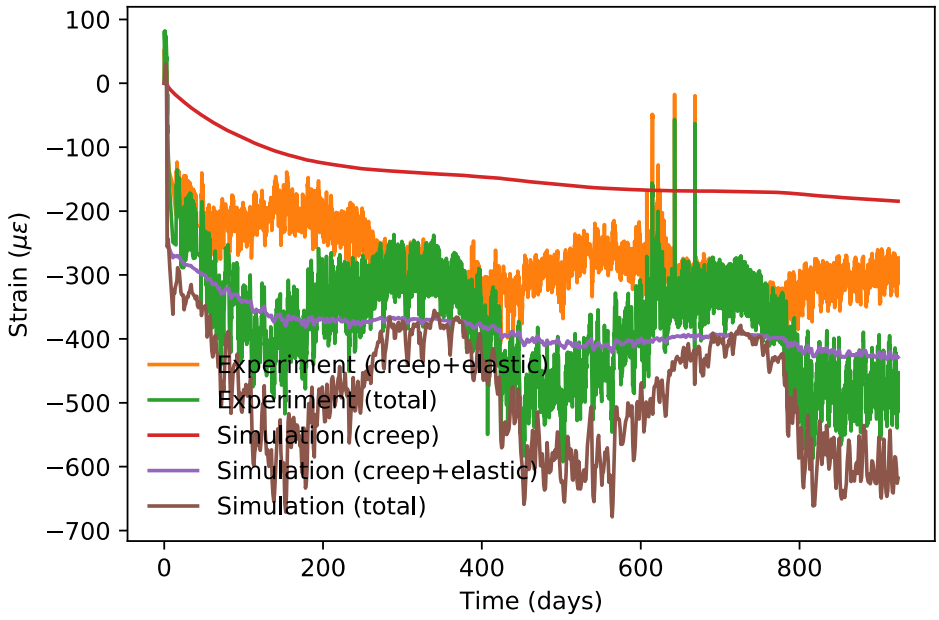

Figure 95 - Concrete gauge CG13. Specimen 2, 9.0-in. embedment (from back face), XX direction

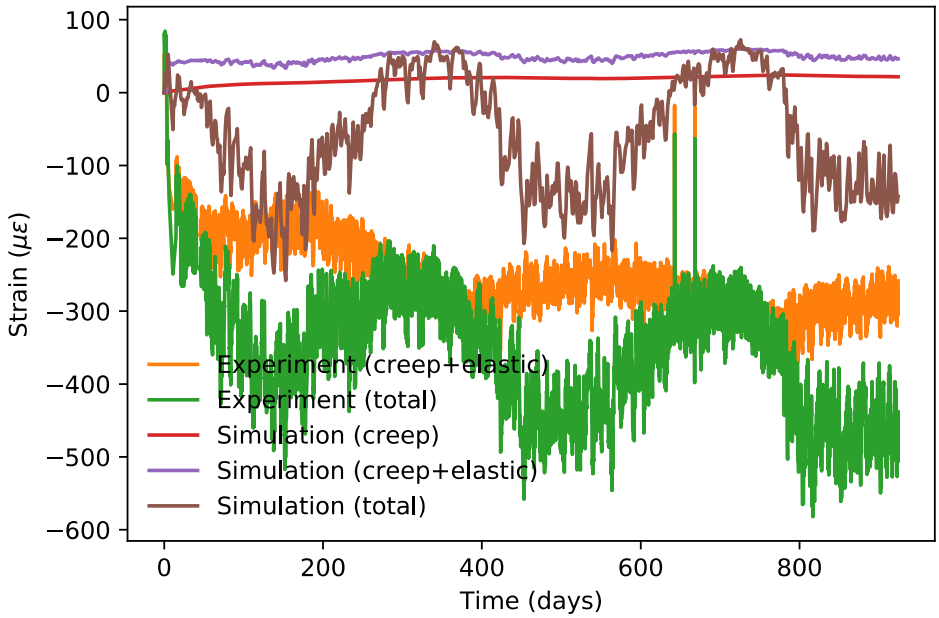

Figure 96 - Concrete gauge CG14. Specimen 2, 9.0-in. embedment (from back face), YY direction.

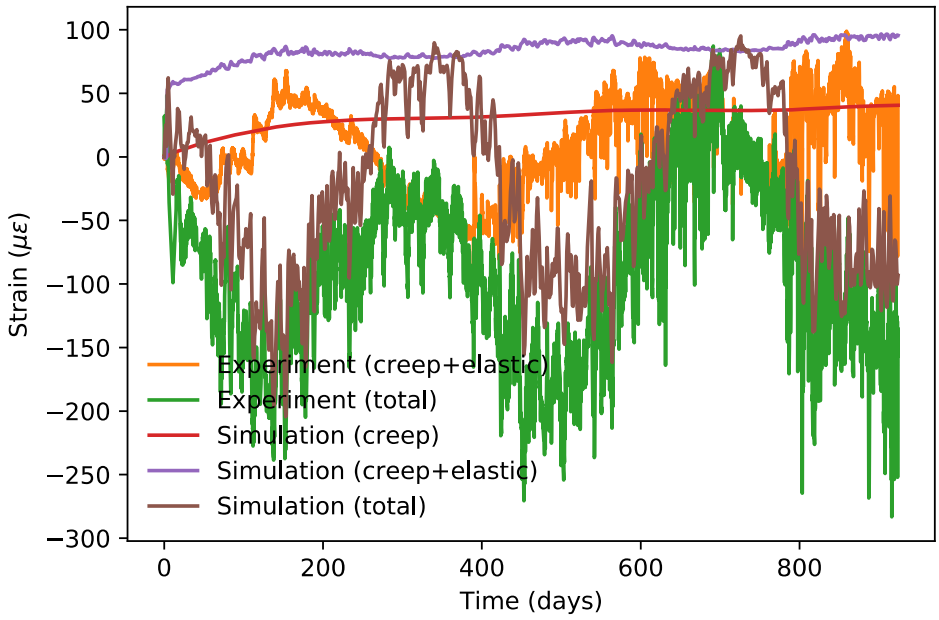

Figure 97 - Concrete gauge CG15. Specimen 2, 9.0-in. embedment (from back face), ZZ direction.

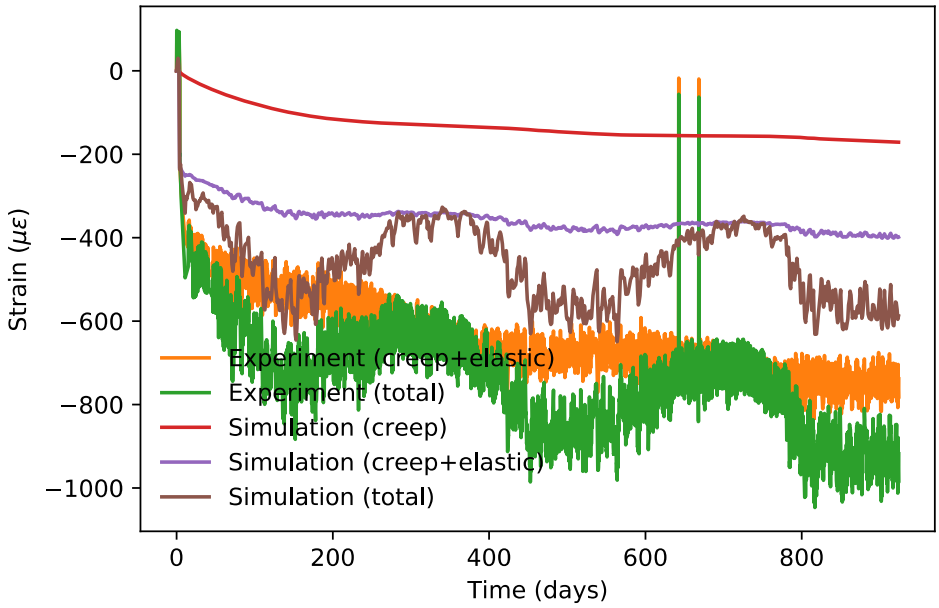

Figure 98 - Concrete gauge CG16. Specimen 2, 18.0-in. embedment (midplane of wall), XX direction.

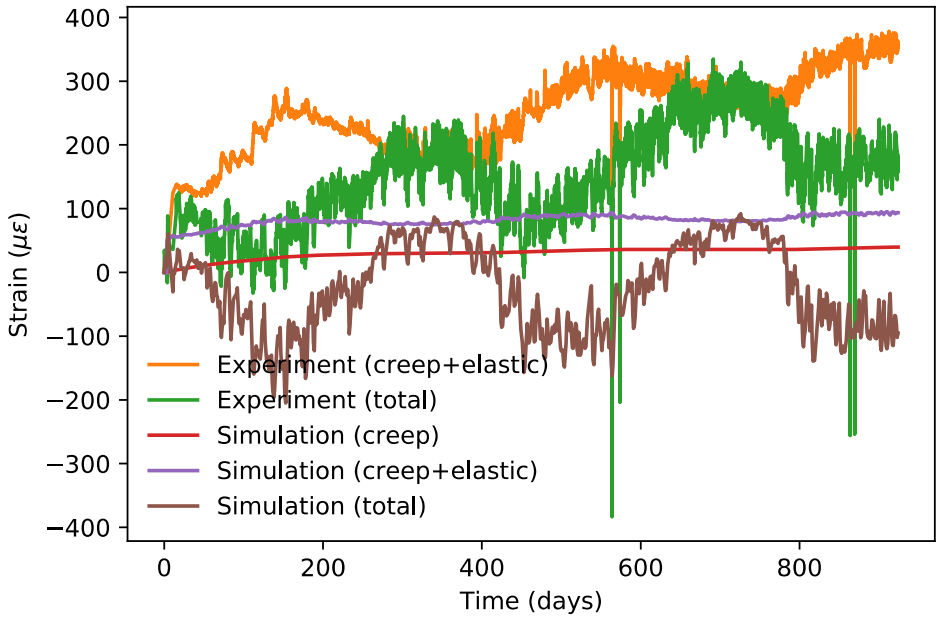

Figure 99- Concrete gauge CG18. Specimen 2, 18.0-in. embedment (midplane of wall), ZZ direction.

Only one strain gauge in the prestressing steel (SG10) provided usable data for this experiment, and the simulation and experimental results for that bar are shown in Figure 100. This was one of the primary horizontal bars near the center of the wall.

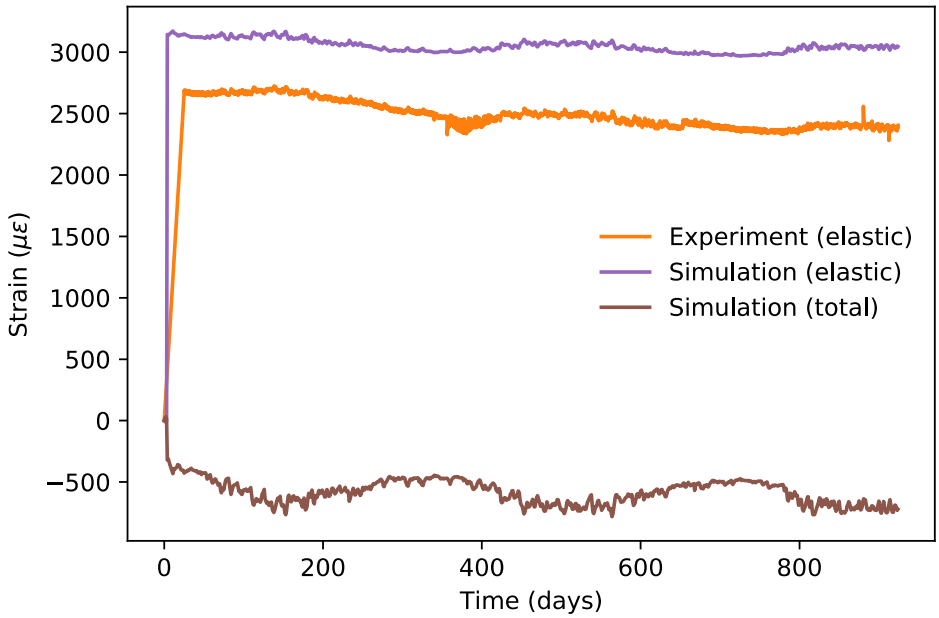

Figure 100 - Prestressing steel gauge SG10. Specimen 2, horizontal bar near midplane, slightly above center

Comparison of Experimental and Simulation Results

The strain gauge results from Specimens 1 and 2 are quite consistent with each other. For the concrete response, focusing on the results for the horizontal (XX) direction shown in Figure 83 and Figure 85 for Specimen 1, and in Figure 93, Figure 95, and Figure 98 for Specimen 2, it can be seen that the simulations consistently underpredicted the strain increment due to application of prestressing by roughly 30–50%. The one exception to this was CG13, where the simulation predicted slightly higher strains due to prestressing than the experiment.

One might reasonably assume that this could be caused by applying prestressing loads that are too low in the simulations, but for all of the prestressing bars for which data is available in Figure 87, Figure 88, and Figure 100, the simulations actually indicate higher prestressing strains than the experiments. It should be noted that the aside from the differences in the strains due to prestressing, the elastic strains in the prestressing generally predict the seasonal variations of the temperature-compensated strains in the prestressing very well.

Consistent with the underprediction of the concrete strains due to prestressing, the same locations where these elastic strains were underpredicted also show underpredictions of the long-term creep strains due to the prestressing. Encouragingly, consistent with this, the one location where the simulations predicted slightly higher initial strains than the experiments (CG13) predicts higher creep strains than the experiments.

It should also be noted that the simulation results do not indicate drastically different creep strains at the various locations where creep in the horizontal direction was monitored. For Specimen 1, the final values of the creep strain for CG4 was -214×10^6, and for CG7 it was -181×10^6. The final values of the creep strain for Specimen 2 for CG10, CG13, and CG16 were -192×10^6, -185×10^6, and -171×10^6, respectively. There was far more variation in the experimental data, with values of the final total strain ranging from roughly -400×10^6 to -1500×10^6 for these same locations, when it would have been expected that they would all have nominally the same response based on the loading conditions. There are a number of potential explanations for these local variations in the experimental response, which could include issues with instrumentation or local variations in the applied prestressing.

Despite these issues, it is encouraging that the creep law, which was derived based on accelerated testing of hardened cement paste and simulated mesoscale structures, was able to reasonably predict the creep response of a large-scale structural element on a time scale of over 2 years.

Application to Long-Term Loading Scenario

To demonstrate the response of the creep model under even longer-term loading, the response of Specimen 1 was simulated over 40 years. For this simulation, seasonal temperature variations were not considered, so a constant temperature was assumed. Results are not compared with experimental data, but are reported here for one location of interest (CG4) in the concrete, as shown

in Figure 101. Because the thermal strains are not considered here, only the simulated creep and total strains are reported. It is notable that over 40 years of being subjected to the prestressing loads, the creep strains are roughly 50% higher than they were for the approximately 2-year experiment. This model could be readily applied to simulate load redistributions caused by making changes to the prestressing, such as those that might be caused by repairs.

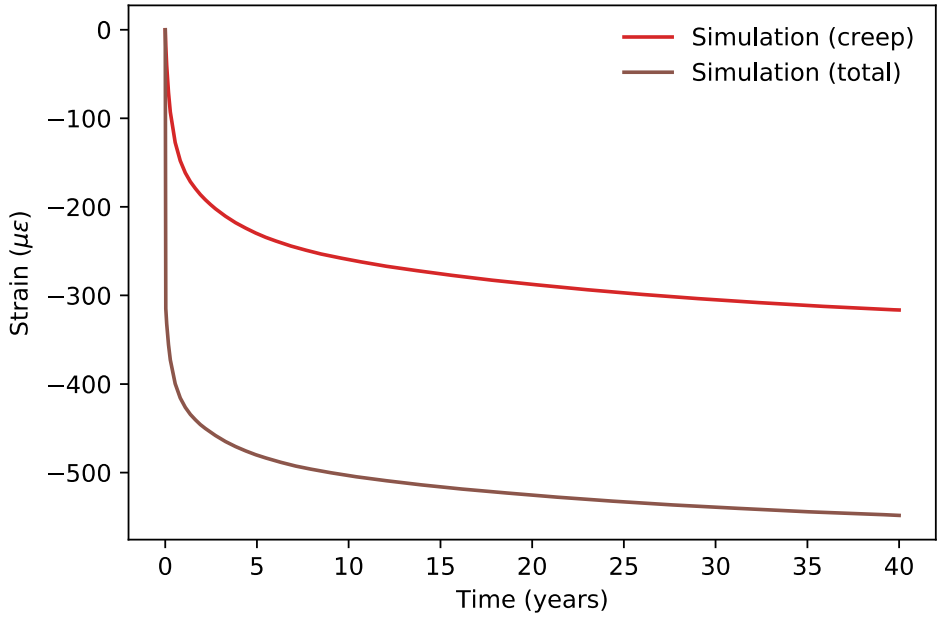

Figure 101 - Long-term creep strains of Specimen 1 reported at the location of concrete gauge CG4 (midplane of wall), XX direction.

Sources of error

It can be seen that simulations consistently underpredicted the strain compared to the experimental data. Few sources of discrepancies or errors between the experimental and simulation data are presented below:

Experimental:
(a) Concrete measurements:

- varying TCE for concrete gage and concrete resulting in errors due to daily and seasonal temperature changes.
- initial prestressing was performed over a 2-week period. Load redistribution of the PT forces may have resulted in some strain variations.
- sensor issues due to misalignment, local effects near sensor that cause inaccurate readings, occasional bad data for unconfirmed reasons (possibly faulty wired connections, moisture conditions in exterior exposure, length of lead wires from sensors to data acquisition/temp effects), data acquisition errors in system itself,
- thermal and moisture variations (gradients) within the concrete depth.

- effects of drying creep and other issues related to exterior exposure of weather (temperature and moisture) and varying sun radiation during the day.
- effects of free shrinkage strain (sample without loading) due to autogenous shrinkage/self-desiccation of water in the pores.

(b) Post Tensioning Steel measurements:
- there is approximately 10-15% reduction in cross sectional area of the concrete between the PT ducts and the longitudinal rebar in the specimen
- unknown local temperature fluctuations that may significantly vary between PT steel and concrete throughout the specimen.
-Overall TCE of strain gage/adhesive and it's comparison/differences to the PT steel.
-Many strain gages were damaged during construction due to very difficult assembly conditions (primarily due to duct alignment issues and a small duct opening). Some gages may have been bearing on the duct walls leading to bad data.

Modeling predictions:
- Effects of using an elastic/linear modulus of elasticity for concrete and the value used.
- Effects of the TCE values used for steel and concrete and temperature fluctuations of both materials (see above)
- method for initial prestressing and boundary conditions (initial PT steel and concrete wall strains near PT ends and wall center)
- rebar-concrete interface (slip) effects.
- inaccuracy in upscaling from cement mortar creep model to concrete to large reinforced concrete wall assembly under 3D state of stress

5.5 Summary

The creep model developed in this project, based on accelerated testing of mortar and upscaled to a continuum-scale Kelvin-Voigt model, has been applied to simulate the structural-scale experiments of prestressed concrete walls conducted in this project using the BlackBear code. These models are able to represent the effects of reinforcing and prestressing. Although there are some discrepancies with experimental data, they are able to predict the trends of the creep response in these experiments. One of these experimental models was also applied to an extended time to demonstrate how the findings from this study can be used to predict the behavior of actual structures of interest that have been in service for extended periods of time.

References

1. Giorla, Alain, 2017, *Implementation of Concrete Creep Model in Grizzly,* ORNL/TM-2017/729. Oak Ridge, Tennessee, Oak Ridge National Laboratory.
2. Huang, Hai, Benjamin W. Spencer, and Guowei Cai, 2015, *Grizzly Model of Multi-Species Reactive Diffusion, Moisture/Heat Transfer and Alkali-Silica Reaction in Concrete*, INL/EXT-15-36425, Idaho Falls, Idaho, Idaho National Laboratory.

3. Permann, Cody J., Derek R. Gaston, David Andrš, Robert W. Carlsen, Fande Kong, Alexander D. Lindsay, Jason M. Miller, et al., 2020, “MOOSE: Enabling Massively Parallel Multiphysics Simulation.” *SoftwareX* 11 (January), pp. 100430.
4. Spencer, Benjamin W., William M. Hoffman, Sudipta Biswas, Wen Jiang, Alain Giorla, and Marie A. Backman. n.d. “Grizzly and BlackBear: Structural Component Aging Simulation Codes.”
5. Spencer, Benjamin W., and Tianchen Hu. 2018, *Enhancements to Concrete Modeling Capabilities in Grizzly 2.0*, INL/EXT-18-51526, Idaho Falls, Idaho, Idaho National Laboratory.

6 CONCLUSIONS

The primary contribution of this project is the framework to assess multi-decade long creep behavior of nuclear concrete structures over short periods of time. The experimental data on cement mortar and concrete creep has been established by leveraging the temperature dependence of creep and the TTS principle. This approach has been used to extend 3 years of data to nearly 60 years of mortar and nearly 30 years of concrete creep data. The ability to generate decades of data in 2-3 years is a powerful capability that can be applied to concrete creep in a wide variety of applications. Specific to NPPs, the mixture design of a plant's concrete structures can be studied to assess the long-term behavior of creep in a particular NPP. The new mortar scale creep frame designed in this research allows for smaller testing frames amenable to placing in temperature controlled chambers or ovens to enable the use of TTS.

The mortar creep data was successfully upscaled to concrete creep through the use of highly realistic, 3D concrete microstructures modeled in FEA simulations. The 3D concrete microstructure generation codes are flexible and account for a variety of aggregate size gradations, aggregate morphologies, and volume fractions. Finite element analysis performed on these virtual microstructures highlights the primary usefulness of this work – the ability to quickly upscale mortar viscoelastic behavior to long-term concrete creep/relaxation data. The agreement of the simulation data with the experimental concrete creep data provides a computational route to obtain concrete creep data from small, compact mortar experiments. This computational tool will allow researchers to maximize the benefits of the experimental approach presented and obtain several decades of concrete creep from mortar experiments conducted over a much shorter time-scale.

The homogenized concrete creep behavior obtained from the FEA simulations was successfully used in Grizzly to model post-tensioned, structural concrete behavior. Large-scale specimens were constructed to provide validation to the Grizzly models, including an unreinforced, unloaded specimen that provides valuable free strain (e.g., thermal, moisture) data, unrelated to loading. The Grizzly model was successful in predicting the overall trends of the creep response of the large-scale concrete. A major implication of this is the ability to use Grizzly with the viscoelastic constitutive model of concrete simulate "*what if*" scenarios – such as repair, critical damage, and load reversals.

As a whole, this project has provided an experimental and computational framework (Figure 102) to obtain decades of large-scale data to predict creep in nuclear concrete structures. This framework has been experimentally validated, thereby enabling future researchers to more thoroughly assess specific nuclear concrete structures with certain materials and structural designs for critical issues and early detection of structural failure. The developed framework can be used in two ways: 1) if the concrete mixture design for the structure to be simulated is similar to the EDF mixture used in this research, one can simply use the concrete constitutive properties given in Section 5.3 directly in Grizzly to simulate long-term (out to 60 years) structural response. The uniaxial viscoelastic relaxation modulus or compliance is the only needed viscoelastic property

since the results of this work indicate that, for mature concrete with minimal drying, the viscoelastic Poisson's ratio (VPR) may be presumed constant with minimal error; 2) if the concrete mixture is significantly different that the EDF mixture considered in this research, then one can use each step in Figure 102. First, miniaturized mortar specimens can be used to measure creep at three temperatures (20 C – 80 C) over a one-three year period. Elastic Young's modulus and Poisson's ratio must also be measured on the mortar. Next, TTS can be used to generate a master curve for the uniaxial creep compliance of the mortar, with the ability to predict creep over several decades. The mortar master compliance curve can then be upscaled to concrete creep compliance using the computational homogenization scheme detailed in this report. The output from the computational homogenization includes the Young's modulus and uniaxial viscoelastic compliance/relaxation of the concrete as well as the Poisson's ratio of the concrete. These constitutive properties enable the prediction of concrete creep over several decades, and are input into the Grizzly structural FEA code to enable simulations of real NPP structures, with discrete reinforcement and post-tensioning, during events such as simulated repairs, damage, etc. In summary, the experimental and computational framework provides a toolset that enables long-term analysis of the impact of creep on decades-old NPP structures for the first time.

The research described in this report led to the production of three dissertations, authored by Christa Torrence, Aishwarya Barinakumar, and Lauren Kelley. Additional details and discussion may be found in the text of the dissertations, which will all be freely available for download from Texas A&M Libraries after January 1, 2021.

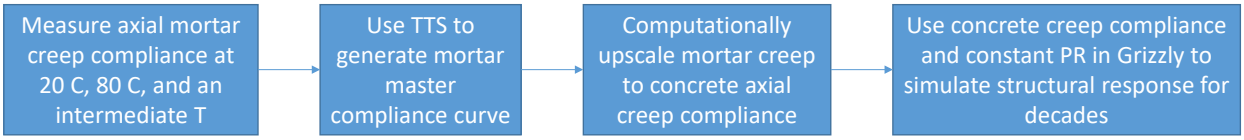

Figure 102. Experimental and computational framework developed and validated in this research project for evaluating NPP concrete structures for the effects of long-term creep.